QUANTIFYING FOREST MORTALITY

WITH THE REMOTE SENSING OF SNOW

By

Emily Hewitt Baker

B.A., Whitman College, 2010

A thesis submitted to the

Faculty of the Graduate School of the

University of Colorado in partial fulfillment

of the requirement for the degree of

Masters of Arts

Department of Geography

2015

This thesis entitled:

Quantifying forest mortality with the remote sensing of snow

Written by Emily Hewitt Baker

has been approved for the Department of Geography by

_____

Noah Molotch

_____

Mark Williams

_____

Thomas Veblen

Date_____

The final copy of this thesis has been examined by the signatories, and we find that both the content and the form meet acceptable presentation standards of scholarly work in the above mentioned discipline.

Baker, Emily Hewitt (M.A. Geography)

Quantifying forest mortality with the remote sensing of snow

Greenhouse gas emissions have altered global climate significantly, increasing the frequency of drought, fire, and pest-related mortality in forests across the western United States, with increasing area affected each year. Associated changes in forests are of great concern for the public, land managers, and the broader scientific community. These increased stresses have resulted in a widespread, spatially heterogeneous decline of forest canopies, which in turn exerts strong controls on the accumulation and melt of the snowpack, and changes forest-atmosphere exchanges of carbon, water, and energy. Most satellite-based retrievals of summer-season forest data are insufficient to quantify canopy, as opposed to the combination of canopy and undergrowth, since the signals of the two types of vegetation greenness have proven persistently difficult to distinguish. To overcome this issue, this research develops a method to quantify forest canopy cover using winter-season fractional snow covered area (F_{SCA}) data from NASA's Moderate Resolution Imaging Spectroradiometer (MODIS) snow covered area and grain size (MODSCAG) algorithm. In areas where the ground surface and undergrowth are completely snow-covered, a pixel comprises only forest canopy and snow. Following a snowfall event, F_{SCA} initially rises, as snow is intercepted in the canopy, and then falls, as snow unloads. A select set of local minima in a winter F_{SCA} timeseries form a threshold where canopy is snow-free, but forest understory is snow-covered. This serves as a spatially-explicit measurement of forest canopy, and viewable gap fraction (VGF) on a yearly basis. Using this method, we determine that MODIS-observed VGF is significantly correlated with an independent product of yearly crown mortality derived from spectral analysis of Landsat imagery at 25 high-mortality sites in northern Colorado. ($\bar{r} = 0.96 \pm 0.03, \bar{p} = 0.03$). Additionally, we determine the lag timing

between green-stage tree mortality and needlefall, showing that needlefall occurred an average of 2.6 ± 1.2 years after green-stage mortality. We relate observed increases in the VGF with crown mortality, showing that a 1% increase in mortality area produces a 0.33 ± 0.1 % increase in the VGF.

ACKNOWLEDGEMENTS

This research was funded by the "Error analysis of MODIS fractional snow-covered area and snow albedo in mountainous regions" award from the National Aeronautics and Space Administration (NASA). Funding was also received from the University of Colorado's Undergraduate Research Opportunities Program (UROP).

I would like to give special thanks to Noah Molotch, Dominik Schneider, Theodore Barnhart, and the Mountain Hydrology Lab for their assistance in developing this project, from concept, through coding difficulties, to advice on analytical techniques, and comments on the final thesis document. I would also like to acknowledge the assistance of Danielle Beaty with image processing, and Roger Carter for a portion of the fieldwork. I also thank my committee members for their guidance, and would like to recognize my grandmother Sylvia Fritch for always telling me “you’re so intelligent”.

This thesis is dedicated to my parents Ahmee Hewitt and Trace Baker for cultivating my love of snow and interest in science from a young age, for always encouraging me to adventure, and for never letting me forget that:

“…all true paths lead through mountains.”

– Gary Snyder

TABLE OF CONTENTS

LIST OF TABLES

LIST OF FIGURES

1 INTRODUCTION

1.1 IMPORTANCE OF FORESTS AND LACK OF CANOPY MAPPING

Forests provide countless ecological, societal, and climate benefits to humanity. They exert strong controls on the hydrologic cycle, atmospheric carbon levels, and global land surface albedo. However, forest canopy extents, as differentiated from undergrowth, are currently difficult to detect with commonly used remote sensing products [*Coops and Wulder*, 2010; *Heiskanen et al.*, 2012; *Bright et al.*, 2013; *Buma et al.*, 2013].

Global forests cover 43 million km^2, approximately 30% of the land surface [*Bonan*, 2008]. Changing patterns of temperature and precipitation have increased forest disturbances, and more extreme climate events are expected to increase the extent and frequency of future die-offs [*Allen et al.*, 2010; *Hicke et al.*, 2012; *Hart et al.*, 2014]. Disturbances alter forest canopy and structure, changing their role in planetary exchanges of carbon and energy [*Adams et al.*, 2010]. In the western United States, disturbances from insect outbreaks and fire are already increasing in both area affected and in severity of disturbance [*Westerling et al.*, 2006; *Meddens et al.*, 2012; *Dennison et al.*, 2014]. As levels of atmospheric carbon rise and global climate continues to warm, understanding the impacts of forest-loss triggered by these events will only increase in importance.

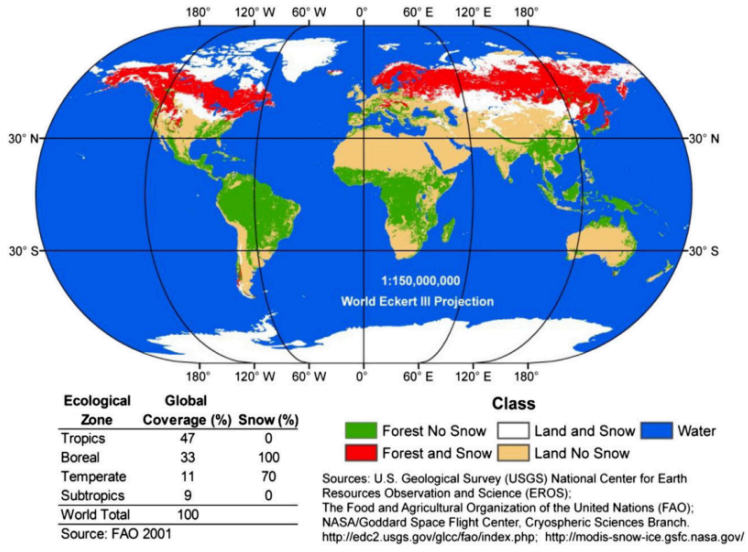

Figure 1: Global distribution of forests within the seasonal snow zone. The intersection of forests and seasonal snow zone are shown in red, primarily in the Northern Hemisphere, composing ~40 % of global forest area. [*Stueve et al.*, 2011]

During winter months in the seasonal snow zone, forest undergrowth is covered by snow. We can leverage this fact, and use remote sensing to quantify canopy extent without the confounding influence of undergrowth. Here, we use the term undergrowth to denote all vegetation shorter than the depth of a typical annual snowpack. Canopy measurements will exclude most shrubs and herbaceous understory, which are covered by snow, but will include the canopy area of small understory trees which do not reach the height of the forest canopy, but nonetheless extend above the snow's surface. This research utilizes the remote sensing of snow covered area (SCA) to determine canopy extent and changes to that canopy in a spatially explicit manner. This method is only applicable in the seasonal snow zone, which certainly does not include all global forests. However, snow covers up over 30% of the land surface seasonally, up to 50 million km^2 [*Vikhamar and Solberg*, 2003], and approximately 40% of global forest extent lies in the seasonal snow zone, as shown by [*Stueve et al.*, 2011] in Figure 1. Incorporation of snow has already been shown to improve automated disturbance mapping, but has not been used explicitly to map canopy extent [*Stueve et al.*, 2011]. In North America, forests cover 40% of the seasonal snow zone [*Klein et al.*, 1998].

1.2 Beetle-caused mortality changing western forests

Since the mid-1990s, outbreaks of aggressive bark beetles have caused extensive forest mortality across over 600,000 km^2 of North-American forests [*Bentz et al.*, 2009; *Meddens et al.*, 2012]. The impacts of the mountain pine beetle (MPB) have been especially severe, killing trees across 71,000 km^2

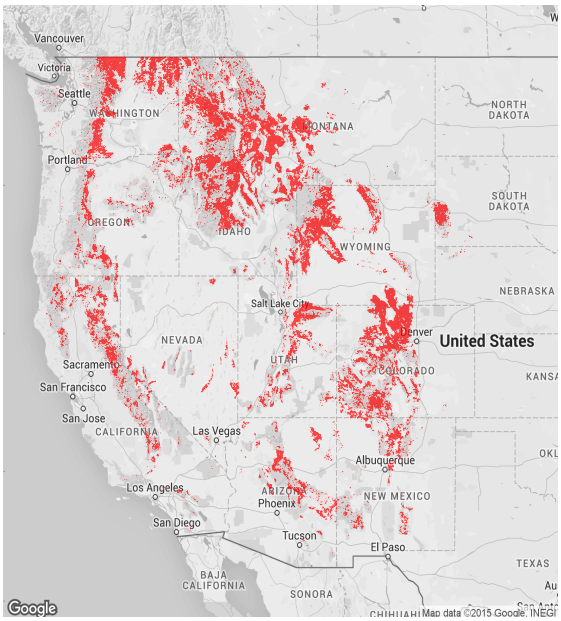

Figure 2: Areas impacted by bark beetle from 1997-2012 in the western United States [adapted from Meddens, 2012].

of forest in the western US [*Hart et al.*, 2015]. In Colorado alone the mountain pine beetle has killed 34,000 km^2 of forest [*USFS*, 2015] affecting 67% of the state's lodgepole pine stands and 40% of forested watersheds, as shown in Figure 2 [*Bentz et al.*, 2009; *Pugh and Small*, 2012]. Forest mortality of this scale is of great public concern for a range of issues from timber production and tourism [*Rosenberger et al.*, 2012] to carbon sequestration [*Kurz et al.*, 2008], habitat [*Saab et al.*, 2014], hydrology [*Livneh et al.*, 2015] and water quality [*Mikkelson et al.*, 2013]. Recognizing the outsize impacts of beetle-induced mortality, congress authorized $200 million in the 2014 Farm Bill for work to reduce future outbreaks, and mediate wildfire risk on affected landscapes [*Agricultural Act of 2014*].

Though the spread of MPB is slowing, with mature pine trees depleted in the core of the outbreak as well as a dramatic reduction in newly impacted areas, the threat of new epidemic-level forest mortality is far from over. A spruce beetle (SB) epidemic is now expanding rapidly, with over 1,000 km^2 of new infection in 2014 in Colorado alone [*USFS*, 2015]. This comes as an addition to an increase in background drought-related mortality [*Allen et al.*, 2010; *Williams et al.*, 2012; *Smith et al.*, 2015] and area affected by fire [*Dennison et al.*, 2014]

Novel methods of detecting and quantifying forest mortality are needed. Though the present MPB epidemic prompted much research into remote sensing of tree mortality [e.g. *Coops et al.*, 2006; *Wulder et al.*, 2006; *Meddens et al.*, 2012; *Meddens and Hicke*, 2014], much of this work depended on either manually-collected Aerial Detection Survey (ADS) data, with known spatio-temporal limitations, or the spectral signature of red-stage mortality, which is unique to specific tree species, and can be relatively short-lived [*Johnson et al.*, 1997]. Methods of quantifying integrated mortality from multiple sources will be needed, as drought, non-MPB insect mortality, and fire continue to expand in forests across western North America.

This research seeks to develop such a method, using the 2000's-era MPB epidemic as a test case. While much time, effort, and money has been devoted to identifying areas impacted by beetle kill, the resulting impacts on canopy extent are still poorly understood. Widespread tree mortality results in a reduction of canopy area as needles fall from dead trees, exposing more ground area to view from satellite remote sensing platforms. Using publicly-available daily satellite data on sub-pixel fractional cover of snow, vegetation, and rock, this research seeks to show a proof-of-concept for quantifying change in canopy extent associated with severe forest mortality, and to model mortality levels based upon observed changes in canopy extent. We use the 2000's-era mountain pine beetle epidemic in northern Colorado as a test case for developing this methodology. Tracking changes in canopy cover, regardless of cause – reductions due to pests, drought, fire, or even subsequent regrowth – has a multitude of potential application in the coming decades.

1.3 IMPACT OF TREE MORTALITY ON SNOW AND WATER RESOURCES

Beetle-caused tree mortality is apparent, extensive, and has resulted in the disappearance of forest canopies across western North America. This has, in turn, exerted strong controls on the accumulation and melt of the seasonal snowpack. In the semi-arid Western United States, where approximately 70-80% of total annual runoff originates as mountain snowmelt, it is important to understand how beetle infestation, and corresponding changes to forest canopies and patterns of snow accumulation and melt, have changed dynamics of water availability [*Pugh and Small*, 2012]. Beetle-caused tree mortality across the west has been centered in the seasonal snow zone, where pine species most susceptible to beetle impact are typically found. The hydrologic impacts of this large-scale landscape change will last for decades; understanding how beetle infestation

changes the timing and quantity of water availability will be important for both short and long-range planning.

Canopy cover strongly impacts the dynamics of both snow accumulation and melt; changes caused by beetle kill are observed in snow accumulation and melt [*Varhola et al.*, 2010; *Pugh and Small*, 2013; *Winkler et al.*, 2014; *Welch et al.*, 2015]. With a reduction in canopy cover, needles and branches intercept less snow. Much of the snow intercepted in the canopy sublimates, never reaching the ground. Canopy removal results in more snow reaching the ground, yielding greater snow accumulation. This increased accumulation, however, is balanced by two factors: increased solar radiation and wind speeds in dead forests. Reduced shading allows more direct shortwave to reach the snow surface, resulting in faster melt. Increased wind speeds result in increased winter sublimation of the snowpack, reducing maximum accumulations [*Varhola et al.*, 2010; *Ellis et al.*, 2011]. These competing processes impact maximum snow accumulation, melt rates, timing of snow disappearance, and soil moisture dynamics [*Bewley et al.*, 2010; *Harpold et al.*, 2013].

Changes in snowmelt persistence and rate of melt have cascading impacts on society and mountain ecosystems [*Bales et al.*, 2006]. Water managers depend upon snowmelt-derived water during the summer months, a time when demand is typically highest, and supply is lowest. Recent work has shown that beetle kill increases late-summer groundwater contributions 15-45%, due to reduced evapotranspiration, but notes that changes in snowmelt processes may offset this effect [*Bearup et al.*, 2014]. In a time of increasing demand for and conflict over water, as population grows and a changing climate impacts typical basin hydrographs, knowledge of runoff and water-input timing to streamflow is increasingly critical. Being able to anticipate the timing of snowmelt is important in order to make well-informed water

management decisions, maximize utility of existing infrastructure, and anticipate water supply changes under atypical snow conditions— either high or low – or with altered melt timing.

Snow influences watershed hydrology and ecology far beyond the simple contribution of snow to runoff. Snowmelt exerts large influence on biogeochemical cycles, especially nitrogen cycling [*Bowman*, 1992; *Brooks et al.*, 2011]; supplies water for vegetation green-up, survival, and productivity [*Fagre et al.*, 2003; *Trujillo et al.*, 2012], and is often a dominant influence on soil moisture [*Molotch et al.*, 2009; *Williams et al.*, 2009]. Trees change wind patterns, creating sheltered areas of accumulation where present, and leaving scoured areas where less canopy is present. This is often a dominant control on spatial patterns of snow accumulation, and thus plant communities [*Winstral et al.*, 2002; *Erickson et al.*, 2005]. Loss of canopy associated with beetle kill will impact these biogeochemical and ecological processes.

While we know that the pine beetle has impacted over 600,000 km^2 of forest in western North America since the mid-1990s [*Bentz et al.*, 2009], the precise impact on extent of canopy cover has not yet been documented. At the plot scale, it has been shown that a beetle infestation in Grand County, Colorado reduced canopy cover by 8%, and leaf area index by 30% [*Pugh and Small*, 2012]. In British Columbia, another plot-scale study showed a canopy cover reduction of 8% in a young pine stand, during one year of a beetle-kill phase [*Winkler et al.*, 2010]. These corresponded to an increase in maximum snow water equivalent (SWE) accumulation of 11-21% in the Colorado study, and 74% in the Canadian study, [*Boon*, 2007; *Pugh and Small*, 2012]. This range of effects is a natural result of differences in initial conditions, particularly size of gaps in relation to canopy height, and snowfall dynamics in the years studied. Applied at the watershed scale, these changes have large hydrologic consequences.

Changes in canopy due to MPB cannot reliably be projected to other forest types; spruce beetle (SB) and drought mortality affect a much more variable profile of tree composition than do MPB, and the magnitude of these changes are likely species-specific [*Cade*, 1997; *Liu et al.*, 2008]. With the recent expansion of regional drought-related mortality [*Williams et al.*, 2012], the nascent SB epidemic [*Hart et al.*, 2015], and an increase in annual area burned [*Dennison et al.*, 2014], there is a need for new methods of quantifying change in canopy – regardless of cause.

1.4 Potential for remote sensing of canopy in winter

When viewed from above, the forest canopy shows a much greater contrast with snow than with summertime understory and soil; the greenness of coniferous canopy and forest understory can often be quite similar. Satellite-based retrievals of leaf area index (LAI, measured as leaf area per area ground, or $m^2\ m^{-1}$) are insufficient to quantify canopy, as opposed to the combination of canopy and undergrowth, as the signals of the two types of vegetation greenness have proven persistently difficult to distinguish [*Coops and Wulder*, 2010; *Nolin*, 2010; *Heiskanen et al.*, 2012; *Bright et al.*, 2013; *Buma et al.*, 2013]. After a disturbance, remotely sensed LAI rebounds quickly due to an expansion of undergrowth [*Buma et al.*, 2013]. Novel techniques are needed that separate over and understory impacts to track forest recovery, and aid in accurate forest modeling – for purposes ranging from hydrologic modeling, to carbon cycling and fire fuels predictions. Additionally, within-crown gap fractions account for approximately 15% of the total viewable gap fraction (VGF) at nadir, meaning that areal estimates of canopy cover ingested into land-surface models likely underestimate within-forest radiation transmissivity [*Liu et al.*, 2008]. Using spectral unmixing to estimate canopy may theoretically overcome this issue, as the reflectance from snow through canopy gaps should be captured.

In winter months, when forest undergrowth is covered in snow, the spectral signature of forest canopy is quite different from that of the VGF; this is less true during times of year when the VGF is composed of soil and undergrowth. The Moderate-Resolution Imaging Spectroradiometer (MODIS) satellite provides a platform that can distinguish sub-pixel coverage of the land surface, differentiating vegetation, soil, and snow [*Painter et al.*, 2009]. Changes in the relative proportions of these landsurface endmembers through time, especially during winter snow-covered months, hold the potential to identify changes in forests through time, and over large spatial extents.

This research utilizes the MODIS Snow-Covered Area and Grain size product (MODSCAG) to quantify canopy extent. MODSCAG returns the fractional area composed of snow (F_{SCA}), vegetation (F_{Veg}), and rock/soil (F_{Rock}) in a pixel at a 500m spatial resolution, and is available at a daily time-step [*Painter et al.*, 2009]. MODSCAG is derived through spectral-unmixing analysis, resolving fractional area by finding the best linear combination of land surface endmembers from a spectral library of observations acquired in both the field and laboratory. For a detailed description of MODSCAG, refer to the Background section of this thesis. MODSCAG is chosen as opposed to MOD10A1 fractional snow cover (another commonly used MODIS snow product), due to its superior performance in forests [*Rittger et al.*, 2013; *Micheletty et al.*, 2014].

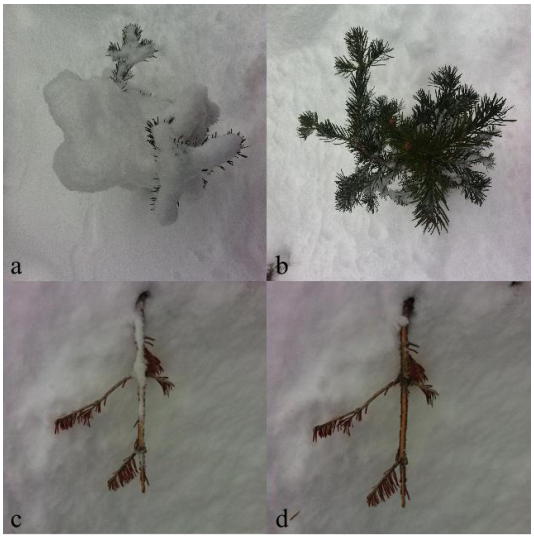

Figure 3: Live and dead spruce saplings viewed from above in winter. When the vegetation is free of snow, F_{SCA} is equivalent to the VGF [*Liu et al.*, 2008]. This is true in both live (b) and dead forests (b). When snow is intercepted in the vegetation, F_{SCA} is elevated (a & c).

The shape of an annual MODSCAG

timeseries during winter months gives information on canopy extent; briefly, select dips or local minima in the timeseries are representative of snow-free canopy conditions, and can be used to quantify fractional canopy extent (F_c). This is independent of forest morality, or disturbance agent, as shown conceptually in Figure 3. At times where F_{SCA} is at a minimum, F_C is at a maximum. This is shown in panels b & d of Figure 3. At these times, F_{SCA} can be used to measure the canopy gaps. A detailed description of this methodology is given in the Methods section of this thesis. Canopy cover is quantified on an annual basis; changes are observed without respect to cause: beetle kill, other forest mortality, harvest, or regrowth.

1.5 Research Questions

This research uses the recent pine beetle epidemic in Northern Colorado as a test case for detecting forest change. It seeks to address the following questions:

1) Is it possible to quantify the distribution of forest mortality using the remote sensing of snow?

2) What is the best method of quantifying VGF and F_c using the remote sensing of snow?

3) How long after mortality does needlefall occur? Is this spatially variable?

4) How does VGF change with mortality? What level of mortality is required to produce a given increase in VGF in lodgepole forests?

2 BACKGROUND

2.1 Importance of snow in the hydrologic cycle

Well over a billion people globally depend on snow or glacier-melt for their water, and people in these areas generate around 25% of the world's Gross Domestic Product [*Barnett et al.*, 2005]. Seasonal snowpacks store water from winter precipitation, and release it in the summer months when demand from municipal, agricultural, recreational and environmental

users are generally highest [*Bales et al.*, 2006]. In the semi-arid Western United States, snowmelt is the largest component of water in most river basins, supplying water for over 60 million people [*Troendle*, 1983; *Barnett et al.*, 2005; *Bales et al.*, 2006]. Decision systems for water allocation are based upon the assumption that the bulk of annual precipitation will fall in winter, be stored in the snowpack, and melt over the spring and summer, thus moderating the pulse of annual streamflow. This assumption underpins much of current water management: water laws and markets, international treaties, flood control infrastructure, hydropower design, interstate compacts, dam operations, and the basic ability to meet water demands of industry, agriculture, and municipalities [*Bales et al.*, 2006].

Additionally, snowmelt largely determines the timing and length of the spring freshete, the time when water becomes plant-available in the spring. The size of the annual snowpack controls forest growth and greenness [*Trujillo et al.*, 2012] and the timing of melt determines the length of drought-stress on vegetation, by setting the end date of water input before summer rains begin [*Kelly and Goulden*, 2008]. North American forests play a large role in the continental carbon cycle; the effect of snowmelt on forest growth and greenness in montane forests controls many important parts of this net ecosystem exchange [*Sacks et al.*, 2007].

2.2 Remote sensing of snow

Mapping snow covered area from satellites has a long history, using many remote-sensing platforms. It is needed for many applications, from understanding global-scale climate feedbacks to small-scale water availability and flooding potential in individual basins, among many others. Satellite remote sensing allows measurement of snow cover in a consistent, spatially extensive manner. It has a long history, reaching back to the 1960s, with the very earliest images of earth taken from space [*Singer and Popham*, 1963; *Dietz et al.*, 2012]. Due to its high albedo, snow

shows a good contrast with most other land surfaces, with the exception of clouds. Many different sensors have been used to map snow though the satellite era, employing various spectral algorithms. Distinguishing cloud cover from snow remains a persistent problem.

2.2.1 BINARY IDENTIFICATION: SNOW-COVERED OR SNOW-FREE

In early analysis, contrast between the brightness of snow in the visible spectrum and darkness of snow in the shortwave infrared, where clouds remain generally bright, was used to discriminate clouds from snow [*Crane and Anderson*, 1984]. In the mid-1970s, Rango and Martinec used this contrast to map snow and run the Snowmelt-Runoff Model with Landsat data [*Martinec*, 1975]. Work in the 1980s formalized the visible – shortwave infrared band contrast as the Normalized Difference Snow Index (NDSI). It was initially developed for Landsat, to perform a binary classification for pixels as either snow-covered or snow-free on a pixel-by-pixel basis, thus accounting for variable illumination in mountainous terrain; in equation 1, R is surface reflectance in visible and shortwave infrared bands [*Dozier*, 1989].

$$NDSI = \frac{R_{visible} - R_{shortwave-infrared}}{R_{visible} + R_{shortwave-infrared}} \quad (1)$$

Table 1: MODIS Land Bands

MODIS Band	Bandwidth
1	620-670 nm
2	841-876 nm
3	459-479 nm
4	545-565 nm
5	1230-1250 nm
6	1628-1652 nm
7	2105-2155 nm

With the launch of AVHRR in 1982, snowcover could be mapped daily at a 1km resolution. The launch of MODIS in late 1999 added four additional land bands not present on AVHRR, and reduced resolution to 500m, also mapping snow globally on a daily basis. Mapping of snow cover using MODIS began with simple detection of binary snow presence or absence, classified using an NDSI index, using MODIS Terra (or Aqua) bands listed in equation 2; shortwave infrared bands used are different depending on the satellite, due to broken sensors in

Aqua's band 6 [*Salomonson and Appel*, 2004; *Hall and Riggs*, 2007]. MODIS band numbers and spectral ranges are given in Table 1.

$$NDSI = \frac{b_4 - b_{6\,(7)}}{b_4 + b_{6\,(7)}} \tag{2}$$

NDSI automatically discriminates snow from cloud, using an empirically-derived cutoff of NDSI > 0.4 [*Hall et al.*, 2002; *Hall and Riggs*, 2007]. In forested areas, the NDSI threshold must be decreased to avoid errors of omission, as forest canopy obscures and shadows substantial amounts of snow cover. NDSI values < 0.4 indicate snow if the normalized difference vegetation index (NDVI) is near 0.1, as snow tends to lower the NDVI [*Hall et al.*, 2002]. Thus, a NDVI value close to 0.1 is a good indication of snow, even where NDSI > 0.4, which reduces problems mapping snow cover in forested regions. To reduce false positives in areas with dark landcover, which creates a small denominator in the NVDI equation, the reflectance in the visible band 4 is required to be > 0.1 in order to be mapped as snow [*Klein et al.*, 1998]. This approach works to map pixels as snow-covered which contain at least 50% snow [*Hall et al.*, 2002] .The algorithm is implemented by NASA operationally, and distributed as MOD10A (binary) at http://modis.gsfc.nasa.gov .

2.2.2 Fractional snow cover

Classifying a 500 m MODIS pixel as either snow-covered or snow-free misses inherent subpixel variability, especially in mountainous environments, and results in overestimates of snow cover at higher elevations, while missing snow at low elevations and during spring and early summer melt [*Dozier et al.*, 2008]. To overcome this issue of scale, multiple approaches have been developed to determine sub-pixel fractional snow cover. Building on earlier binary

work using NDSI, Salomonson & Appel [2004] developed an empirical relationship between NDSI and sub-pixel snow covered area for MODIS, taking the form:

$$F_{SCA} = -0.01 + 1.45\ NDSI \quad (3)$$

The relationship was developed with a Landsat 30 m NDSI-based binary snow cover validation dataset [*Dozier*, 1989]. This algorithm is currently processed and distributed by NASA as MOD10A1-fractional, available at http://modis.gsfc.nasa.gov.

Though this empirical relationship has proven useful, it fails to account for variable grain size of snow, and potential impacts of different land cover types (e.g. organic soil vs. granitic rock outcrops) at the sub-pixel scale, which may impact NDSI values, and thus an empirically-derived estimate of F_{SCA}. With the development of imaging spectroscopy in the early 1990's, a new approach for quantifying F_{SCA} using the full-spectrum reflectivity of various land cover types became possible.

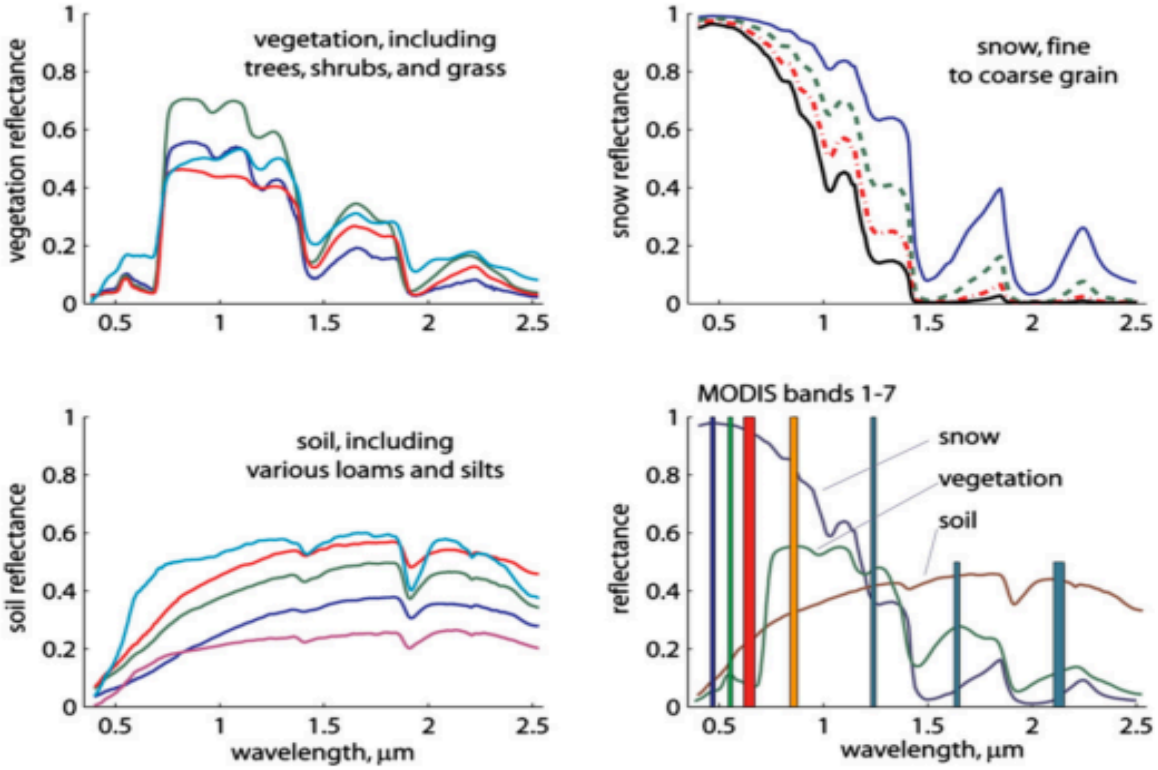

Figure 4: Spectral reflectance of vegetation, snow, and rock, overlain with the 7 MODIS land bands in the lower right panel [*Painter et al.*, 2009]

Imaging spectroscopy allows for simultaneous solution of fractional snow cover and grain size, and can account for sub-pixel variability in other land cover types. It uses the shape of surface reflectance curves, rather than absolute values in specific bands, to solve for sub-pixel fractional land cover. Initially developed using Airborne Visible/ Infrared Imaging Spectrometer (AVIRIS) data [*Painter et al.*, 2003], it has since been modified for global-scale daily FSCA estimates using MODIS data [*Painter et al.*, 2009]. Example spectra showing the distinctive shapes of vegetation, snow and soil spectra are shown in Figure 4 along with the MODIS land bands which can be used to distinguish these characteristic shapes and resolve sub-pixel fractional coverage [*Painter et al.*, 2009].

Utilizing surface reflectance data in the visible, near infrared, and shortwave infrared bands, MODSCAG returns the fractional snow covered area (F_{SCA}), vegetation (F_{Veg}), and rock/soil (F_{Rock}) in a pixel at a 500 m spatial resolution, at a daily time-step [*Painter et al.*, 2009]. The physically-based MODSCAG algorithm considers a library of land surface endmembers (i.e. snow, rock, soil, and vegetation) acquired in both the field and laboratory, and solves for the linear combination of two of more with the smallest error, and fewest number of endmembers, as compared with the base MOD09GA surface reflectance product:

$$R_{S,\lambda} = \sum_{i} f_i R_{\lambda,i} + \varepsilon_\lambda \tag{4}$$

where $R_{S,\lambda}$ is the mean surface reflectance from MOD09GA in wavelength λ, f_i is the fraction of pixel composed of endmember i, $R_{\lambda,i}$ is the surface reflectance of endmember i at wavelength λ, and ε_λ is the residual error at λ for the combination of all endmembers.

The MOD09GA surface reflectance product provides estimates of surface spectral reflectance in all MODIS land bands as would be measured at ground level, corrected for

atmospheric scattering and absorption that has occurred between ground surface and instrument. Base corrections include those for atmospheric gases and aerosols, and a cloud-state variable, though this has remaining errors of both omission and commission [*Hall and Riggs*, 2007].

MODSCAG uses reflectance values from the MODIS Terra satellite exclusively, not Aqua. This gives a morning overpass in the northern hemisphere, assuring relatively consistent illumination angles, and reducing this variability in the spectral unmixing procedure. Solution of F_{SCA} and grain size are simultaneous, as the spectrum of a mixed pixel is sensitive to snow grain size; snow of varying age and albedo will not affect estimates of F_{SCA} [*Rittger et al.*, 2013]. If one of these endmembers is snow, then the F_{SCA} is calculated as the initial solution of $F_{SCA,}$, normalized by shade fraction, due to terrain or vegetation in the pixel [*Painter et al.*, 2009; *Raleigh et al.*, 2013]. Cloudy pixels are flagged with base MOD09GA, as well as with custom band thresholds; this process is still in development. Grain size was initially used to filter clouds (with large grain size possible indicating snow incorrectly mapped as cloud, and small grain sizes possibly indicating cloud mapped as snow), but was found to miss substantial snow cover in rocky pixels. The lower limit of detection is 0.15, or 15% of the pixel. MODSCAG uses the relative shape of spectra, instead of absolute values, which allows confidence even in steep terrain where solar illumination angle can be uncertain due to co-registration errors between DEM and reflectance data. Pixel-weighted average root mean squared error (RMSE) for snow covered areas during model validation was found to be 5%, ranging from 1-13% [*Painter et al.*, 2009]. MODSCAG is publicly available for download through NASA's Jet Propulsion Laboratory at http://snow.jpl.nasa.gov.

2.2.3 *SNOW PRODUCT COMPARISON*

Empirically-derived estimates of F_{SCA} (MOD10A) have been found to perform worse than spectral-unmixing approaches (MODSCAG) in forested environments and in transitional snow seasons (early winter and late spring, and by extension potentially areas of mixed-pixel

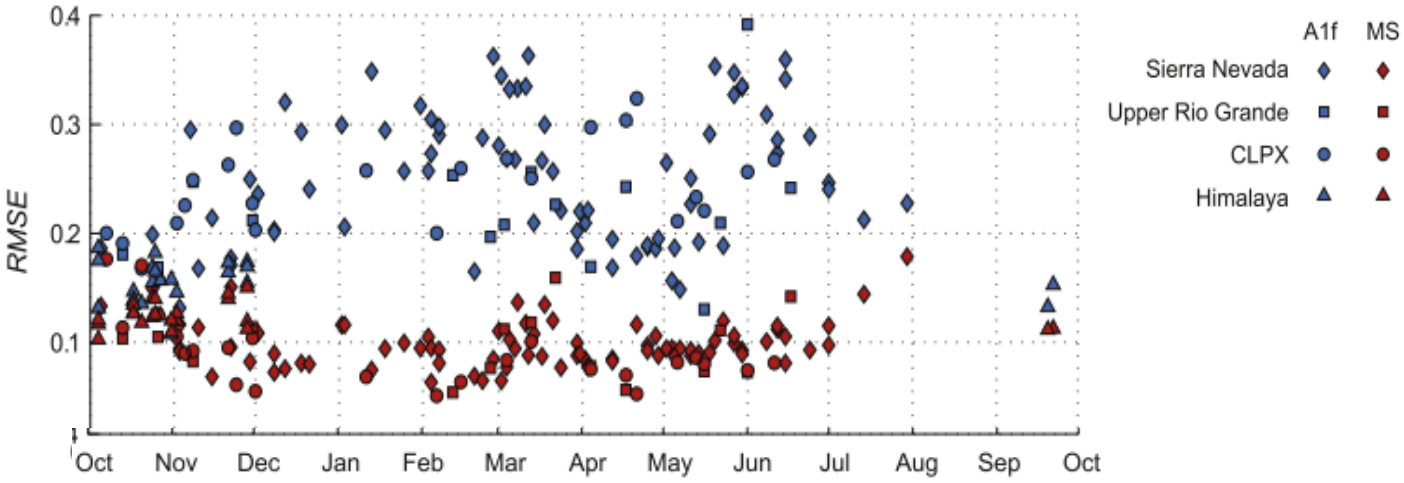

Figure 5: Seasonal and regional variability of F_{SCA} error in MODSCAG (red) and MOD10A fractional (blue), as compared to Landsat-derived fractional snow cover [*Rittger et al.*, 2013].

landcover with lower snow fractions as well). A comparison of error in MODSCAG and MOD10A are shown in Figure 5. MOD10A is biased high, commonly overestimating FSCA by > 20% [*Rittger et al.*, 2013]. The overestimation of F_{SCA} by MOD10A in densely forested areas persists following disturbance [*Micheletty et al.*, 2014]. This is likely due to the empirically defined NDVI threshold in the MOD10A algorithm which is used to identify snow in forested areas [*Klein et al.*, 1998], and does not differentiate among vegetation types within the pixel.

Thus, the best contemporary product for use in quantifying F_{SCA} in forested areas on a daily basis is MODSCAG, which returns sub-pixel F_{SCA} at a 500 m resolution [*Painter et al.*, 2009; *Rittger et al.*, 2013; *Micheletty et al.*, 2014]. Landsat-based products are available at higher spatial resolution, but are available much less frequently, and are not generally publicly available, or produced operationally.

2.2.3.1 Spline Interpolation for Gaps

Daily data from MODSCAG contain gaps and errors from cloud cover, poor viewing geometry, noisy reflectance data, and imperfections in the retrieval algorithm. This leaves gaps in the data which, depending on the intended use, may or may not be an issue. The research presented in this thesis tests and compares two approaches for use in quantifying canopy cover. The first approach uses raw MODSCAG values of F_{SCA}, F_{Rock}, and F_{Veg}, and simply utilizes only those with good viewing geometry, (< 30°, following Liu et. al [2008]) and no clouds or errors; this yields large temporal gaps in the data, but is not necessarily an issue when used to parameterize canopy extent, when a few values per year will suffice – if of high quality. The second approach applies a per-pixel temporal spline interpolation, following Dozier [2008] and Dozier and Frew [2009]. The spline is implemented on a timeseries of either raw F_{SCA} or raw $F_{SCA} + F_{Rock}$, and applied on a yearly time limit. The resulting spline is a weighted combination of a least-squares fit and cubic spline, depending upon length of gaps in available data, and weighted according to the cosine of sensor view zenith angle and sensor-view pixel size. Near nadir MODIS overpasses have the greatest weight. This research does not necessarily require daily data; thus, we test if native MODSCAG returns at low zenith angle introduce less error than implementing a spline for modeling canopy cover.

2.2.3.2 Impact of forests on F_{SCA} returns

Satellite-based remote sensing platforms view projected area, or area incorporated in the field of view at which the sensor is viewing a given location. In forests, tree canopies obscure the ground. In high-density forests, or at higher sensor zenith angles, canopies can obscure snow completely. Rittger [2013] puts the limit of detection at 60% canopy cover, as identified in the National Land Cover Dataset (NLCD) [Homer et. al, 2007], noting that shading of thicker

canopies affects the mixing model as well. At 30°, VGF is under half that it would be at nadir [*Liu et al.*, 2008]. Remote sensing of snow in forests, especially those with a dense canopy, presents a significant difficulty. In beetle-impacted areas, the remote sensing of F_{SCA} should improve as needles fall, and the VGF increases.

2.3 FOREST COVER CONTROLS ON SNOW ACCUMULATION

Forest structure has important hydrological impacts, especially in snow-dominated basins. Canopy cover exerts strong control on the accumulation, persistence, and melt of snow [*Musselman et al.*, 2008, 2012; *Varhola et al.*, 2010; *Lundquist et al.*, 2013]. Forest structure affects the amount of precipitation that reaches the ground and greatly alters the energy balance at the ground's surface, through shading of the snowpack, altering site micrometeorology (wind, humidity, and vapor pressure), and changing the albedo of the snow surface itself.

Forest cover influences the distribution of snow through several competing canopy processes. Interception of snowfall by branches and increased long-wave radiation from vegetation decrease accumulation, while shading of the snowpack from shortwave solar radiation inputs increases accumulation [*Boon*, 2007; *Essery et al.*, 2008; *Teti*, 2008]. Interception of snowfall by forest canopy in an individual storm ranges from 25-45% of snow, depending on tree species and forest density [*Molotch et al.*, 2009; *Harpold et al.*, 2013]. Snowfall intercepted by canopy is sublimated, and is thus removed from the plot or basin of interest, though this relationship is modulated by needleleaf area and albedo of the specific tree type, air temperatures, and wind movement through the forest [Hedstrom &Pomeroy, 1998; Winkler & Moore, 2006]. Broadly, synthesis of many field studies shows that forest cover explains 57% of variance in snow accumulation, and 72% of variance in snow melt in studies across forested portions of the northern hemisphere [*Varhola et al.*, 2010].

Conventional wisdom holds that higher forest density corresponds to higher interception and less accumulation, with lower melt rates and later snow disappearance due to surface shading [*Varhola et al.*, 2010]. However, cases exist that do not follow this pattern, where reduction of incoming solar energy by trees is overwhelmed by the increase in long-wave radiation from forest cover [*Sicart et al.*, 2008; *Lawler and Link*, 2011]. The effects of longwave are most likely to dominate in cases where snow albedo is high, solar elevation is low, atmospheric emissivity is low, and on pole-facing slopes; in short, cases where shortwave radiation is not the dominant driver of melt [*Sicart et al.*, 2004; *Ellis et al.*, 2011]. The relative size of longwave energy inputs from the canopy to reduction of shortwave solar energy by canopy is governed by tree height, size of canopy gaps relative to tree height, and solar zenith angle; thus, it can vary through the accumulation and melt seasons [*Sicart et al.*, 2004; *Molotch et al.*, 2011].

In forested areas, peak snowpack accumulation decreases, and rate of ablation decreases, compared to adjacent open locations. The relationship between snowmelt rate and canopy cover is modulated by other factors affecting the quantity of incoming shortwave radiation– elevation, aspect, slope, and latitude [Varhola et al., 2010]. Site-specific work confirms increased accumulation and faster melt in open relative to forested sites: a study in Colorado and New Mexico found 29% greater accumulation in open versus under-canopy locations [*Molotch et al.*, 2009]; and an increase in ablation rate of 33% was observed in Canada [*Spittlehouse and Winkler*, 2005]. These findings are fairly representative: as a general rule, less snow accumulates under the forest canopy, where it also melts more slowly [*Musselman et al.*, 2008; *Varhola et al.*, 2010]. The effect of forest cover on snow disappearance date is variable; it depends rather on whether the faster rate of melt is balanced by a larger snowpack [*Molotch et al.*, 2011].

Recent meta-analysis of plot-scale studies attempted to delineate areas where snow disappears first under trees from areas where it melts first in clearings, using mean winter temperatures [*Lundquist et al.*, 2013]. They found that in areas where mean December—February temperatures are over -1 ° C, forest cover reduces snow duration by 1-2 weeks, compared to nearby clearings [*Lundquist et al.*, 2013]. This is a general rule, however, and does not hold true for all plot-scale locations [e.g. *Musselman et al.*, 2008]. Latitude, controlling intensity of incoming shortwave radiation, and annual climatic conditions contributing to turbulent energy transfer are an important consideration when determining how forest cover will affect annual snowpack accumulation and melt.

Pine beetle infestation reduces canopy coverage over the course of an infestation from full branches to bare grey limbs. Loss of canopy from any cause, including beetle infestation, is known as defoliation; it impacts patterns of snow accumulation and ablation as discussed more generally above, through changes in interception, and by modifying the snow-surface energy balance. Quantifying changes in canopy in a spatially explicit manner, as accomplished in this research, allows for inferences on changing accumulation and melt patterns associated with forest disturbance.

Sublimation is a strong control on wintertime snowpack accumulation; it is a highly complex process in forested environments, complicated by variability in incident solar radiation at the snow surface, longwave radiation from trees and the ground, albedo of tree needles, and site-specific climatic constraints including temperature, wind, and solar zenith angle. Reduced canopy cover increases wind speeds, which creates sharper temperature and humidity gradients near the snow surface, increasing sensible and latent heat fluxes to the snowpack and rates of sublimation [*Boon*, 2007, 2009]. Vapor losses of 40-50% of total snowfall prior to peak

accumulation are common [*Molotch et al.*, 2007, 2009; *Harpold et al.*, 2013]. A reduction of forest canopy following a beetle epidemic will increase the amount of shortwave radiation at the snow surface, and increase typical wind speeds, accelerating sublimation. This increase in sublimation may be balanced to a small degree by decreased interception vapor losses, which enhance snow through-fall volumes [*Biederman et al.*, 2012; *Harpold et al.*, 2013]. Recent LiDAR-based work suggests open areas near trees (< 15m) retain 30-40% more SWE than locations under the canopy, and 10-25% more than open areas far from trees (> 15m) [Broxton et. al, 2014].

2.4 STAGES OF BEETLE KILL & BIOLOGICAL CYCLE OF THE MOUNTAIN PINE BEETLE

Beetle kill progresses through three stages: green, red, and grey. In the green stage, beetles have infected the tree, but have not yet caused changes to needle color or extent. Green-stage infestation can be detected through changes in the normalized difference vegetation index (NDVI), but cannot be seen with the naked eye, and is not recorded in aerial detection surveys [*Meddens et al.*, 2013]. The green stage typically lasts one year [*Pugh and Small*, 2012], before progressing to red stage. In the red stage, tree death begins, needles turn red, and begin to fall from the tree. After 2-3 years in the red stage, trees loose almost all of their needles, and are considered to be in the grey phase [*Wulder et al.*, 2006]. Needles typically fall in 3–5 years, branches in 10–15 years, and trunks begin 5 years after death [*Safranyik and Wilson*, 2006]; blowdown generally peaks 10 years after stand death [*Lewis and Huggard*, 2010]. These numbers are approximate, however, and are highly dependent on site-specific meteorological conditions, such as soil moisture and wind events [*Veblen et al.*, 1991; *Wulder et al.*, 2006; *Klutsch et al.*, 2009]. The progression of beetle kill is not uniform across a watershed, or even a stand-scale study, representing a mosaic of different beetle-kill stages and uninfected trees. Thus,

the progression of canopy-cover decline, which is an inherently heterogeneous process, can best be synthesized using remote sensing, rather than projecting canopy decline seen at the plot-scale uniformly to an entire watershed.

The mountain pine beetle (*Dendroctonus ponderosae*) preferentially targets large-diameter trees, causing extensive mortality of mature stands. Two main factors are generally accepted as having contributed to the 2000s-era expansion in the western US: drought, and a lack of extreme cold winter temperatures [*Raffa et al.*, 2008; *Bentz et al.*, 2009; *Chapman et al.*, 2012; *Williams et al.*, 2012].

Beetles generally hatch a single generation per year, attack trees in August and lay eggs which then mature into adults one year later [*Safranyik*, 2004]; this year is the green-stage of attack. Tree defenses are overwhelmed through two main mechanisms: mass attack, and the impact of beetle-carried microorganisms (primarily blue-stain fungi: *Ophiostoma clavigerum*) which beetles bring into the tree phloem as they attack) [*Safranyik et al.*, 1974].

Generally, foliage fades from green to yellow and then red over the spring and summer immediately following attack [Amman, 1982]. After twelve months, over 90% of killed trees have reached the red-attack stage; after three years, most trees will have lost all needles, leaving only dead branches and twigs (grey-attack stage) [*Safranyik*, 2004].

Timing of changes in foliage color and needlefall depends upon tree genetics, condition, and the local microclimate and environment [*Safranyik et al.*, 1974]. In a single stand, red and grey-phase mortality often overlap; small-diameter trees may not experience beetle infestation at all. These mixed-area effects complicate satellite remote sensing spectrally-based detection of beetle-caused tree mortality.

2.5 PINE BEETLE RELATED REDUCTION OF FOREST CANOPY

Plot-scale studies of pine beetle impacts on canopy cover, while limited, show a significant reduction in canopy cover from green to grey-stage beetle-caused tree mortality [*Boon*, 2009; *Pugh and Small*, 2013]. These studies are limited to uniform, pure lodgepole pine stands. Beetle infestation opens the canopy, and thins dense stands of trees. In paired-plot studies, it has been shown that a beetle infestation in Grand County, Colorado, reduced canopy cover by 8%, and leaf area index by 30% [*Pugh and Small*, 2012]. In British Columbia, another plot-scale study showed a canopy cover reduction of 8% in a young pine stand, during one year of a beetle-kill phase [*Winkler et al.*, 2010]. Another Canadian study spanning six years found that average canopy gaps increased from 27% to 49% [*Winkler et al.*, 2014].

Reduction of canopy in these studies showed a variable relationship with snow accumulation and melt, with a greater influence often exerted by annual weather than by beetle-induced mortality [*Winkler et al.*, 2014]. A study with 2 sites in southern Wyoming and the Colorado Front Range found that grey-phase plots experienced 20% lower interception than in unimpacted plots [*Biederman et al.*, 2012]. However, with a distributed snow survey, they also found no significant difference in snow accumulation between green and grey stands, meaning that these differences may only hold at small scales.

2.6 REMOTE SENSING OF BEETLE KILL

Many efforts to map beetle outbreaks with remote sensing have been made, using simple visual aerial detection surveys (ADS, typically done by the US Forest Service annually), high-resolution aerial imagery, and a variety of multi-spectral satellite remote sensing platforms; a review is given by Wudler et al. [2006].

2.6.1.1 Aerial Detection Surveys (ADS) & Meddens ADS Mortality Area (MADS-MA)

Original management efforts to track forest mortality started with simple visual mapping. Aerial Detection surveys (ADS), also known as sketchmapping, involve observers from the USFS visually estimating the number of trees killed per hectare from an aircraft, and recording these estimations manually onto a base map [*USFS*, 2015]. This has been performed annually for areas of interest since the 1940s. These surveys are widely used operationally, but are typically considered qualitative in nature [Johnson et al., 2008; McConnel et. al, 2000], and contain many issues for use in quantitative research [*Chapman et al.*, 2012; *Meddens et al.*, 2012].

ADS data are considered acceptable for coarse-scale analyses, but contain large errors at finer spatial scales. In comparison with ground surveys, 35% of sites had errors of omission in detecting mortality for lodgepole pine, and 56% in subalpine fir, where stand structures are more complex [Johnson et al., 2008]. With a spatial tolerance of 50 m, omission errors were reduced to 26% and 51%; a tolerance of 500 m further reduced errors of omission to 13% and 38%. This work indicates that ADS data captures beetle-induced mortality broadly, especially pine mortality with its signature and long-lasting red-stage, and can be useful when high spatial resolution is not required.

ADS data is limited to areas flown by the forest service in a given year – areas which are selected for management purposes, and limited by funding; they do not generally include wilderness areas and national parks where management options for pests are limited [*Johnson and Ross*, 2008]. ADS surveys report area affected by varied pests, which includes live trees as well as dead trees. Mortality area – the canopy area of killed trees – is more applicable to assessing impacts, as it differentiates areas that have changed from those which have not [*Meddens et al.*, 2012]. To address this issue, as well as known issues with ADS underestimation

of mortality, a gridded 1km^2 mortality-area product derived from a combination of ADS data, typical species-specific crown areas, and MODIS vegetation-cover indices has been developed for the Western United States and Canada: the Meddens-ADS Mortality Area (MADS-MA) [*Meddens et al.*, 2012]. This dataset is useful for a variety of purposes, as it shows where forests have been impacted, over large spatial scales. However, it has somewhat lower spatial accuracy, due to inherent issues in ADS data. Additionally, conversion of area affected, which includes both dead and live trees as collected by ADS surveys, to mortality area is quite uncertain, with a conversion factor ranging from 0.01 to 0.15 for upper and lower estimates [*Meddens et al.*, 2012]. Mortality area is distinctly different from canopy extent, and viewable gap fraction. The Meddens dataset gives the percentage of a pixel composed of tree canopy killed by specific beetle-type in a given year, but does not address the canopy-area reduction seen through the course of a beetle infestation. A yearly parameterization of canopy cover is critical for landsurface models, especially hydrologic prediction in snow-dominated catchments where canopy cover largely dictates both the maximum snow accumulation, and the surface energy balance, and thus timing and speed of melt.

2.6.1.2 Spectral Detection

Detection of forest mortality using multi-spectral satellites sidesteps the issue of observer subjectivity and the spatial limitations inherent in ADS-derived measures of forest mortality. Much progress has been made on spectral detection of beetle-induced mortality. Spatial accuracy and estimates of timing have higher confidence than ADS-derived data. Therefore, this research uses the spectrally-identified, Landsat-based mortality area developed for an area in Northern Colorado and Southern Wyoming for our validation dataset [*Meddens and Hicke*, 2014]. We will refer to this dataset as the Meddens Landsat Mortality Area (MLMA); it quantifies the severity and location of bark-beetle-caused tree mortality on an annual basis [*Meddens and Hicke*, 2014].

The MLMA data gives the percent mortality of forest canopy within a 30 m Landsat pixel – this is easily conceptualized as the canopy area of killed trees. The amount of canopy lost should theoretically correspond very closely with the percent canopy area of dead trees; only dead canopy will be lost, and remaining live trees and open area should not change with increasing mortality.

The MLMA data was developed in three distinct steps, which are described in detail below. Step one used field plots of tree mortality stage (green, red, or gray) to develop a method of classifying stage in high-resolution (30 cm), multi-spectral, aerial imagery [*Meddens et al.*, 2011]. Step two used this classified aerial image to develop a Landsat-based (30 m) strategy for spectral classification of red-stage mortality, creating yearly maps of red-stage trees, undisturbed forest, and herbaceous understory [*Meddens et al.*, 2013]. Step three developed a model to predict percent mortality within a Landsat grid cell, going beyond simple stage classification. The classification map from step two was used to mask no-forest pixels prior to model building, and to select pixels with red-stage mortality that could then be used for model-building in step three. The classification map developed in step one was used to calculate class proportions in each pixel (the percentage of each class within the 30 m Landsat pixel), and this percent red stage mortality was then used as the response variable for model building in step three [*Meddens and Hicke*, 2014]. Step three produced annual maps of percent red-stage mortality over the entire Landsat scene.

Step 1 begins with classifying aerial imagery using reference field assessments. Though the final MLMA product is remote-sensing based, the method is anchored by a plot-based field assessment of tree mortality stage. Meddens et. al [2011] used 36 fixed plots to develop a classification scheme for multi-spectral, high-resolution aerial imagery. The scheme is consistent

across cover types and forest compositions, including Engelmann spruce, subalpine fir, lodgepole pine, occasional aspen trees, and open meadows. They used a band/index combination of green, red-green index (RGI), and the normalized difference vegetation index (NDVI) for stage classification, employing a maximum likelihood classifier approach. Landsat bands are given in Table 2. The RGI is simply the ratio of the red (B3) to green (B2) wavelengths; NDVI is difference in near-infrared and red divided by their sum : (B4−B3)/(B4+B3).

Table 2: Landsat bands and spectral regions, adapted from Meddens [2011].

Sensor	Landsat 5	Landsat ETM+
Band 1 (B1: blue)	0.45–0.52	0.45–0.515
Band 2 (B2, green)	0.52–0.60	0.525–0.605
Band 3 (B3, red)	0.63–0.69	0.63-0.69
Band 4 (B4, near infrared)	0.76–0.90	0.75–0.90
Band 5 (B5, near infrared)	1.55–1.75	1.55–1.75
Band 6 (thermal)	10.40–12.50	10.40–12.50
Band 7 (middle infrared)	2.08–2.35	2.09–2.35

This yielded an overall pixel-level accuracy of 90%, as compared to field-based tree classification. Occasional errors (10%) resulted from misclassification of sunlit crowns of live trees with herbaceous understory, and misclassification of sunlit crowns of grey and red trees with bare soil. Aggregating high-resolution imagery to 2.4 m, instead of native 30 cm, prevented many areas of brightly-lit crowns from being misclassified as grey, and red trees misclassified as bare soil, as pixels at this resolution included more shadow in forested areas decreasing visible-spectrum brightness.

Using the classified aerial imagery developed in Step 1, in Step 2 Meddens et al. [2013] develop a method for classifying mortality stage in late-summer Landsat satellite imagery. Forested areas were identified using tasseled cap greenness (TCGRE), with TCGRE < 1.1 indicating forest. Inside this forest mask, annual grids of beetle-induced mortality were produced using anomalies from a site-specific beginning undisturbed mean in a radiometrically normalized

Landsat Band5/ Band4 ratio (B5/B4 anomaly > 0.018 indicating disturbed, red-stage forest mortality).

While the distributed dataset uses the B5/B4 anomaly with multi-date methods, the use of these multi-date methods (following pixel trajectories through time) did not significantly improve accuracy of classification from single date methods (90% vs. 91%) [*Meddens et al.*, 2013]. The spectral indices yielding highest classification accuracy differed between multi-date and single-date classifications. Single-date had the highest accuracy using a combination of three tasseled cap indices: tasseled cap brightness, tasseled cap greenness, and tasseled cap wetness. With these spectral indices, pixels are classified as either red-stage, undisturbed, or herbaceous understory using maximum likelihood classification. This classification produced annual gridded maps of red-stage mortality, giving location of dead trees and year of red-stage mortality.

Following classification of a pixel as red-stage, step three consists of a multiple linear regression model, used to predict percent red stage canopy in the Landsat pixel for each year identified as red-stage by the spectral index anomaly in step two. The model predicts percent mortality with a combination of Landsat Band 1 (B1), the Normalized Difference Vegetation Index (NDVI) and the B5/B4 anomaly, and has an overall mean r^2 of 0.77 [*Meddens and Hicke*, 2014].

The MLMA gives mortality area of canopy within a grid cell; an area with few trees will certainly have a low MLMA, even if all trees within the cell are dead. In order to compare to our measurements of canopy extent, the MLMA does not need to be adjusted for variable forest density, or basal area. Rather, both our local-minima approach and the MLMA do not contain implicit assumptions on forest extent; they measure area of canopy mortality, and area of canopy directly and in the spatial patterns in which they occur. This dataset represents the highest-

accuracy remotely-sensed dataset on beetle-induced mortality in lodgepole pine forests; its only limitation, in relation to the MADS-MA, is the spatial extent for which it is available. The method is repeatable, and anchored in field measurements. Though these field assessments are far removed from the final dataset, it is hard to envision a way to include more robust field validation for a dataset spanning almost a quarter of Colorado.

2.7 REMOTE SENSING OF BEETLE IMPACTS

Satellite observations in recent years have been successfully used to document bark beetle impacts to a suite of land surface characteristics. MODIS products showed bark beetle impacts decreasing leaf area index (LAI)1-40%, gross primary productivity (GPP) 5-26%, daily summer evapotranspiration (ET) 13-44%, and increasing August land surface temperature (LST) 1-3.9° C in northern Colorado and southern Wyoming over a range of beetle impact severity [*Bright et al.*, 2013]. MODIS estimates of LAI and GPP are unable to distinguish canopy and understory vegetation [*Coops and Wulder*, 2010; *Xiao et al.*, 2011; *Heiskanen et al.*, 2012; *Buma et al.*, 2013]. Rather, MODIS estimates of LAI and GPP may capture initial reductions following a forest disturbance, and a quick recovery capturing an increase understory growth, but obscuring knowledge of post-disturbance canopy conditions [*Bright et al.*, 2013]. Additionally, MODIS products assume a fixed land cover type in calculating LAI and GPP, which could also contribute to errors following a disturbance.

Recent work has shown that forest disturbance changes the distribution of snow cover values in a given area over the course of a winter season, with removal of the canopy resulting in a significantly higher suite of F_{SCA} values [*Micheletty et al.*, 2014]. Following the removal of forest canopy by fire in a basin in California, the number of days exceeding the pre-fire high snow-cover threshold increased by 81%; F_{SCA} following fire was also significantly higher in the

burned area than in an analogous unburned neighboring basin. Melt-out dates were delayed as well [*Micheletty et al.*, 2014]. This work illustrates the ability of snow covered area remote-sensing products to capture land cover changes at basin-wide scales, and additionally demonstrates the superiority of MODSCAG over MOD10A in forested areas [*Micheletty et al.*, 2014].

Additionally, utilizing F_{SCA} has been shown to improve the ability of Landsat-based vegetation-change detection algorithms, with F_{SCA} being used to improve a non-forest mask area, and differentiate deciduous from coniferous stands [*Stueve et al.*, 2011]. Other work shows that for estimating forest structure with remote sensing, winter imagery outperforms summer, for attributes including basal area and biomass volume [*Franco-Lopez et al.*, 2001].

It has been established that forest extent and changes can be observed using wintertime remote sensing, often improving upon summer-imagery approaches. Our research builds upon this existing work.

3 METHODS

This section is split into 2 parts: one dealing with development of a remote sensing technique to measure canopy extent using MODSCAG, and the second detailing field methods used to determine canopy extent and constrain remote sensing estimates of canopy change due to beetle-induced mortality in lodgepole pine forests.

Our research uses remote sensing data from 2000 to 2012, in order to identify beetle kill, quantify annual canopy extents, and document changes associated with beetle-induced mortality. Data on canopy extent in years before and after peak mortality can then be used to quantify canopy change caused by a known severity of beetle kill.

In this research, we measure canopy extent (F_c) indirectly, by characterizing the viewable gap fraction (VGF): the portion of the ground in forested areas that is visible from directly above; in satellite measurements, this is ideally observed at nadir. When ground is completely snow-covered and the canopy snow-free, at nadir, the VGF equals the maximum viewable snow fraction [*Liu et al.*, 2008; *Xin et al.*, 2012]:

$$Max.Viewable\ F_{SCA} = VGF_{nadir} = 1 - F_{c_{nadir}} \quad (5)$$

When the ground is only partially snow-covered (e.g. exposed rock and/ or soil), the equation takes the form:

$$Max.Viewable\ F_{SCA} + F_{Rock} = VGF_{nadir} = 1 - F_{c_{nadir}} \quad (6)$$

As MODSCAG is designed to maximize accuracy of F_{SCA}, and validation efforts have been focused in this area, this research measures VGF using F_{SCA} and F_{Rock}, rather than measuring F_c directly. As needles fall from trees, following beetle-induced tree mortality, the VGF – portion of pixel covered in rock and snow – should increase correspondingly.

The key to measuring VGF with fractional cover of rock and snow lies in carefully selecting dates where the canopy is snow-free, but undergrowth is snow-covered. Choosing days to measure VGF where snow remains in the canopy would yield overestimates of VGF (counting snow-covered canopy as part of the VGF), while selecting dates where undergrowth is exposed, not snow-covered, would underestimate VGF (counting undergrowth as part of the canopy).

3.1 STUDY AREA SELECTION:

We selected twenty-five sites to test our ability to measure changes in canopy cover associated with forest mortality. Sites are located in north-central Colorado and southern Wyoming, within the extent of the MLMA validation dataset, as shown in Figure 6. Sites were required to be in the seasonal snow zone, and in high-mortality lodgepole pine forests.

We defined the seasonal snow zone using frequency of snow cover for the Upper Colorado River Basin (UCRB), an area encompassing our study area, ~500,000 km^2 in Wyoming, Colorado and New Mexico centered on latitude of 38.375° and longitude of -108.2°. For each year from 2000 through 2012, we identified the first day of MODSCAG F_{SCA} on or following April 1 where mean sensor zenith angle for the UCRB was under 30°, and cloud-cover and other quality issues masked under 10% of the image. Pixels with higher than 75% frequency (at least 10 of 12 years) of snow present were mapped as part of the seasonal snow zone. This only includes pixels with at least 15% snow covered area, the lower detection limit of MODSCAG, [*Painter et al.*, 2009]. Additionally, pixels were required to be over 2000 m in elevation, in order to ensure that cloud-masking or other remaining spectral unmixing issues did not erroneously map low-lying, generally warmer areas as a part of the seasonal snow zone. The seasonal snow zone is shown in blue in Figure 6. Sites were further limited to pixels in lodgepole forests using an AVHRR-derived 1km^2 dataset [*Zhu and Evans*, 1994]. In lodgepole forests, red-stage

mortality is most prominent and long-lasting, increasing confidence in the MLMA validation dataset [*Meddens and Hicke*, 2014]. Spruce mortality has a spectral signature characterized by a short-lived yellow-green stage, quite unlike the red-stage mortality with which the MLMA dataset was developed [*Meddens and Hicke*, 2014; *Hart and Veblen*, 2015]. Spectral signature of drought mortality is also somewhat subdued, in comparison to bright red beetle-caused mortality [*Macomber and Woodcock*, 1994]. Locations within both the seasonal snow zone and lodgepole pine forests are shown in dark green in Figure 6.

Sites were then limited to high-mortality areas, defined as pixels with area composed of at least 75% dead trees. Within these constraints, 50 sites were then randomly selected using R's sampleRandom [*Hijmans*, 2014; *R Core Team*, 2014], and then manually screened for anthropogenic disturbances in Google Earth's Time Machine (e.g. salvage logging, road building, exurban development), leaving a final set of 25 sites, shown below as black triangles in Figure 6. Sites had a mean cumulative mortality of 80 ha/km^2, ranging from 75.2 to 91. Year of peak mortality ranged from 2005 to 2009, with an average timing of 2007 across all sites. Mean percent canopy cover as estimated by NLCD was 78% in 2001 and 47% in 2011, though direct comparison of multiple years of NLCD can be problematic, due to a change in methodology between production the two datasets [*Homer et al.*, 2012]. Elevations range from 2642 to 3214 m, with a mean of 2934; this includes sites spanning the elevation range of lodgepole pine distribution in Colorado, which is generally considered to be from 2500 to 3300 m in elevation [*CSFS*, 2007]. Details on each site are given in Table 3.

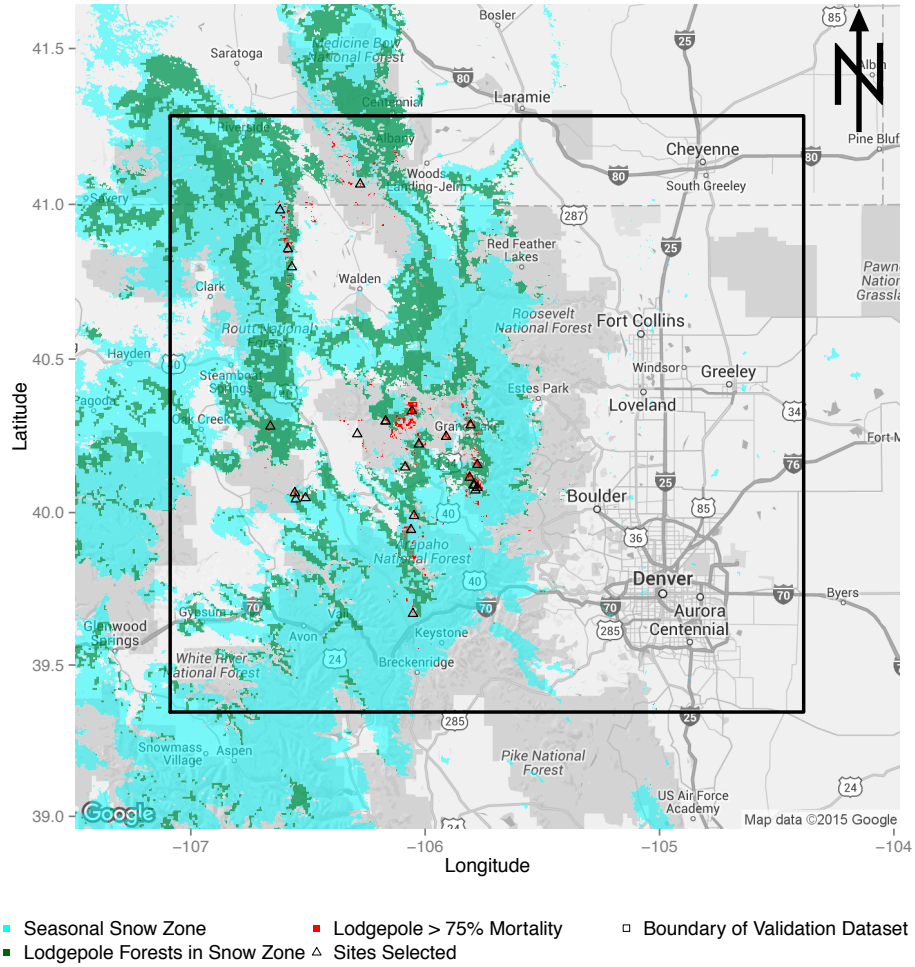

Figure 6: Remote-sensing study sites in north-central Colorado, USA, shown as black triangles. The seasonal snow zone is shown in blue, lodgepole pine forests within the seasonal snow zone are shown in green, and high-mortality (> 75% pixel area) lodgepole pine forests within the seasonal snow zone are shown in red. Study sites were randomly selected from these high-mortality areas, and then visually checked using Google Earth Time Machine to ensure a lack of anthropogenic disturbance.

Table 3: Study area overview for the 25 high-mortality lodgepole pine pixels selected for development of the remote sensing methodology

Location	Latitude	Longitude	Cumulative MLMA	Yr. Max. Mortality	SNOTEL Site	NLCD 2001	NLCD 2011	Elevation (m)	DC	1/DC	VGF Live	VGF Dead
Site 1	40.2854	-105.8063	82	2007	05J12S	74	29	2999	0.29	3.5	29	52
Site 2	40.2479	-105.9104	88	2007	05J12S	69	29	3108	0.19	5.3	32	58
Site 3	40.2229	-106.0271	77	2007	05J12S	68	40	3014	0.45	2.2	28	59
Site 4	40.1479	-106.0854	79	2007	05J12S	69	23	2921	0.22	4.6	25	66
Site 5	40.0813	-105.7771	82	2008	05K06S	67	20	3009	0.25	4.0	34	56
Site 6	40.1146	-105.8104	91	2006	05K06S	72	30	2920	0.42	2.4	26	53
Site 7	40.0896	-105.7896	83	2007	05K06S	72	35	2921	0.48	2.1	28	48
Site 8	40.0896	-105.7938	83	2007	05K06S	70	27	2874	0.35	2.9	28	47
Site 9	40.1563	-105.7771	78	2006	05K06S	67	29	3042	0.41	2.5	27	52
Site 10	40.0729	-105.7854	86	2008	05K06S	70	28	2942	0.25	4.0	29	46
Site 11	39.9896	-106.0479	75	2006	05K30S	76	35	2902	0.50	2.0	22	56
Site 12	41.0646	-106.2771	79	2007	06H24S	66	30	2647	0.28	3.5	27	45
Site 13	40.9813	-106.6188	81	2007	06H26S	76	32	2719	0.20	5.0	17	37
Site 14	40.3313	-106.0563	76	2008	06J05S	65	25	2826	0.38	2.6	30	62
Site 15	40.2979	-106.1688	77	2006	06J05S	71	31	3022	0.16	6.1	25	61
Site 16	40.0646	-106.5563	75	2008	06J06S	74	47	3077	0.37	2.7	26	52
Site 17	40.0479	-106.5104	77	2007	06J06S	74	24	2986	0.48	2.1	26	58
Site 18	40.0438	-106.5521	80	2006	06J06S	76	26	2957	0.39	2.5	29	49
Site 19	40.2563	-106.2896	78	2007	06J08S	74	0	3036	0.41	2.5	21	60
Site 20	40.2813	-106.6604	76	2009	06J09S	72	34	2916	0.52	1.9	32	48
Site 21	40.8563	-106.5854	81	2008	06J19S	76	0	2762	0.28	3.6	31	62
Site 22	40.7979	-106.5688	83	2007	06J19S	78	33	2643	0.30	3.3	46	60
Site 23	39.9438	-106.0604	79	2005	06K12S	78	0	2879	0.24	4.2	23	52
Site 24	40.2979	-106.1688	77	2006	06J05S	71	31	3022	0.23	4.4	25	61
Site 25	39.6688	-106.0521	80	2008	06K14S	77	37	3214	0.32	3.1	24	55

PROCESSING OF REMOTELY SENSED DATA

3.1.1 MEASURING THE VIEWABLE GAP FRACTION

This section details development of several methods for determining VGF, and by extension F_c, using the full suite of MODSCAG products. Comparison of methods tested, and final methodology selected are shown in the Results section.

The following preprocessing steps are used for all methods:

MODSCAG tiles of fractional snow, rock, and vegetation for the western United States were downloaded from NASA's Jet Propulsion Laboratory at http://snow.jpl.nasa.gov. Rasters were mosaicked and reprojected to NAD83. The native resolution is 500 m, which is the scale of this analysis.

High-quality Landsat-derived mortality area data (MLMA) was acquired from its creators [*Meddens and Hicke*, 2014], and reprojected to NAD83. Mean-based aggregation was used to increase pixel size from native 30 m resolution to 480 m. Rasters were then resampled to match MODIS grid coordinates with nearest-neighbor aggregation, using R's raster package [R Development Core Team, 2014].

After initial raster pre-processing, analysis splits into several branches. A suite of approaches were tested to quantify VGF; these are detailed below. Briefly, with a snowfall event, snow covers the forest canopy, increasing F_{SCA}. When snow melts from the canopy, this should decrease snow cover visible from above, causing F_{SCA} to decrease. During the winter months, dips or local minima (LMs) in a timeseries of F_{SCA} or $F_{SCA} + F_{Rock}$ are assumed to represent snow unloading from the canopy. A select set of these LMs represent our target conditions for measuring VGF: snow-free canopy, with a snow-covered understory. Thus, F_{SCA} on these days is equivalent to VGF, and can be used to measure VGF for a given year.

The performance of a suite of approaches for measuring VGF in this manner, by picking specific dates where F_{SCA} or $F_{SCA} + F_{Rock}$ are representative of VFG, are tested by their correlation with mortality area (MLMA) – as mortality area expands, we would expect VGF to increase accordingly. Thus, the best approach for quantifying VGF is chosen as that which shows the best correlation with MLMA (the mortality area estimate with highest resolution and geolocation certainty). This analysis is shown in the Results section.

Figure 7 illustrates an example of this methodology for determining VGF for two years, one before and one after severe beetle-induced mortality, in a single 500 m resolution pixel near Granby, Colorado. This example uses a spline-interpolated timeseries of summed F_{SCA} and F_{Rock} to measure the VGF. We show two years of MODSCAG fractional landcover data, along with an associated timeseries of snow water equivalent (SWE) data from a nearby and similar elevation snow telemetry (SNOTEL) site. SWE is simply the amount of water in the snowpack, and can be though of as the depth of water that would result if the entire snowpack were melted instantaneously. Vertical dashed lines show the time period that is considered the snow-covered season (December 1st through May 15th). Comparing spikes in the $F_{SCA} + F_{Rock}$ timeseries with the timeseries of SWE shows that in general, spikes closely follow increases in SWE, meaning that they are likely capturing snow interception by the canopy. This supports the idea that LMs in the timeseries represent unloading events, where the canopy is snow-free. All LMs in the timeseries during the snow-covered season are marked with points. Outliers, which do not represent target snow-free canopy and snow-covered undergrowth conditions, are marked in green, while points used to measure VGF are marked in purple; further details on distinguishing outliers are discussed below. Points selected as representative of that year's VGF are plotted in

purple, and their mean is the estimated VGF for that year, plotted as a bold, black horizontal dashed line.

In the two years shown, we estimate that in 2001 (before significant beetle kill has occurred), the pixel has a VGF of 31.2, and in 2010, the same pixel has a VGF of 50.6%. The VGF here is shown as a percent rather than fraction; the VGF is percent of pixel composed of ground. This indicates the fraction of ground visible over that 7 year period increased by 19% of pixel area: a 62% increase in VGF from initial conditions for this specific pixel. SWE accumulation patterns in the two years appear quite similar, supporting the idea that changes in viewable snow cover are due to landcover change, rather than differences in the annual snow regime.

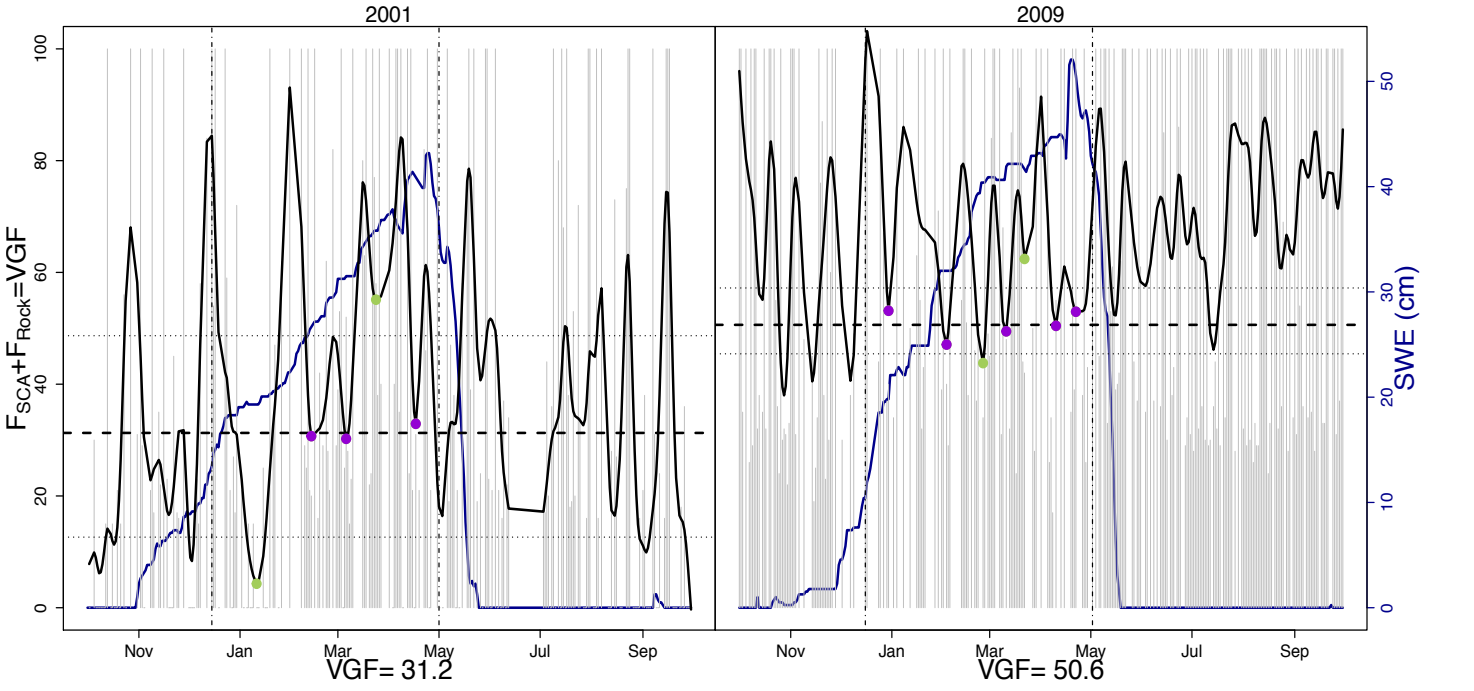

Figure 7: Timeseries of fractional land cover products (FSCA + FRock) near Granby, CO in 2001 and 2009, before and after peak beetle-induced mortality. Raw MODSCAG values are shown in light grey. A spline-interpolation is given as a solid black line Vertical dashed lines delineate winter season when undergrowth is assumed to be snow-covered. Points show local minima (LMs) in the timeseries, within the wintertime window. Bold dashed horizontal line shows measurement of VGF for that year. Light dashed horizontal lines delineate LMs used to calculate VGF from those deemed unrepresentative.

MODSCAG Approaches

While it may seem straightforward to estimate the VGF from F_{SCA} and F_{Rock}, there are several potential ways to approach the task. We test results of three main choices for quantifying yearly VGF, as enumerated below:

1) Endmember Selection

The fraction of land surface – all land cover with the exception of the forest canopy – viewable from directly above composes the viewable gap fraction. MODSCAG returns three endmembers: snow, rock, and vegetation. We test using only snow (F_{SCA}) to measure VGF, versus using snow and rock ($F_{SCA} + F_{Rock}$). Using the two endmembers makes the most physical sense, as exposed rock or soil may be present within the VGF, but may cause jumps in the timeseries, depending on sensor viewing geometry. Both are tested:

$$VGF = F_{SCA} \tag{7}$$

$$VGF = F_{SCA} + F_{Rock} \tag{8}$$

This creates the first branching of our methods tested, with two approaches.

2) Raw versus Spline Interpolated Timeseries

Most work utilizing the remote sensing of snow requires daily data, and thus employs a space-time smoothing algorithm to account for missing data related to cloud-cover obscuring the land surface or sensor noise and errors. One common approach in snow hydrology is to use a spline interpolation, as described in the Background section, developed by Dozier et. al [2008]. Measuring canopy, however, doesn't necessarily require daily data; a few good measurements every year can suffice, if the goal is to quantify canopy extent on a yearly basis, capturing slow changes occurring over the scale of months to years. Rather than a large number of days used to

quantify canopy, it is important that the days selected satisfy the necessary assumptions for measuring canopy cover: a snow-free canopy, and snow-covered undergrowth.

We test both raw and spline-interpolated timeseries of F_{SCA} and $F_{SCA} + F_{Rock}$ to quantify canopy cover. For raw timeseries, we only use data acquired at sensor zenith angles < 30°. This cutoff is used, following recommendations of Liu [2008] and Raleigh [2013], as over 30°, the observable fractional snow cover is under half the true value [*Liu et al.*, 2008]. A spline is more commonly used (e.g. [*Nolin*, 2010; *Rittger et al.*, 2013; *Micheletty et al.*, 2014]) , and is applied on both timeseries of F_{SCA} and $F_{SCA} + F_{Rock}$.

This is the second branching of our methods tested, yielding a suite of four possible approaches to estimate VGF; i.e. using raw versus spline interpolated data and using the single endmember approach, F_{SCA} , versus a two-endmember approach, $F_{SCA} + F_{Rock}$.

3) Outlier Elimination

Outlier estimates for VGF can occur when our target conditions – snow free canopy and snow-covered undergrowth – are not met. High estimates of VGF may occur when, following a large storm, a small snow melt event occurs (giving a LM in the timeseries) but residual snow remains in the canopy by the time of the next storm; if used to measure annual VGF, the incomplete-melt LM would give an anomalously high VGF value. In Figure 7, this occurs in March of both years, and is plotted as a green point. Outliers can also occur on the low side if F_{SCA} falls to zero or near-zero – this may be due to higher sensor zenith angle, or simply remaining issues in the MOD09GA retrieval or MODSCAG algorithms. An example of an anomalously low LM occurs in January of 2001. To reduce errors of both types, we include LMs that are only within a specified value from the mean of all local minima in a year, estimating annual VGF. We test a range of tolerances, from 0.5 to 2 standard deviations (sd) of all identified

LMs at an interval of 0.25 sd; the median of all LMs is also tested, for a total of 8 cutoff values. In Figure 7, the outlier cutoff value is shown for 1sd, with the horizontal, lightly dashed lines, delineating outlier LMs from those used to calculate VGF.

This is the third branching of our methods tested, with eight approaches, yielding a suite of thirty-two possible methods to estimate a yearly VGF, given a timeseries of winter MODSCAG; i.e. 2 options: raw versus spline-interpolated, 2 options: single versus two endmembers; 8 options of outlier removal

We also investigate effectiveness of these methods at multiple scales – single pixel analysis at MODIS native 500 m, and a 9-pixel grid at 1.5 km resolution surrounding a location of interest, to account for possible pixel misregistration errors, following Raleigh (2013) and Tan (2006).

Once a location and timeseries of MODSCAG is chosen, each year of data is analyzed separately, to give a timeseries of VGF at that pixel. Snow-covered season – where undergrowth is assumed to be snow-covered – is defined statically as December 1st through May 15th. Other methods of determining snow-covered season are certainly possible and warranted, but are beyond the scope of current analysis. A flowchart of these processing methods is given for reference in Figure 8.

The performance of these varied approaches for measuring VGF were tested by their correlation with mortality area (MLMA) – as mortality area expands, we would expect VGF to increase accordingly. Thus, the best approach for quantifying VGF is chosen as that which shows the best correlation with MLMA. Details of this analysis are shown in the Results section.

3.1.2 MEASURING CANOPY CHANGE

Changes in canopy extent due to tree mortality should correspond closely with the area of canopy killed, giving rise to that change. In using the MLMA to quantify beetle-induced

mortality this is explicitly clear: the MLMA gives percent of the pixel composed of dead trees, which is equivalent to the canopy area over which we expect to see change. A single tree dying will not influence the VGF in a 500m pixel substantially; all trees dying should. Mortality area does not correspond with an increased VGF in a one-to-one relationship, however. Even in a pixel that has experienced complete mortality, where all trees within the pixel are dead and grey-stage, trunks, branches, and some small twigs will remain, obscuring the satellite ground view. Thus, in order to see a 1% change in VGF, we would expect to need an increase in mortality area of over 1%. Using VGF data from periods before and after beetle-induced mortality, we quantify this relationship. We define the change in VGF per change in mortality area, and term it the defoliation coefficient (DC):

$$\mathrm{DC} = \Delta\text{Viewable Gap Fraction}/\Delta\ \text{Mortality} \tag{9}$$

To determine how VGF changes with beetle-induced mortality, we classify annual VGF measurements into two stages: live and dead. The two periods are delineated by determining the peak year of beetle-induced mortality – the year with the most area classified as red-stage in that pixel's MLMA dataset – and applying a one-year buffer on either side. Years before are classified as live, and years after are classified as dead. This timing is variable, depending on the progression of beetle-induced mortality at a given site. This process is shown in Figure 12, and described in further detail in the results section. Using a buffer lessens the potential effects of poorly identified mortality timing, and also allows for us to make an estimate of DC using the limited years of VGF we've measured. Ideally, a larger buffer could be used, allowing more time for needlefall, and higher certainty that some needlefall has occurred in later years of the pre-mortality VGF. However, with the limited dataset available to us, from 2001 to 2012, using a one-year buffer allows for multiple estimates of VGF in each class, reducing the effects of

interannual variability on our estimate of VGF change. Pre- and post-mortality VGF are calculated as the mean VGF in each time period, and their difference gives the change: ΔVGF. Change in mortality is calculated as the difference between minimum cumulative mortality, experienced in 2001, to maximum cumulative mortality, experienced in 2012; this is ΔMortality. The DC is then calculated from these two quantities at each individual site.

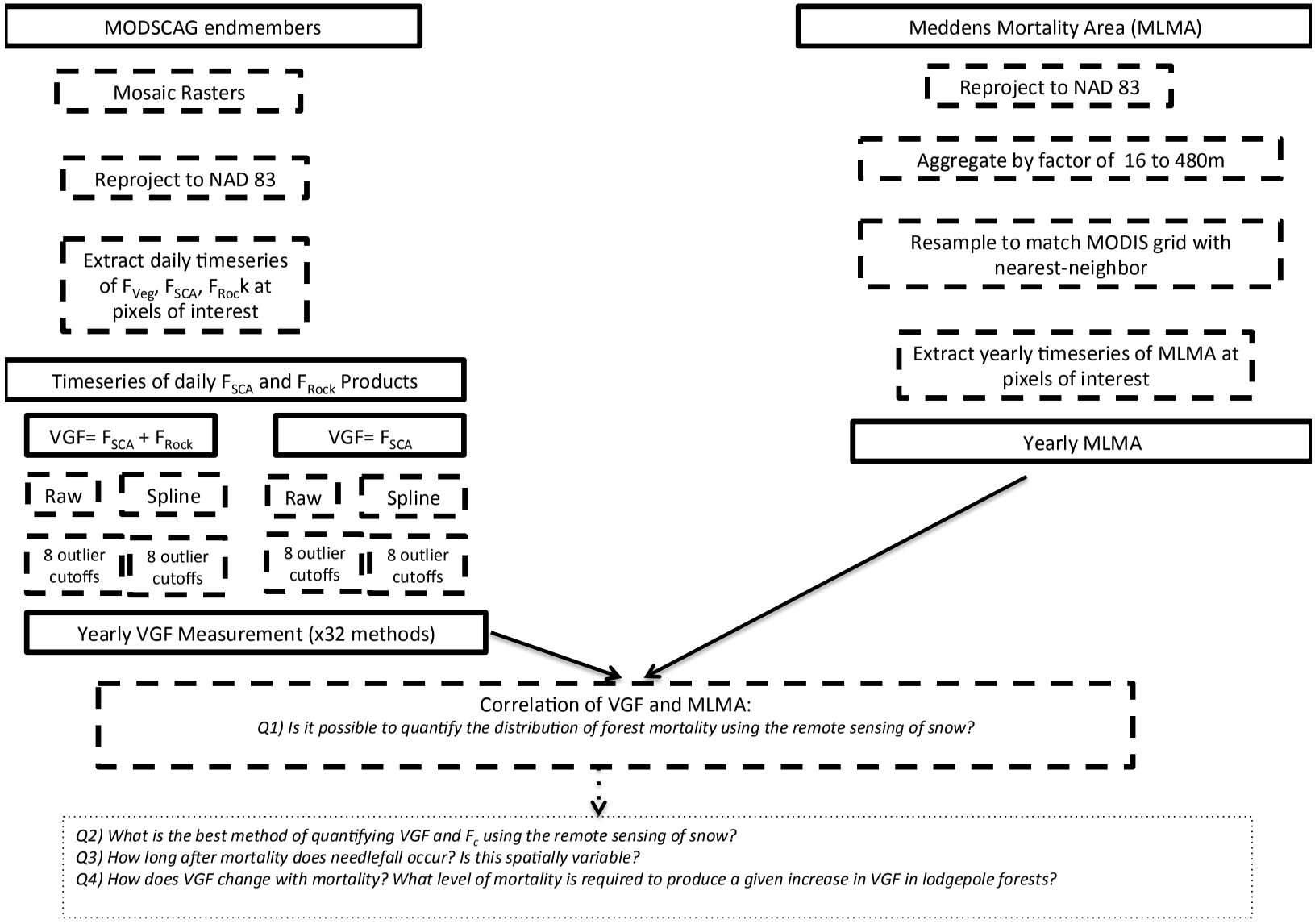

Figure 8: Data processing flowchart, showing how raw inputs are manipulated to answer research questions. Datasets are shown with a solid box, processes are shown with a dashed box, and research questions are shown with a fine dashed box.

3.2 FIELD METHODS: HEMISPHERICAL PHOTOGRAPHY

Hemispherical photography is commonly used to quantify forest canopy [e.g. *Liu et al.*, 2008; *Musselman et al.*, 2012; *Pugh and Small*, 2013]. Hemispherical photography grounds our remote sensing based estimate of canopy change using a space for time substitution model. In areas with extensive beetle kill, previous ground-based studies assume that canopy changes are due to beetle infestation; this research will do the same [e.g. Winkler et al., 2006; Biederman et al., 2012; Pugh and Small, 2012]. The space for time substitution allows us to quantify changes in canopy though the course of mortality, using a single year of field data [*Pickett*, 1989]. Such an approach is necessary given that this research did not begin prior to mortality and hence photos preceding mortality are not possible. In our space-for-time substitution, live, green trees from one location are compared with dead, grey-stage trees at another location as a substitution for the passing of time. Underlying this model is the assumption that the differences in canopy cover seen between the two sets of forest stands – live and dead – represent what would occur over time during disturbance of a single stand. This is not necessarily true, as field studies have established that beetles preferentially attack large-diameter trees, and leave small-diameter untouched [*Safranyik and Wilson*, 2006]. However, this study made an effort to select stands with similarly sized trunks and stand densities in both mortality classes; using a t-test, there is no significant difference in basal area between live and dead classes ($p > 0.05$). This was made possible by using the continental divide as a barrier, as the beetle outbreak has largely left the Colorado Front Range relatively unscathed. In areas to the west of the continental divide, few large-diameter lodgepole trees remain unimpacted. East of the continental divide, however, it's possible to find live stands of mature lodgepole pine with trunk diameters similar to those that

have died in the rest of the state. Pine beetle preferentially attack large diameter trees, especially those over 25 cm in diameter at breast height (DBH) [*Safranyik et al.*, 1974].

In hemispherical photography, an upward-looking photograph with a fish-eye lens is taken on a level plane, ideally on a cloudy day or at dusk. Photographs are then converted to binary black and white, based upon pixel brightnesses, pixels are weighted given angular location and effective size, and percentage of viewable sky is calculated to measure the VGF.

Upward-looking hemispherical photographs were captured at 46 sites in live and dead lodgepole stands across northern Colorado, primarily near Frasier, CO and Nederland, CO, using a Nikon D700 digital single lens reflex camera [Nikon Corporation, Japan], with a Sigma 8 mm F3.5 EX DG Circular Fisheye Lens [Sigma Corporation, Japan]. Field sites were selected to be as close to 100% live or 100% dead trees as possible, to represent stages completely before and after beetle kill. Broad-scale areas were chosen based on knowledge of intense beetle kill, or lack

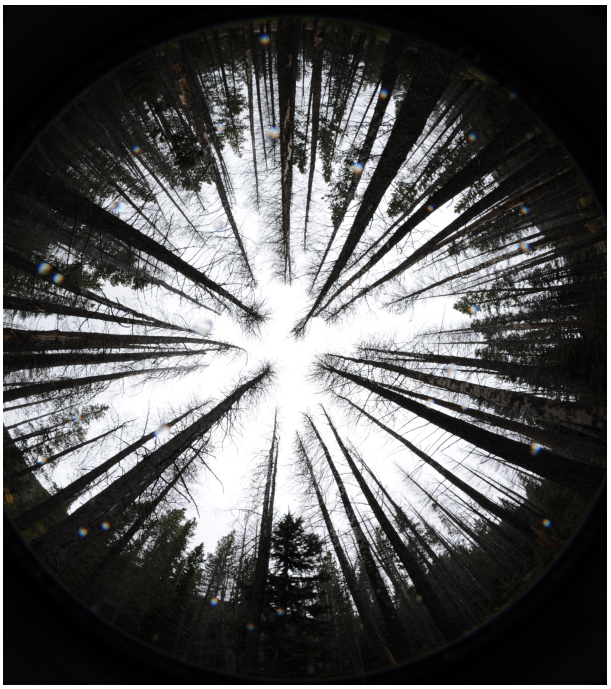

Grey Stage Lodgepole Plot

Green Lodgepole Plot

Figure 9: Hemispherical photography showing a live, green, lodgepole forest stand, and a dead, grey-stage mortality stand.

thereof, in a particular location. Once in such an area, photograph locations were chosen based on observed tree mortality (as close as possible to 100% either live or dead), and proximity to roads for access convenience. Sites were separated from one another by a minimum of 30 m, to prevent overlap of canopy measurements. Selected sites are shown in Figure 10, and additional site characteristics are given in Table 4.

At each location chosen, 3 pre-set exposures were captured at ~1.4 m from ground height using a tripod. A bubble level fitted to the lens cap was used to level camera, and a hand-held compass was used to orient the top of the image to geographic north. Additionally, size classes of trees were visually estimated within a ~15 m radius from the photo location. The diameter at breast height (DBH; 1.4 m from the ground) was measured for 5 trees in estimated small, medium, and large size classes, for a total of 15 DBH measurements per site. Canopy height was also measured for 5 representative trees at each plot using a TruePulse 360B laser rangefinder, which has a reported accuracy of 0.3 m [*Laser Technology Corporation, 2015*].

For each site, the exposure with the most contrast between sky and canopy was chosen for analysis. The selected images were processed in Gap Light Analyzer (GLA) Version 2.0 software [*Frazer et al.*, *1999*], following procedures of Frazer [1999] and Hardy et al. [2004]. The VGF is determined as the fraction of unobstructed sky present in the picture, using a thresholding procedure based upon pixel brightness; pixels are sine-weighted to adjust for variable effective area in hemispherical photograph. Thresholding is a subjective process, with few opportunities for systemization. Nonetheless, many other studies have found consistent results under a variety of light and weather conditions [e.g. *Liu et al.*, 2008; *Burles and Boon*, 2011; *Musselman et al.*, 2012; *Perrot et al.*, 2012; *Gleason et al.*, 2013]. In this work, thresholding was performed by two skilled practitioners, and the average of both analyses was

used. The mean VGF for all sites for the two practitioners were separated by only 5%, but were significantly different ($p < 0.05$).

A map with hemispherical photo locations, and table of overall site characteristics are given in Table 4 and Figure 10.

Figure 10: Locations of hemispherical photos taken in live and dead forest stands. Red triangles indicate dead stands, and dark green represent live.

Change in VGF, the numerator of the DC_{Field}, is calculated as the difference of mean VGF in live sites from the mean VGF in dead (ΔVGF_{Field}). This field estimate of VGF change (ΔVGF_{Field}) is analogous to the remote sensing estimate (ΔVGF_{RS}) without any adjustments, as given below:

$$\Delta VGF_{Field} = \overline{VGF}_{Dead} - \overline{VGF}_{Live} \quad (10)$$

Calculating the change in mortality area is more complicated. In order to serve as a comparison for our remotely sensed estimate of the DC, it's necessary to create an analogous denominator for change in morality area. The MLMA is the percent of a pixel composed of dead trees, with units of ha/km^2. Thus, to calculate an analogous value, we must calculate a change in tree mortality area per unit ground area covered in each hemispherical photograph. This is especially important as most plots contained a mixture of dead and live trees; we must be able to capture the mortality area present in all plots in order to comment on the change, using these somewhat mixed stands. This can be described as:

$$\Delta Mortality_{Field} = \frac{\overline{Area}_{Dead\ (in\ dead\ plots)}}{Area_{Plot}} - \frac{\overline{Area}_{Dead\ (in\ live\ plots)}}{Area_{Plot}} \quad (11)$$

where mean basal area of dead trees across all dead plots is given as $\overline{Area}_{Dead\ (in\ dead\ plots)}$, mean basal area of dead trees across all live plots is given as $\overline{Area}_{Dead\ (in\ live\ plots)}$, and $Area_{Plot}$ is the planar area covered by the hemispherical photograph.

We calculate $Area_{Plot}$, using plot canopy height, and the knowledge that we calculate VGF using only canopy from 0-60° zenith angle. This site geometry is illustrated in Figure 11. Using basic trigonometry, knowledge of camera zenith angle (60°), camera height from ground (1.4 m), and tree height (H; variable), it follows that the plot radius and area can be described by:

$$\text{Radius}_{plot} = \text{Cos}(60°) \times (\text{H-1.4 m}) \quad (12)$$

$$Area_{plot} = \pi \times [\text{Cos}(60°) \times (\text{H-1.4 m})]^2 \quad (13)$$

$Area_{Plot}$ is the denominator of the $\Delta Mortality_{Field}$ terms.

Calculating basal area of dead trees in all plots is more complicated, as it was not measured directly in the field. It is necessary to calculate the basal area of dead trees in our live stands, as it was not possible to find completely green, live stands, and some dead canopy is often included in

site hemispherical photographs. Similarly, dead stands often had a small number of live trees in the hemispherical photograph. Explicitly calculating the basal area of dead trees at each plot allows us to control for the effects of these somewhat mixed-mortality classes. $\overline{Area}_{Dead}$ is the mean basal area of dead trees in all plots of either live or dead mortality stage, as denoted; this is calculated by determining the basal area of dead trees at each site: $Area_{Dead_{Site\,i}}$.

We calculate $Area_{Dead_{Site\,i}}$. using the number of both live and dead trees per image, in combination with field DBH data collected at each site. The number of live and dead trees at each site were recorded during image thresholding The proportion of dead trees present at each site is calculated with these manual counts as:

$$P_{Dead} = \frac{N_{Live}}{N_{Dead}} \tag{14}$$

Where N_{Live} is the number of live trees, N_{Dead} is number of dead trees, and P_{Dead} is the proportion

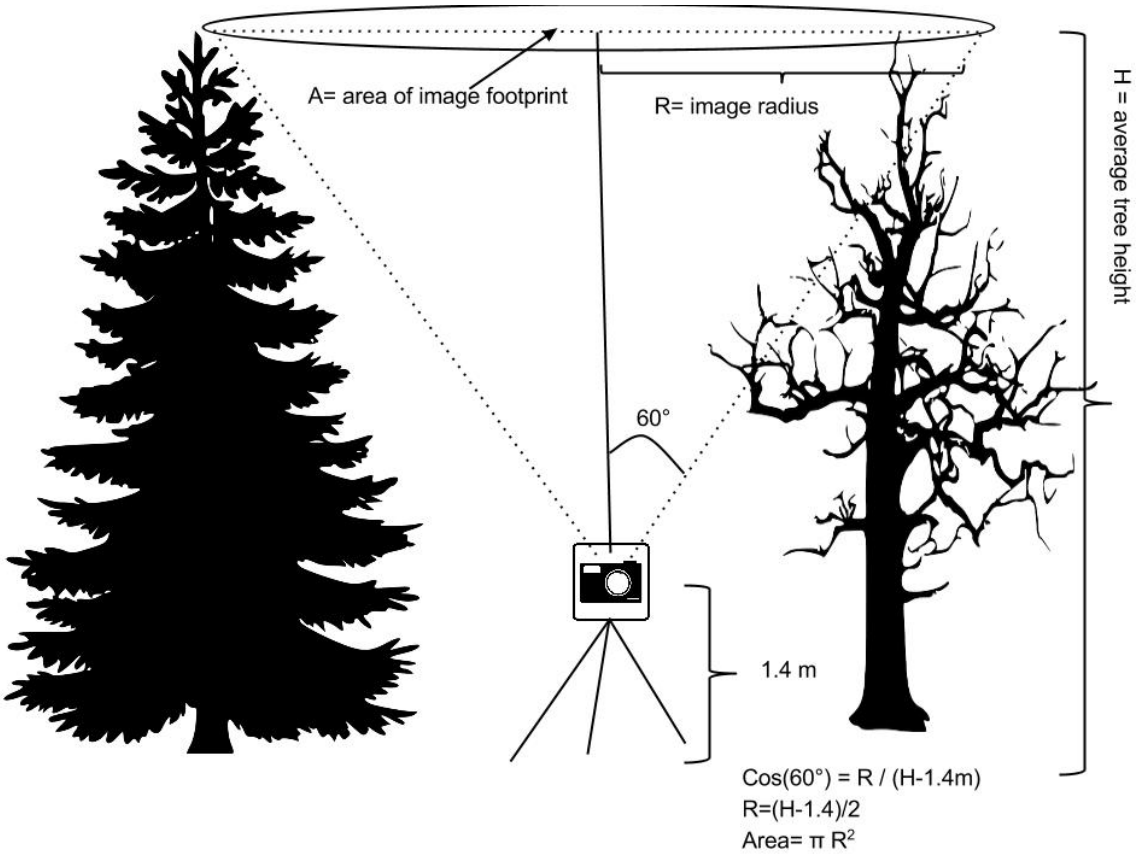

Figure 11: Schematic relating hemispherical photography to ground area captured by photograph, using average plot tree height (H), camera zenith angle used to measure VGF (60°), and camera height from ground (1.4m).

of dead trees. Total number of trees at each plot is denoted with N_{Total}.

At each site, size classes of trees within an approximate radius of 15 m from the photo location were visually estimated, and 5 from small, medium, and large classes were measured, giving a total of 15 DBH measurements per site. The mean of these for the 3 size classes is used, giving mean DBH for small, medium and large trees at each plot.

Next, we calculate total stand basal area for each site. We accomplish this by assuming that trees fall evenly into the 3 size classes, so that 1/3 of total tree count is given the DBH of that size class. This is expressed as:

$$TA_i = \frac{N_{Total_i}}{3} \times \pi \left(DBH_{Small_i}/2\right)^2 + \pi \left(DBH_{Medium_i}/2\right)^2 + \pi \left(DBH_{Large_i}/2\right)^2 \quad (15)$$

$$SBA_i = \frac{TA_i}{Area_{Plot}} \quad (16)$$

where TA_i is cross-sectional tree area in m^2, $\frac{N_{Total_i}}{3}$ is the number of stems in each size class, $\pi(DBH/2)^2$ is the basal area of a single tree of a specified DBH for the three size classes in meters, and SBA.

Next, we determine $Area_{Dead_{Site\,i}}$ with:

$$Area_{Dead_{Site\,i}} = SBA_i \times P_{Dead_i} \quad (17)$$

We can then calculate $Mortality_{Field}$ for both live and dead classes. We calculate tree basal area in square meters (m^2); in order to correspond with the MLMA, which is expressed ha dead trees/km^2, we convert stand basal area to ha of tree stem area, and divide by $Area_{plot}$, which is expressed in km^2.

From here, we calculate the $\Delta Mortality_{Field}$ as shown in Equation (11), and DC_{Field} as below:

$$DC_{Field} = \frac{\Delta VGF_{Field}}{\Delta Mortality_{Field}} \quad (18)$$

Table 4: Hemispherical photograph locations in Northern Colorado, with associated site characteristics including elevation, Meddens cumulative Landsat Mortality Area (MLMA), year of maximum mortality (as seen in the MLMA), and forest cover from the National Land Cover Dataset 2001 and 2011 [*Homer et al.*, 2004; *Meddens and Hicke*, 2014].

Location	Latitude	Longitude	Elevation (m)	Cumulative MLMA	Yr. Max. Mortality	NLCD 2001	NLCD 2011
Dead 1	39.7708	-105.81634	3031	18	2007	63	51
Dead 2	39.9321	-105.85068	2690	50	2010	67	37
Dead 3	39.93114	-105.85175	2690	50	2010	67	37
Dead 4	39.93069	-105.85218	2690	50	2010	67	37
Dead 5	39.93025	-105.852	2690	50	2010	67	37
Dead 6	39.93055	-105.85138	2690	50	2010	67	37
Dead 7	39.93171	-105.85118	2690	50	2010	67	37
Dead 8	39.93122	-105.85146	2690	50	2010	67	37
Dead 9	39.93049	-105.8507	2690	50	2010	67	37
Dead 10	39.91164	-105.87603	2757	41	2007	75	49
Dead 11	39.90709	-105.88409	2786	20	2007	68	48
Dead 12	39.90698	-105.88618	2786	20	2007	68	48
Dead 13	39.90698	-105.88618	2786	20	2007	68	48
Dead 14	39.90688	-105.88766	2802	20	2007	60	30
Dead 15	39.8758	-105.90118	2935	37	2007	74	49
Dead 16	39.87599	-105.90079	2935	37	2007	74	49
Dead 17	39.882835	-105.89397	2854	35	2007	69	35
Dead 18	39.88968	-105.8972	2908	26	2007	78	51
Dead 19	39.77038	-105.81578	3031	18	2007	63	51
Dead 20	39.77054	-105.8162	3031	18	2007	63	51
Dead 21	39.95358	-105.60445	2829	4	2010	77	64
Dead 22	39.95379	-105.60483	2829	4	2010	77	64
Live 1	39.95362	-105.60381	2781	4	2010	79	63
Live 2	39.933269	-105.57821	2925	6	2009	75	43
Live 3	39.933142	-105.57772	2925	6	2009	75	43
Live 4	39.933072	-105.57756	2925	6	2009	75	43
Live 5	39.938369	-105.56837	2833	2	2010	46	42
Live 6	39.95366	-105.60378	2781	4	2010	79	63
Live 7	39.95353	-105.60406	2781	4	2010	79	63
Live 8	39.95369	-105.60508	2829	4	2010	77	64
Live 9	39.95394	-105.60557	2829	4	2010	77	64
Live 10	39.97426	-105.5496	2760	2	2009	65	52
Live 11	39.97427	-105.54996	2760	2	2009	65	52
Live 12	40.0346	-105.5442	3028	2	2010	76	60
Live 13	40.035	-105.544	3028	2	2010	76	60
Live 14	40.0354	-105.5438	3028	2	2010	76	60
Live 15	40.0355	-105.5444	3028	2	2010	76	60
Live 16	40.03558	-105.54436	3028	2	2010	76	60
Live 17	40.03675	-105.54565	3028	2	2010	76	60
Live 18	40.03617	-105.54617	3067	2	2010	77	65
Live 19	40.036505	-105.54691	3067	2	2010	77	65
Live 20	40.03684	-105.54765	3067	2	2010	77	65
Live 21	40.03618	-105.54624	3067	2	2010	77	65
Live 22	40.03582	-105.54623	3067	2	2010	77	65
Live 23	40.03537	-105.54628	3067	2	2010	77	65
Live 24	40.03573	-105.54666	3067	2	2010	77	65
Live 25	40.03602	-105.54635	3067	2	2010	77	65

4 RESULTS

The basic objective of this research is to illustrate that MODIS-observed F_{SCA} data can be used to quantify the distribution of forest mortality and associated VGF increases, and develop a method to do so.

In order to evaluate our approach and to determine the best methodology, a comparison is made with the best available large-scale dataset on lodgepole pine mortality: the MLMA. However, there is an inherent temporal lag of several years between mortality (MLMA), and needlefall (when we expect our measurement of VGF to increase). The MLMA reports year of red-stage tree mortality, not year of needlefall; additionally, initial green-stage tree mortality is one year prior to year of MLMA reported mortality [*Meddens and Hicke*, 2014]. Timing of needlefall post-mortality is variable, and lags behind initial green-stage mortality by 3-5 years [*Wulder et al.*, 2006]. Lag-time reported hereafter gives a lag from green-stage mortality to observed increases in VGF.

In order to compare the two metrics of mortality quantitatively, we must first apply a temporal lag; time must be allowed for the needles to dry and fall from the trees, following initial green-stage mortality.

4.1 QUANTIFYING THE VIEWABLE GAP FRACTION WITH REMOTE SENSING OF F_{SCA}

Q1) Is it possible to quantify the distribution of forest mortality using the remote sensing of snow?

Our annual VGF estimates and the MLMA validation data both increase over the course of the 2000's era pine beetle epidemic, with mortality occurring a few years before an increase in VGF is observed. This relationship is easily visualized with a simple timeseries comparison. In Figure 12, timeseries of cumulative mortality area is shown in dark brown, our estimate of VGF is shown in red, and mortality area for each individual year is shown in orange for four sites across Northern Colorado, as listed in the upper left of each panel. This pattern is consistent across all sites, though only four are shown for brevity. Cumulative mortality area and VGF both begin low in the early 2000s, and finish high in the 2010s. Increases in mortality precede

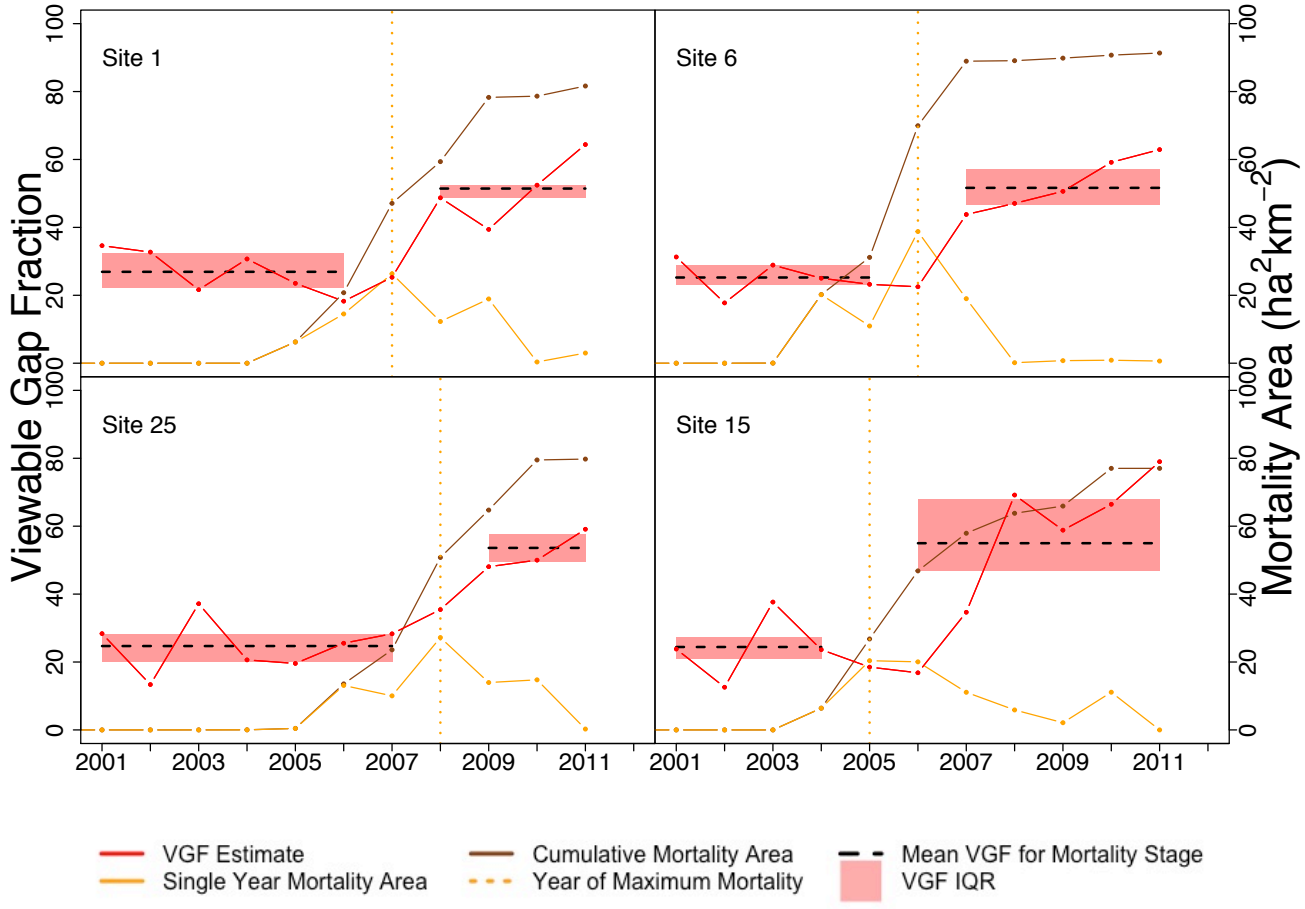

Figure 12: Timeseries of beetle-induced tree mortality and VGF at four sites. Cumulative mortality is shown in dark brown. Mortality occurring in a single year is shown in solid orange. Year of maximum single-year mortality is used to separate pre- and post- beetle stages; this is shown with a vertical, dashed orange line. VGF is shown in red. Red shading shows the inter-quartile range (IQR) of pre- and post-beetle VGF. Change in VGF through the beetle-kill epidemic is much larger than interannual variability in our VGF measurement

increases in VGF, as expected. In the figure, VGF is divided into two periods: before and after beetle kill, with either live or dead forests respectively. The two periods are delineated by determining the peak year of single-year beetle-induced mortality in that pixel's MLMA dataset (vertical orange dashed line), and applying a one-year buffer on either side. This timing is variable; maximum mortality for Site 25 occurs in 2008, while Site 15 is 3 years earlier in 2005. Trees die individually, not as a section of forest; the year of maximum mortality is simply the year when the most trees in a given pixel are in red-stage mortality. Red shading shows the inter-quartile range (IQR) of VGF in each period. Visually, it is apparent that year-to-year variability in our VGF estimate is much smaller than changes to the VGF caused by beetle-induced mortality, giving higher confidence that we do indeed capture the process of beetle-related mortality and defoliation. This is borne out statistically as well: distributions of VGF are significantly higher in years following beetle mortality at all 25 high-mortality sites investigated using a t-test ($p<0.05$), as illustrated with a boxplot in Figure 14.

In addition to showing significant change with beetle kill, the VGF is significantly correlated with MLMA. A Pearson's correlation is used to compare correlation across all sites and methods, even though in many cases the MLMA is not normally distributed. This would normally indicate that a non-parametric statistical test should be used. However, in this case, using a spearman's ranked correlation yields many lag times with a perfect correlation ($r=1$), with both timeseries increasing monotonically, which makes determining the lag-time for needlefall difficult. Thus, a Pearson's correlation is used, as it varies with increases in lag timing, and captures the changing relationship between VGF and Mortality with increased lag time numerically quite well.

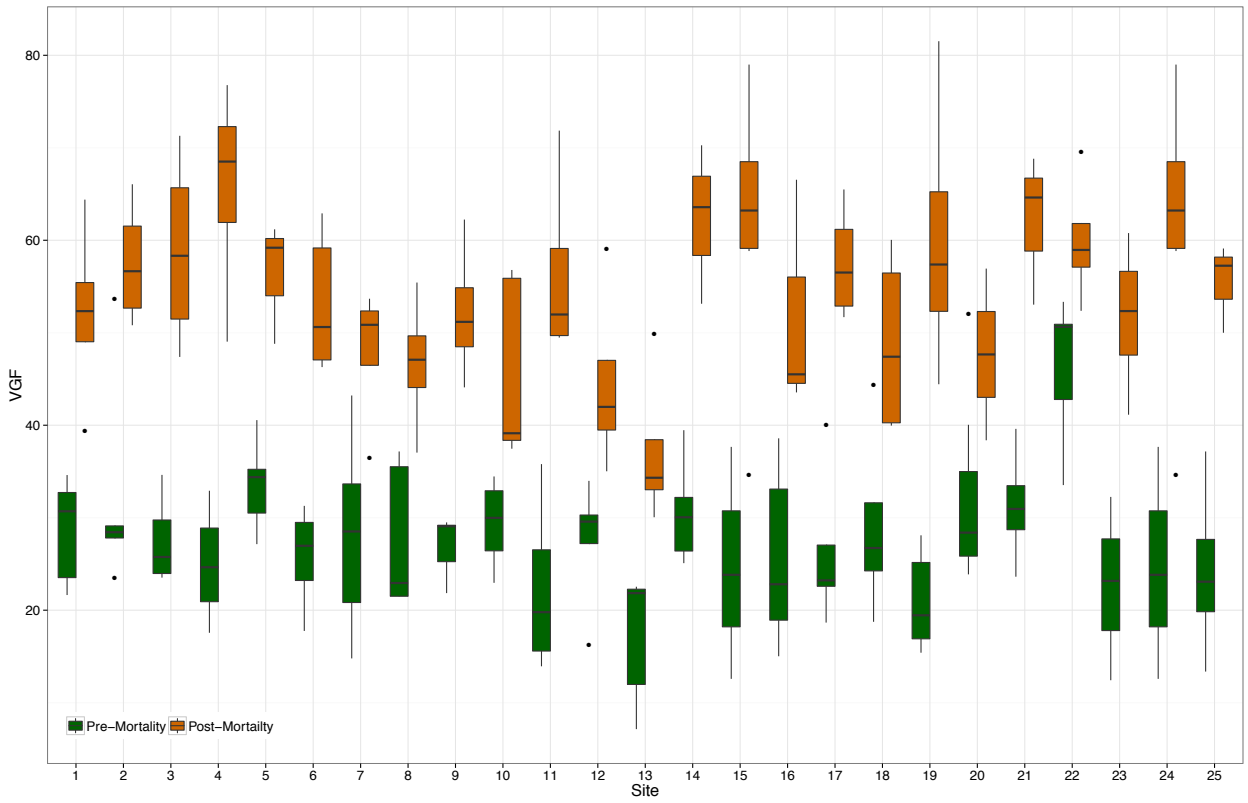

Figure 14: Boxplots displaying the range of VGF before and after beetle-induced tree mortality, for all 25 high-mortality remote sensing sites. Green represents live VGF, and orange represents grey-stage, dead VGF.

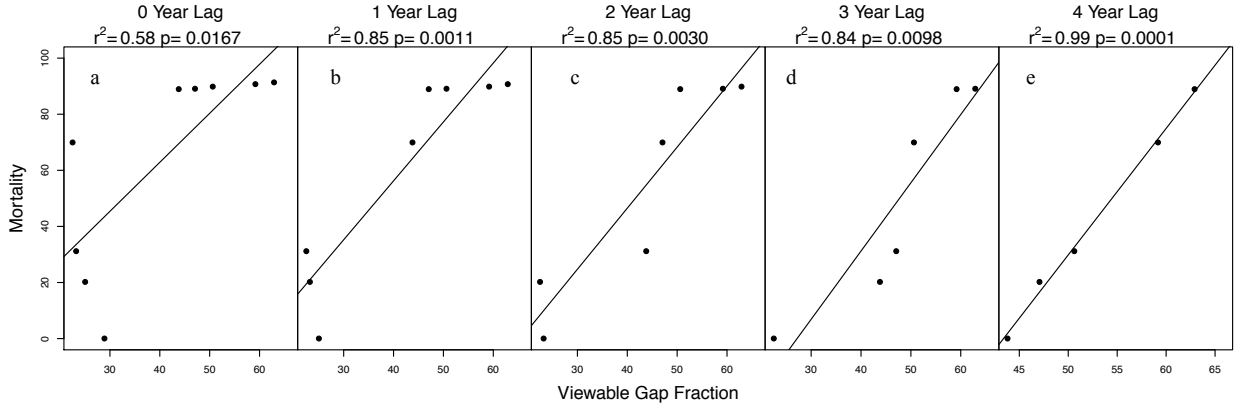

Figure 13: Correlation of mortality area (MLMA) and viewable gap fraction (VGF) for a single site. The left panel shows zero year lag time, with mortality that occurred in 2010 (red-stage detected in summer 2011) correlated with winter 2011 VGF. The second panel shows a 1-year lag, with mortality occurring in 2010 correlated with VGF in 2011. Remaining panels show increasing lag-timing to allow for needlefall. Pearson's correlation coefficients are shown. As lag time is increased, number of points in the correlation decrease.

Without applying any lag time to the correlation, the VGF is significantly correlated with the MLMA across all 25 high-mortality sites for all methods tested in 98% of cases, with a mean Pearson's r of 0.76 ± 0.11 (n=800; $p<0.1$); this includes both MODSCAG endmember combinations, raw and spline-interpolated timeseries, and all outlier-cutoff thresholds. However, as shown in Figure 12, it is apparent that VGF rises a few years following the increase in mortality; the relationship follows the physical processes we know occur on the ground: trees die, and then needles take time to dry, turn red, and fall from the branches, increasing the VGF several years after initial mortality. Thus, correlation coefficients generally increase if a temporally-lagged correlation is used, giving needles time to fall from the trees after detection of red-stage mortality. Data is first subset to years that both the VGF and MLMA are available: 2001 to 2011. Then, VGF is shifted from 0-4 years ahead of mortality. This allows us to correlate VGF of a given year with the cumulative mortality experienced at that site from 0-4 years prior. VGF Correlation of non-lagged data is shown in panel a of Figure 13, and lagged data with corresponding improvement in correlation coefficient are shown in remaining panels. For this example, Site 6 –near Granby, CO – lagging correlation by four years gives the highest r^2 value, as displayed in the rightmost panel. In this univariate regression, r^2 is simply the square of Pearson's correlation. Due to constraints on available years of data, we were only able to test lag timing of 0-4 years following green-stage mortality; each year of lagging necessitates losing a year of data of both mortality and VGF. Across all sites and methods at the single-pixel scale, using only the best lag-timing for all methods improves mean r^2 from 0.60 ± 0.13 (n=4000) to 0.88 ± 0.06 (only best lag time for that method and site, n=800). Using only our final, selected method, this improves to a mean r^2 of 0.92 ± 0.05 (n=25).

4.2 CHOOSING A METHOD

Q2) What is the best method of quantifying VGF and F_c using the remote sensing of snow?

Annual VGF Estimates

For any single location, 32 approaches were tested for quantifying VGF on an annual basis. Choices were made on MODSCAG endmembers to use (F_{SCA} vs. $F_{SCA} + F_{Rock}$), raw vs. spline-interpolated timeseries, and outlier tolerance, yielding 32 separate estimates of annual VGF, as described in detail in Section 3.2. These different approaches give slightly different estimates of VGF each year. Figure 16 shows the sensitivity of annual VGF measurements to the outlier removal method used. Points on the figure represent the estimated VGF using each method, and arrows correspond to one standard deviation in either direction, using the multiple dates of VGF measured each year. Approaches which remove most annual LMs from the VGF estimate have a smaller range of variability. For some years, using the smallest tolerance for outliers – 0.5 sd – yielded only one date which was used to estimate VGF. These years have no standard deviation of the dates used for a VGF estimate, and hence no confidence intervals plotted. Figure 15 is analogous, showing the sensitivity of VGF estimate to use of different MODSCAG endmembers and use of a raw or spline-interpolated timeseries.

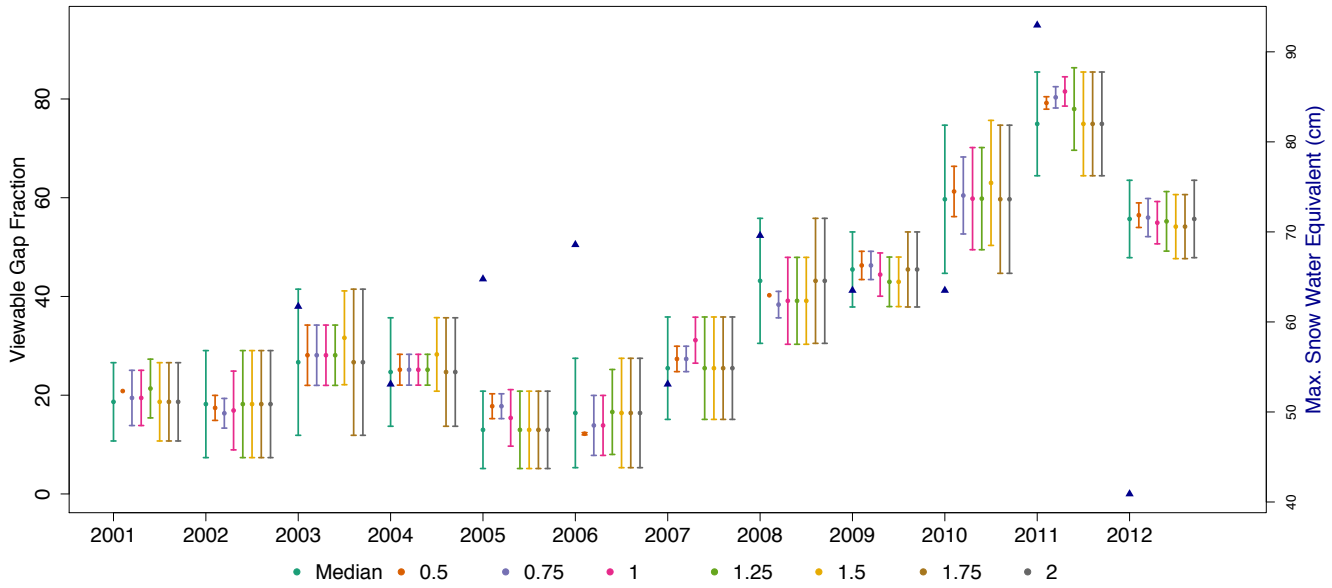

Figure 16: This boxplot displays the VGF measured at Site 19 every year, using different sd outlier cutoff thresholds. The point is the VGF estimate for that year. The line extends one standard deviation of all yearly LMs above and below that point, showing the range of variability for LMs that are used to measure the VGF. Plots for other sites show a similar pattern.

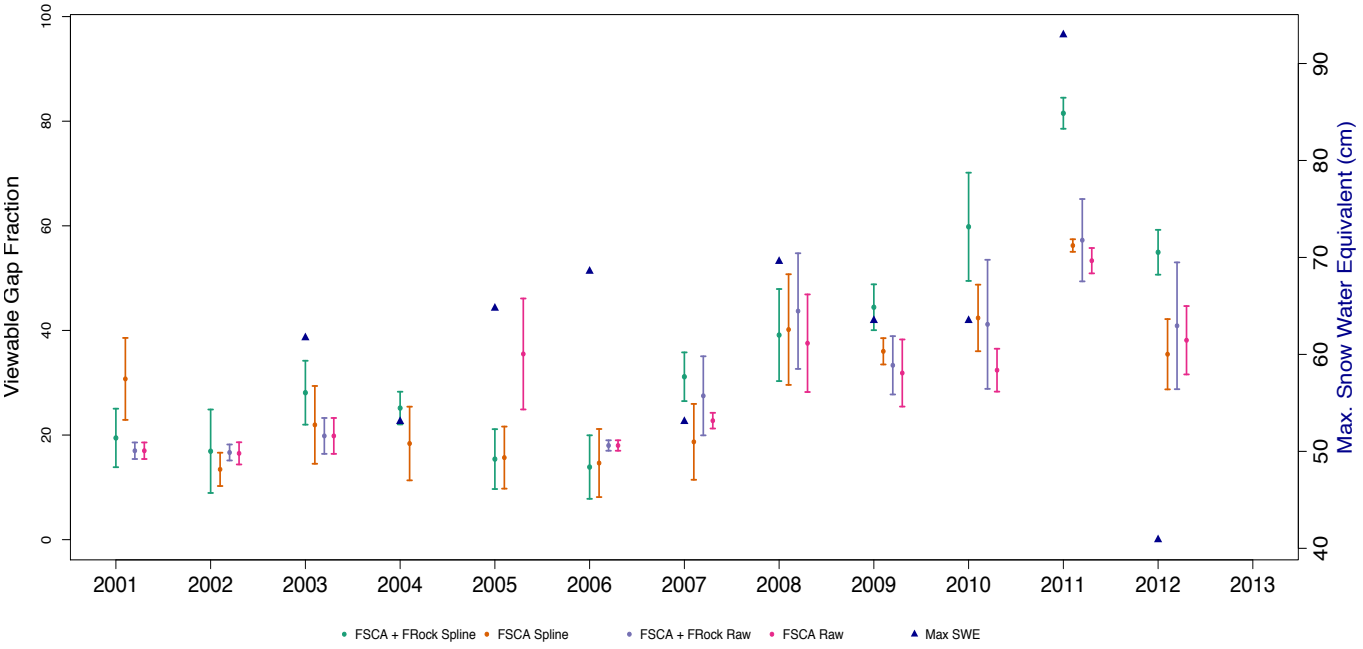

Figure 15: This boxplot displays the VGF measured at a single site every year, for changing MODSCAG endmembers and choice of raw vs. spline timeseries. The point is the VGF estimate for that year. The line extends one standard deviation of all yearly LMs above and below that point, showing the range of variability for LMs that are used to measure the VGF.

In both Figure 16 and Figure 15, overall patterns in VGF are the same: increasing VGF through time, with small differences between approaches on annual estimates of VGF. It appears that sensitivity of VGF estimates to these methodological choices is actually quite low, though for obvious reasons, using a combination of F_{SCA} and F_{rock} endmembers yields higher estimates of VGF than simply using F_{SCA} alone, as shown in Figure 15. The best method is selected as that which is most highly correlated with the MLMA. A consistent use of Pearson's correlation allows for both robust correlation coefficient estimates, and meaningful comparison across all sites and methods.

Correlations of VGF and MLMA are performed for data shifted 0-4 years after red-stage mortality for each of the 32 approaches, and the lag time with the best correlation coefficient (r) is chosen. Testing lag times from only 0-4 years following mortality was possible, due to constraints on the length of record of both datasets; a minimum of 3 values are required for correlation, and each additional year of lag causes the loss of an additional year of overlap. Additionally, years of MLMA used in the correlation are limited so that only a single pre-mortality year of <1 ha mortality area/ km^2 is used in the correlation. This prevents statistical leverage of many near-zero values from biasing the correlations; this issue is largest in areas with a later onset of mortality, and thus a longer record of near-zero mortality. Additionally, this process allows us to identify the lag time between mortality timing identified by the MLMA and needlefall, identified by an increase in VGF. All correlations shown hereafter use Pearson's correlation, and include only the best-lagged correlation from each site. This gives one value of r per site – selected as the highest – with lag-time from mortality to needlefall differing from site-to-site as it does in reality.

All further analyses are based upon this single best lag-timing correlation per site. This gives a total of 800 correlation coefficients: 25 sites, a choice of 2 MODSCAG endmember combinations (F_{SCA} vs. $F_{SCA} + F_{Rock}$), a choice of 2 ways to deal with missing values and non-ideal sensor viewing geometry (raw vs. spline timeseries), and eight tested outlier tolerances.

The method with the absolute highest *r* value varied from site to site; we pick the method with the most frequent occurrence of high *r* values. In Figure 17, a boxplot of correlation coefficients, limited to those which are significant with $p < 0.1$, shows that using $F_{SCA} + F_{Rock}$ and a spline yields the highest set of *r*-values at both the single-pixel and nine-pixel scales. Summary statistics across the 25 sites are given in Table 5; using $F_{SCA} + F_{Rock}$ and a spline gives the highest correlation mean coefficients at both the single pixel and nine-pixel scales

Table 5: Mean correlation coefficients for best lagged VGF-MLMA pairs across 25 high mortality sites, including all outlier elimination methods

	Single Pixel	Nine Pixel
FSCA + FRock Spline	0.92±0.07	0.93±0.06
FSCA Spline	0.90 ± 0.09	0.89±0.09
Raw FSCA	0.90 ± 0.08	0.91±0.06
Raw FSCA + FRock	0.89 ± 0.09	0.93±0.05

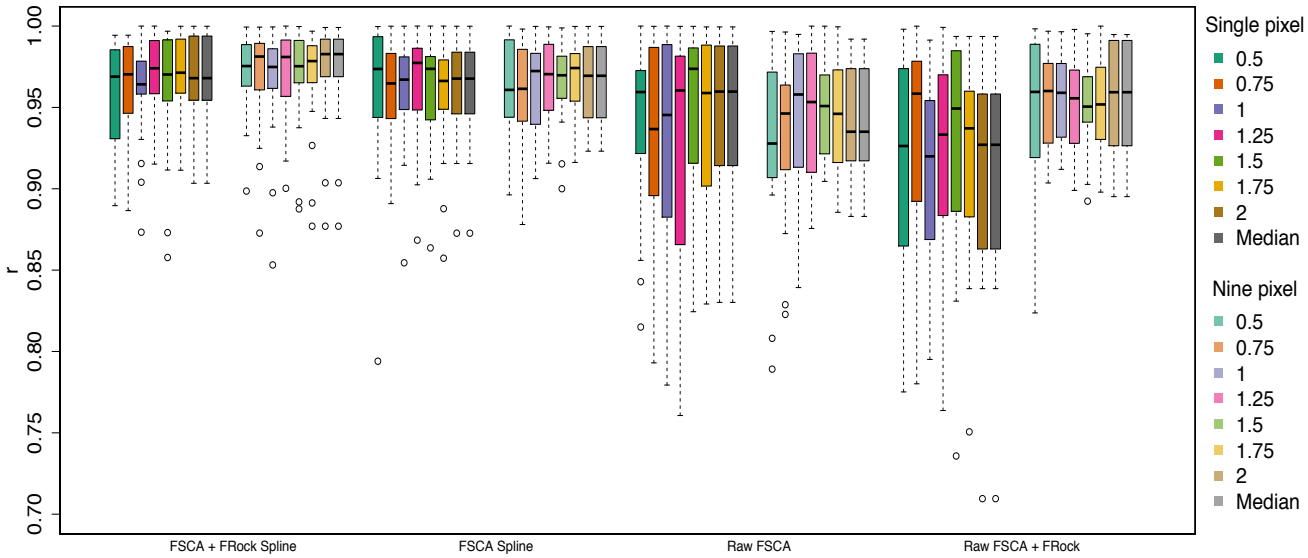

Figure 17: Boxplots showing the distribution of the correlation coefficient between VGF and MLMA among the 25 high-mortality sites. Spread in values represents different correlations for specified MODSCAG endmembers and outlier cutoffs. Boxplots for singe-pixel are shown in darker colors, and 9-pixel (3x3 grid) are shown in lighter colors.

Within the set of correlations using both $F_{SCA} + F_{Rock}$ and a spline, it is difficult to determine which outlier elimination cutoff is best from this simple boxplot. A kernel density plot, akin to a smoothed histogram, helps to elucidate this. Figure 18 shows that for estimates of VGF using $F_{SCA} + F_{Rock}$ and a spline, choosing an outlier cutoff of one standard deviation yields the highest frequency of high correlation coefficients. While the peak is not shifted to the absolute highest correlation coefficient of all sd cutoff choices, the slight reduction in correlation coefficient (from 0.97 to 0.95) is less important than lower frequency of high correlation (22 vs. 18 sites at distribution peaks).

Though using the median of all local minima or a two standard deviation cutoff yields higher values for correlation coefficients, these two methods frequently eliminate no outliers in a year of data. There are important physically-based reasons to exclude some local minima (e.g. non-covered understory yielding anomalously low VGF, or incomplete melt events leaving snow in canopy yielding high VGF estimates), and using an outlier cutoff value that does indeed exclude some values is important for capturing these physical processes of interest, and thus most accurately measuring VGF. Therefore, the best method is selected as using $F_{SCA} + F_{Rock}$ for defining the VGF, a spline to create a yearly timeseries, and one standard deviation from the mean cutoff for outlier elimination.

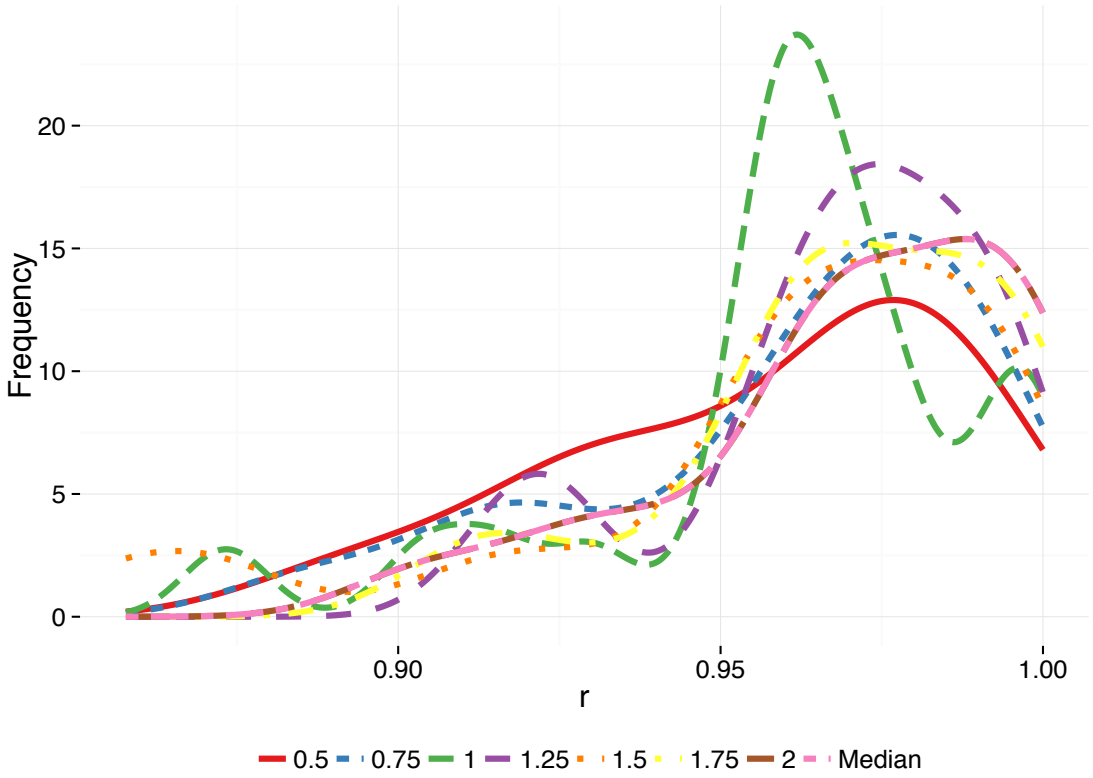

Figure 18: Kernel density plot of correlation between VGF estimates and Meddens Mortality Area timeseries at the 25 selected sites., split by outlier cutoff value, as fraction of standard deviation of all annual LMs. All correlations use a spine-interpolated timeseries of $F_{SCA} + F_{Rock.}$

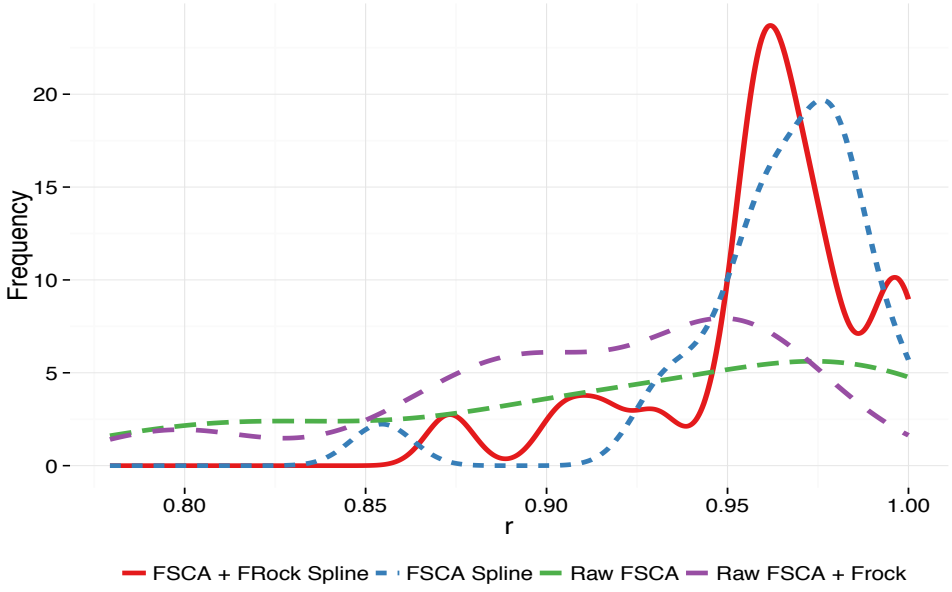

Figure 19: Kernel density plot of correlation between VGF estimates and Meddens Mortality Area timeseries at the 25 selected sites., split by MODSCAG endmembers used, and choice of spline vs. raw timeseries.. All correlations use an outlier cutoff of 1 standard deviation.

It is also possible to choose the best method staring with best outlier cutoff, and then choosing the best MODSCAG endmembers and raw vs. spline timeseries. If the choice is made in this order, results are the same. For an outlier cutoff of one standard deviation, using F_{SCA} + F_{Rock} and a spline yield the highest-frequency of high correlation coefficients as shown in Figure 19.

All further analyses are based on these specific methods: using a timeseries of F_{SCA} + F_{Rock}, spline-interpolation, and an outlier cutoff of 1 sd from the mean.

4.3 NEEDLEFALL TIMING

Q3) How long after mortality does needlefall occur? Is this spatially variable?

Correlations of VGF and MLMA are performed for data shifted 0-4 years after attack, as described in Section 4.2 This gives us a site-specific estimate for how long the needles take to fall. A plot of correlations, with a single best lag-time shown per site is given in Figure 20.

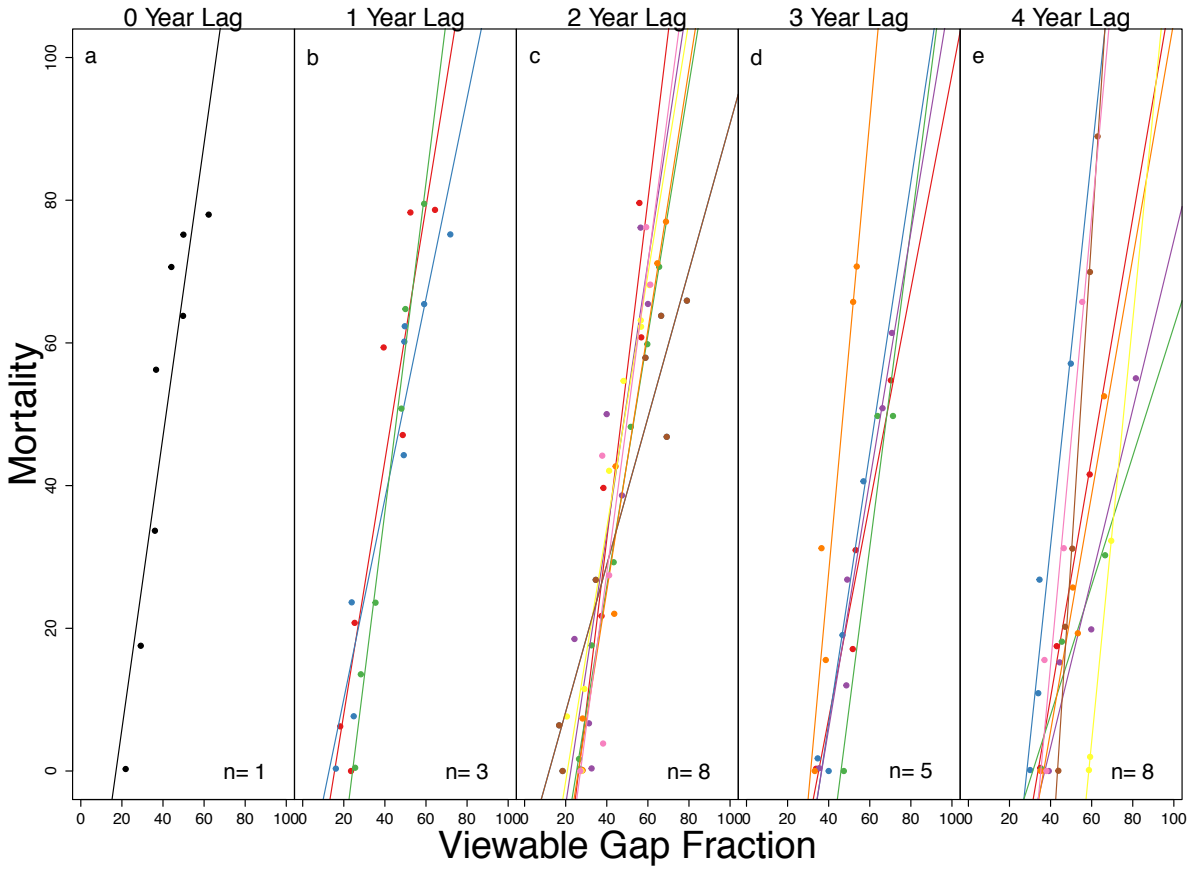

Figure 20: Correlations between mortality (MLMA) and VGF for all sites, split by best correlated lag timing. Each site is shown only once, in the panel that the site had the most highly correlated mortality (MLMA) and viewable gap fraction (VGF). Number of sites per panel is given in the lower right of each plot. Years of lag between green-stage mortality and observed VGF increases from 0 in panel a to 4 in panel e, as noted at the top of each panel.

With the high-mortality sites selected for this study in Northern Colorado, needles most frequently fell 2-4 years after initial green-stage mortality, as shown in Figure 21. This is scale-specific; aggregation to stand-scale (1.5 km^2) showed more sites with a lower 2-year lag-time, while for a single-pixel scale, highest frequency of lag-timing was equally split between 2 and 4 years. This most likely reflects the slower spread of beetle infestation across that larger area, giving a later overall increase in mortality, leading to a shorter estimate of VGF increase, or perhaps simply more variable date of infection and spread of mortality. Average timing of needlefall at the single pixel scale was 2.6 ± 1.2 years.

A summary of lag-time between mortality and needlefall, along with associated site characteristics, including elevation and maximum mortality levels, is given in Table 6.

Table 6: Lag-timing between mortality and needlefall at single-pixel resolution (500 m) for each site, and associated model fit

Location	r2	p	Lag (yrs)	Latitude	Longitude	Elevation (m)	Cumulative MLMA	Yr. Max. Mortality	NLCD 2001	NLCD 2011
Site 1	0.87	<0.01	1	40.2854	-105.8063	2999	82	2007	74	29
Site 2	0.93	0.03	4	40.2479	-105.9104	3108	88	2007	69	29
Site 3	0.91	0.20	3	40.2229	-106.0271	3014	77	2007	68	40
Site 4	0.96	<0.01	3	40.1479	-106.0854	2921	79	2007	69	23
Site 5	0.82	0.01	2	40.0813	-105.7771	3009	82	2008	67	20
Site 6	0.99	<0.01	4	40.1146	-105.8104	2920	91	2006	72	30
Site 7	0.92	0.01	3	40.0896	-105.7896	2921	83	2007	72	35
Site 8	0.92	0.04	4	40.0896	-105.7938	2874	83	2007	70	27
Site 9	0.84	<0.01	0	40.1563	-105.7771	3042	78	2006	67	29
Site 10	0.90	0.01	2	40.0729	-105.7854	2942	86	2008	70	28
Site 11	0.92	<0.01	1	39.9896	-106.0479	2902	75	2006	76	35
Site 12	0.99	0.06	4	41.0646	-106.2771	2647	79	2007	66	30
Site 13	0.93	0.04	4	40.9813	-106.6188	2719	81	2007	76	32
Site 14	0.95	0.03	3	40.3313	-106.0563	2826	76	2008	65	25
Site 15	0.92	<0.01	2	40.2979	-106.1688	3022	77	2006	71	31
Site 16	0.90	0.20	4	40.0646	-106.5563	3077	75	2008	74	47
Site 17	0.99	<0.01	2	40.0479	-106.5104	2986	77	2007	74	24
Site 18	0.76	0.01	2	40.0438	-106.5521	2957	80	2006	76	26
Site 19	0.94	0.03	4	40.2563	-106.2896	3036	78	2007	74	0
Site 20	0.93	0.04	3	40.2813	-106.6604	2916	76	2009	72	34
Site 21	0.96	<0.01	2	40.8563	-106.5854	2762	81	2008	76	0
Site 22	1.00	<0.01	4	40.7979	-106.5688	2643	83	2007	78	33
Site 23	0.94	<0.01	2	39.9438	-106.0604	2879	79	2005	78	0
Site 24	0.92	<0.01	2	40.2979	-106.1688	3022	77	2006	71	31
Site 25	0.98	<0.01	1	39.6688	-106.0521	3214	80	2008	77	37

Timing of needlefall may vary based upon many factors, including site microclimate, especially wind, level of drought stress preceding tree mortality, severity of beetle infestation, and physiographic factors like elevation and levels of snow and rain fall [*Safranyik*, 2004; *Wulder et al.*, 2006]. Determining lag-timing in a spatially-explicit, pixel-by-pixel manner gives the basis for investigating what factors influence the timing of needlefall, across the landscape. For instance, does needlefall occur more quickly in high-wind locations, vs. sheltered? Do north-facing slopes experience slower needlefall, due to higher pre-beetle moisture conditions? Needlefall timing has implications for fire risk, local-scale carbon-cycling, understanding patterns of tree and understory regrowth following mortality, soil moisture, biogeochemical cycling and more.

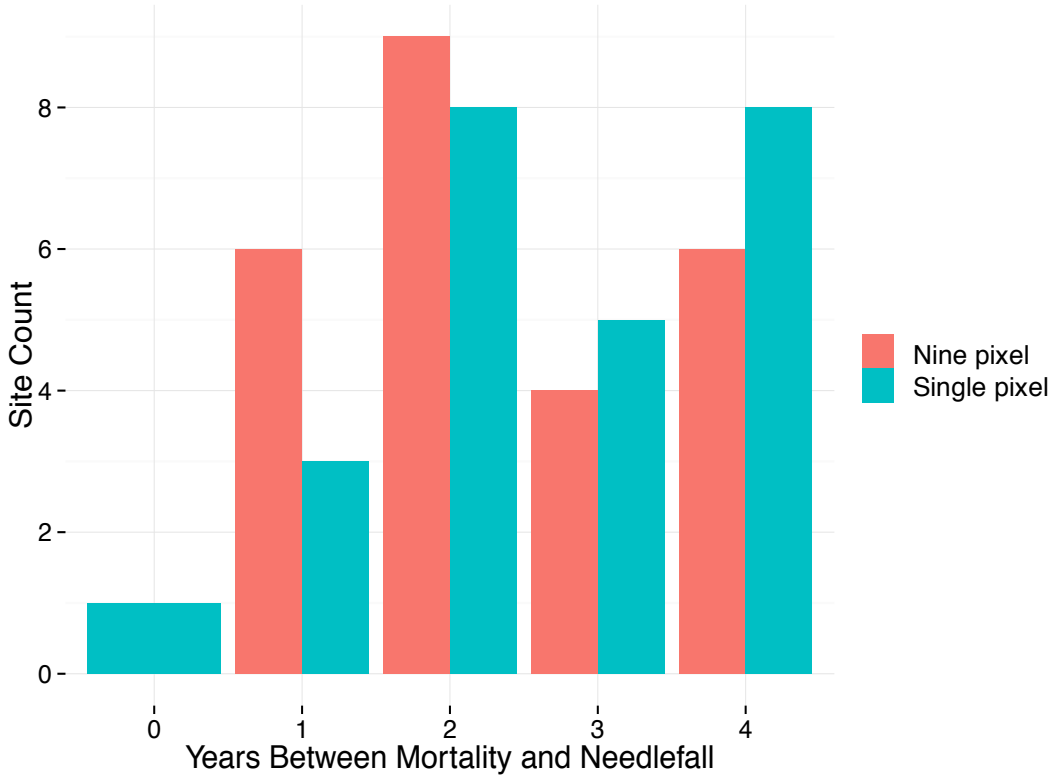

Figure 21: Histogram of lag timing in years between green-stage beetle-induced tree mortality and observed increases in VGF, at single-pixel and aggregated 9-pixel scales.

4.4 DEFOLIATION COEFFICIENT

Q4) How does VGF change with mortality? What level of mortality is required to produce a given increase in VGF in lodgepole forests?

The defoliation coefficient describes the relationship between changes in canopy and severity of mortality; simply, it conveys the expected increase in VGF given a 1% increase in mortality area. Changes in canopy extent due to beetle-induced tree mortality should correspond closely with the level of mortality causing that change. In using the MLMA to quantify beetle-induced mortality, this is explicitly clear: the MLMA gives percent of the pixel composed of dead trees, which is equivalent to the canopy area over which we expect to see change. A single tree dying will not influence the VGF in a 500m pixel substantially; all trees dying should.

We expect the DC to remain relatively constant for a single species; when a lodgepole dies and loses its needles, an approximately consistent proportion of trunk, branches, and twigs should remain, relative to initial canopy area. The DC should theoretically be different in different species, as branch structure and initial canopy differ quite significantly [*Cade*, 1997; *Liu et al.*, 2008; *Meddens et al.*, 2012].

We calculate the DC using both remote sensing (DC_{RS}) and field data (DC_{Field}). The DC_{RS} is relatively consistent among sites, ranging from 0.16 to 0.5, with a mean of 0.33 ± 0.1 for the 25 individual sites; boxplots of differences are shown in Figure 14. It's also useful to conceptualize this change as the mortality level necessary to reach a 1% change in VGF. Numerically, this is simply 1/DC, ranging from 1.9 – 6.1 with a mean of 3.3 ± 1.1. On average, a 1% increase in VGF would require the death of 3.3 % of trees in the pixel area. The DC for all 25 individual sites is shown in Table 3, along with parameters used to calculate it.

DC_{Field} gives only a single value, using a space-for-time substitution. The DC_{Field} is 0.4, which falls within 1 sd of the mean of DC_{RS}. Calculation of the DC_{Field} is shown graphically in Figure 22, where the horizontal red lines are the $\overline{VGF}_{Dead}$ and $\overline{VGF}_{live}$, and $\overline{Area}_{Dead}$ is listed on the bottom portion of the plot.

In calculating the $\overline{Area}_{Dead}$, it was necessary to calculate stand basal area (*SBA*) for all sites; values ranged from 10-102 m^2/ ha, which is comparable to the range of 40-94 m^2/ha found in permanent plots in the Colorado Front Range [*Smith et al.*, 2015]. This adds some confidence in our method for approximating *SBA*. *SBA* is not significantly different between live and dead stands, using a non-parametric Wilcoxon signed rank test (p=0.13), showing that selected stands are suitable for a space-for-time comparison. Stand similarity indicates that the DC_{Field} is not

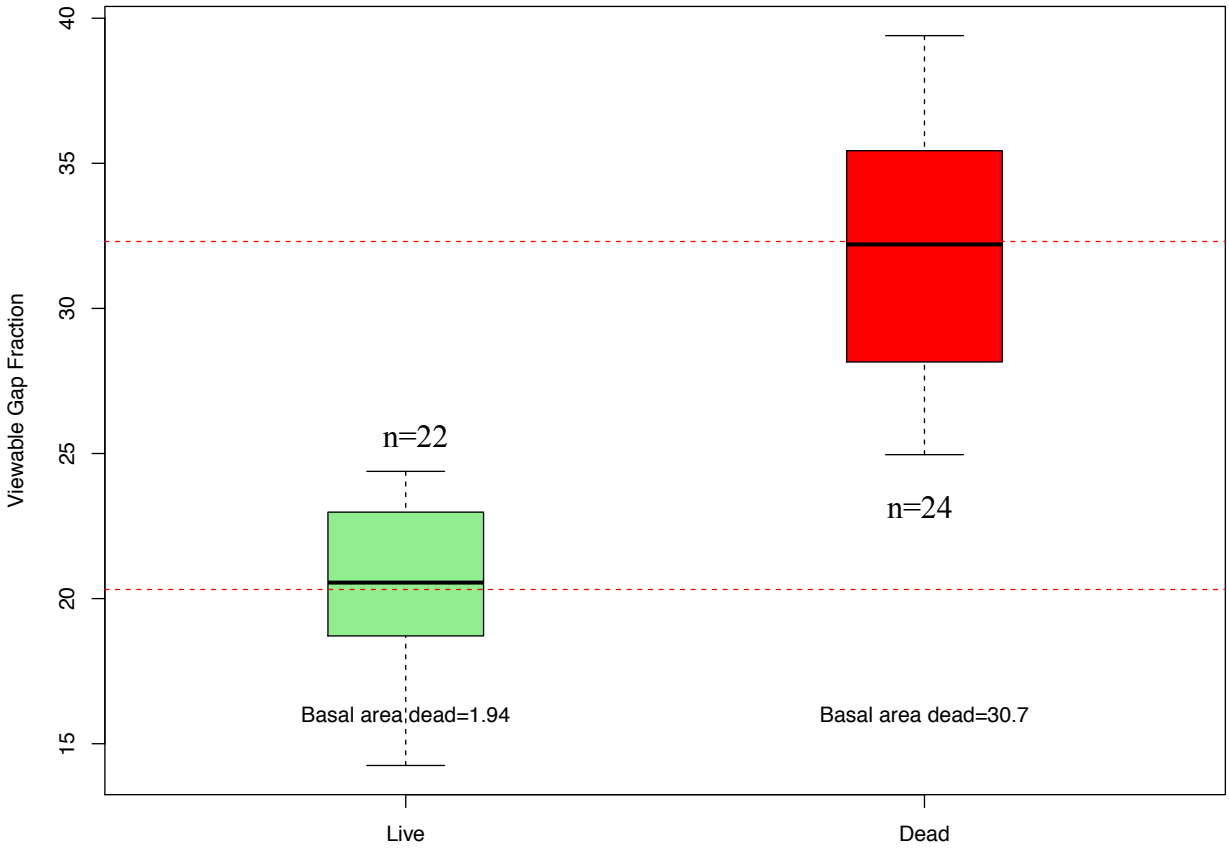

Figure 22: Boxplots displaying the range of VGF measured with hemispherical photograph for live and dead lodgepole pine stands in Northern Colorado. The basal area of dead trees has a median of 30.7 ha/km^2 in dead stands, and 1.94 ha/km2 in live stands. Mean VGF in live stands is 20.3, and mean VGF in dead stands is 32.3. The defoliation coefficient (DC_{Field}) is 0.4.

unduly influenced by the tendency of beetle to attack larger diameter trees, as the live forests have a similar basal are to the dead, and live plots were purposefully located in a currently unimpacted area of the Colorado front range where many large live trees remain.

Though the scales of analysis are different – 0.25 km^2 pixel, versus a forest stand with approximately 300 m^2 camera field of view – the field-based estimate gives confidence that our remotely-sensed measurement of VGF is capturing beetle defoliation effectively.

As this study did not measure dead basal mortality directly, a simple parameterization of change in mortality was tested as well. Calculating the $\Delta Mortality_{Field}$ as simply the change in mean proportion of dead trees between the two mortality classes (0.03 Live, 0.75 Dead), gives a DC_{Field} of 0.2, also within the range of remotely-sensed DC estimates. Hemispherical photography locations, elevation, forest cover, number of live and dead trees, DBH measurements, canopy height, plot area, and calculated basal area of dead trees are given in Table 4.

Table 4: Hemispherical photography site characteristics used for calculating the defoliation coefficient.

Location	Latitude	Longitude	Elevation (m)	Cumulative MLMA	Yr. Max. Mortality	NLCD 2001	NLCD 2011	VGF	Live Trees	Dead Trees	Prop. Dead	DBH Small (cm)	DBH Med. (cm)	DBH Large (cm)	Height (m)	# Trees	Plot area (m^2)	Basal Area Dead (ha/km^2)
Dead 1	39.7708	-105.81634	3031	18	2007	63	51	32.8	16	31	0.66	12	18	23	14	47	127.68	0.61
Dead 2	39.9321	-105.85068	2690	50	2010	67	37	25.19	4	13	0.76	12	19	27	27	17	528.21	0.08
Dead 3	39.93114	-105.85175	2690	50	2010	67	37	24.32	6	18	0.75	14	20	30	16	24	160.98	0.43
Dead 4	39.93069	-105.85218	2690	50	2010	67	37	27.97	1	20	0.95	15	20	26	18	21	212.96	0.32
Dead 5	39.93025	-105.852	2690	50	2010	67	37	26.97	6	18	0.75	8	15	20	17	24	188.69	0.17
Dead 6	39.93055	-105.85138	2690	50	2010	67	37	32.62	4	19	0.83	11	16	22	15	23	144.20	0.30
Dead 7	39.93171	-105.85118	2690	50	2010	67	37	31.04	2	10	0.83	14	20	28	16	12	162.48	0.21
Dead 8	39.93122	-105.85146	2690	50	2010	67	37	31.89	1	11	0.92	11	19	33	17	12	181.46	0.24
Dead 9	39.93049	-105.8507	2690	50	2010	67	37	28.61	7	27	0.79	10	16	23	17	34	196.89	0.31
Dead 10	39.91164	-105.87603	2757	41	2007	75	49	31.91	14	17	0.55	10	15	22	15	31	137.19	0.26
Dead 11	39.90709	-105.88409	2786	20	2007	68	48	25.5	5	19	0.79	12	19	26	20	24	263.98	0.22
Dead 12	39.90698	-105.88618	2786	20	2007	68	48	35.52	4	18	0.82	11	19	27	16	22	162.11	0.35
Dead 13	39.90698	-105.88618	2786	20	2007	68	48	32.23	11	17	0.61	14	20	26	17	28	182.26	0.30
Dead 14	39.90688	-105.88766	2802	20	2007	60	30	27.66	14	28	0.67	12	16	30	19	42	245.59	0.39
Dead 15	39.8758	-105.90118	2935	37	2007	74	49	35.68	3	25	0.89	16	29	38	22	28	317.31	0.51
Dead 16	39.87599	-105.90079	2935	37	2007	74	49	37.78	3	16	0.84	17	30	36	27	19	509.37	0.20
Dead 17	39.882835	-105.89397	2854	35	2007	69	35	34.6	6	13	0.68	20	27	35	20	19	279.56	0.28
Dead 18	39.88968	-105.8972	2908	26	2007	78	51	31.96	8	22	0.73	18	24	35	20	30	276.12	0.44
Dead 19	39.77038	-105.81578	3031	18	2007	63	51	37.51	9	14	0.61	12	17	24	10	23	61.28	0.61
Dead 20	39.77054	-105.8162	3031	18	2007	63	51	34.42	8	17	0.68	12	17	23	15	25	144.91	0.30
Dead 21	39.95358	-105.60445	2829	4	2010	77	64	28.43	12	26	0.68	12	16	24	14	38	127.08	0.52
Dead 22	39.95379	-105.60483	2829	4	2010	77	64	30.79	7	15	0.68	10	17	23	12	22	85.93	0.42
Live 1	39.95362	-105.60381	2781	4	2010	79	63	16.43	8	10	0.56	11	16	21	11	18	66.77	0.32
Live 2	39.933269	-105.57821	2925	6	2009	75	43	17.45	19	0	0.00	14	20	26	12	19	90.93	0.00
Live 3	39.933142	-105.57772	2925	6	2009	75	43	14.29	18	1	0.05	14	19	28	16	19	160.98	0.02
Live 4	39.933072	-105.57756	2925	6	2009	75	43	21.22	33	0	0.00	15	20	26	18	33	212.96	0.00
Live 5	39.938369	-105.56837	2833	2	2010	46	42	21.72	22	3	0.12	8	16	22	14	25	133.14	0.05
Live 6	39.95366	-105.60378	2781	4	2010	79	63	21.29	33	1	0.03	11	14	20	15	34	139.35	0.01
Live 7	39.95353	-105.60406	2781	4	2010	79	63	19.77	23	4	0.15	12	15	23	14	27	131.10	0.07
Live 8	39.95369	-105.60508	2829	4	2010	77	64	18.29	25	5	0.17	14	20	28	19	30	236.15	0.08
Live 9	39.97426	-105.5496	2760	2	2009	65	52	17.14	34	0	0.00	9	12	17	11	34	77.60	0.00
Live 10	39.97427	-105.54996	2760	2	2009	65	52	13.85	22	4	0.15	9	16	22	12	26	87.25	0.10
Live 11	40.0346	-105.5442	3028	2	2010	76	60	15.58	19	0	0.00	11	19	23	14	19	124.29	0.00
Live 12	40.035	-105.544	3028	2	2010	76	60	10.73	32	0	0.00	7	12	54	11	32	70.58	0.00
Live 13	40.0354	-105.5438	3028	2	2010	76	60	NA	29	0	0.00	11	15	20	11	29	77.91	0.00
Live 14	40.0355	-105.5444	3028	2	2010	76	60	13.93	37	6	0.14	11	15	22	12	43	89.92	0.14
Live 15	40.03558	-105.54436	3028	2	2010	76	60	16.11	28	1	0.03	9	15	21	12	29	81.07	0.02
Live 16	40.03675	-105.54565	3028	2	2010	76	60	11.97	32	1	0.03	11	15	21	13	33	103.15	0.02
Live 17	40.03617	-105.54617	3067	2	2010	77	65	13.81	30	1	0.03	8	13	17	12	31	80.44	0.02
Live 18	40.036505	-105.54691	3067	2	2010	77	65	18.63	39	0	0.00	11	17	25	13	39	112.72	0.00
Live 19	40.03684	-105.54765	3067	2	2010	77	65	14.66	34	2	0.06	11	16	21	13	36	111.97	0.04
Live 20	40.03618	-105.54624	3067	2	2010	77	65	13.28	35	0	0.00	10	16	20	11	35	78.23	0.00
Live 21	40.03582	-105.54623	3067	2	2010	77	65	16.76	21	3	0.13	16	21	28	13	24	104.23	0.11
Live 22	40.03537	-105.54628	3067	2	2010	77	65	22.13	33	0	0.00	9	12	16	11	33	79.49	0.00
Live 23	40.03573	-105.54666	3067	2	2010	77	65	17.32	27	2	0.07	11	17	23	12	29	88.25	0.05
Live 24	40.03602	-105.54635	3067	2	2010	77	65	18.33	31	0	0.00	10	13	23	14	31	116.90	0.00

5 DISCUSSION

Our analysis used daily satellite data on land surface cover to track the progression of canopy loss over time, using the 2000's-era mountain pine beetle epidemic in northern Colorado as a test case. We demonstrated that it is possible to measure forest mortality and the progression of needlefall using satellite imagery at a 500 m resolution, using satellite imagery acquired in winter months, when dark evergreen forest canopies contrast starkly with underlying snow.

5.1 LIMITATIONS: INHERENT ISSUES IN MODSCAG

Accuracy of our canopy assessments is limited by errors inherent to the spectral-unmixing process and land surface fractional snow cover products we utilize. Though Landsat-based validation of F_{SCA} shows an RMSE of 0.10, with median differences from Landsat ETM+ data ranging from -0.16 to 0.04, issues with cloud-masking and identifying snow in densely forested environments (> 60% canopy cover) persist [*Rittger et al.*, 2013]. As the unmixing algorithms improve over time, so too will the accuracy of our VGF estimates.

5.1.1 CLOUD MASKING

MODIS atmospherically corrected surface reflectance returns (MOD09GA) are distributed with a native cloud-mask. This flags cloudy pixels and accounts for changing conditions in the atmospheric column between sensor and land surface, which would otherwise impact raw reflectance values and thus estimates of snow cover [*Kotchenova and Vermote*, 2007]. In addition to this native cloud mask, MODSCAG initially used an ad hoc cloud mask combining the native mask with the algorithm's grain size estimate, changing pixels with too-large particle size masked as cloud to snow, and snow with a too-small grain size as cloud [*Painter et al.*, 2009]. However, this is no longer in use, as it commonly omits snow cover in any

pixel composed of over 50% rock, a common occurrence in mountainous environments [*K. Rittger, personal communication*, 2015]. However, the approach may be useful in subalpine, forested environments with lower surface roughness, where the methods presented in this paper are applied. Various band thresholds (optical and thermal) are another method utilized for snow-cloud discrimination [*K. Rittger, personal communication*, 2015]. Despite the long history of the problem and effort given to solving it, issues with a discrimination algorithm persist, especially with high cirrus clouds. An improved cloud-masking scheme is currently in development, using filters based on scene-specific radiative transfer modeling of snow and cloud reflectance [*T. Stillinger, personal communication, 2015*]. Thin clouds present a specific problem, in that they reflect a much smaller portion of shortwave-infrared radiation than thick clouds [*Rittger et al.*, 2013]. Additionally, mixed pixels of snow and rock/soil on the edge of snow cover are often erroneously flagged as cloud, due to elevation of visual reflectance by snow, and inflation of the shortwave-infrared by soil/rock. Soot or dust in snow presents issues as well, as there is no spectral endmember in the library for this [*Painter et al.*, 2012; *Rittger et al.*, 2013]. In addition, MODIS grids have an inherent level of noise, which can cause some bands to drop to zero, rendering accurate snow cover mapping impossible [*Tan et al.*, 2006].

A faulty cloud mask which misidentifies cloud as snow introduces anomalously high values of F_{SCA} into our analyses, which, if not identified with the outlier cutoff procedure, would give erroneously high estimates of VGF. If this were the case, cloudy years would have higher estimates of VGF. As clouds are commonly associated with precipitation, this would most likely be years with high snowfall. Using maximum annual SWE accumulation as a proxy for the annual snowfall regime, we see this is generally not the case: maximum SWE is not correlated with our VGF estimate at 87% of sites, as shown in Figure 23. While this primarily shows that

the annual snowfall regime has only a small effect on our VGF measurements, it also indicates that misidentifications of cloud as snow, and resulting anomalously high F_{SCA} estimates, do not significantly impact our results.

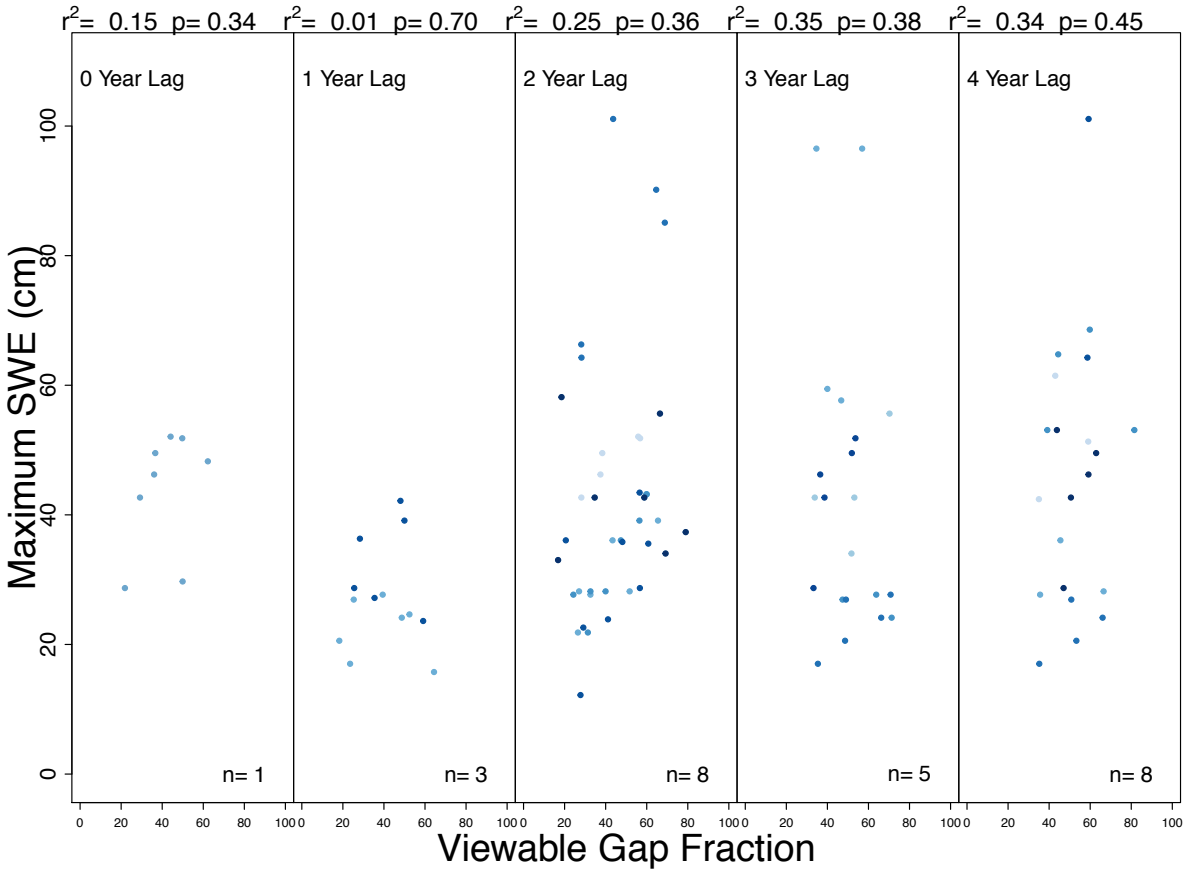

Figure 23: Relationship between annual maximum SWE and VGF estimates, split by site-specific lag-timing of mortality to needlefall. Colors denote different sites. Number of sites per panel is given in the lower right of each plot. Years of lag between green-stage mortality and observed VGF increases from 0 in panel a to 4 in panel e, as noted at the top of each panel.

5.1.2 Projected Pixel Area & Location

The size of MODIS pixels varies based upon the scan angle in both the along and cross-track dimensions. Pixel resolution varies from 0.5 km at nadir to 1.003 by 2.417 km (elongated in the cross-track direction) at the maximum scan angle of 55°, nearly 10 times the pixel area at nadir [*Dozier et al.*, 2008]. Returns on different days are not only viewing from a different angle, but are in fact viewing a different area of a different size, and thus receive a different suite of surface reflectance's from which to run the spectral unmixing algorithm. Base MOD09GA reflectance is resampled to the 500 m resolution, but these initial differences in area sampled are especially important in mountainous areas, where abrupt landscape changes, such as cliffs or areas of wind scour or loading, can be sampled in an adjacent pixel; however, this error is not systematic [*Dozier et al.*, 2008]. Mismatches between swath returns and MODIS-defined grid cells can be significant, especially for high zenith view angles, creating a pixel shift [*Tan et al.*, 2006].

Geolocation certainty is 50 m at nadir, with transformation of the MODIS reflectance products resulting in a 250 m uncertainty, increasing as sensor viewing angles increase [*Wolfe et al.*, 2002]. Landsat-validation of snow cover products suggests a geolocation error of 1-2 pixels (500-1000 m) [*Rittger et al.*, 2013]. Our analysis accounts for this issue with the sine-weighting of sensor zenith angle in the spline and interpolation process of raw MODSCAG values. While this minimizes the issue – weighting F_{SCA} and F_{Rock} values on dates where sensor zenith angle is low more highly than days with poor viewing geometry – it also means that observations of F_{SCA} and F_{Rock} are only observed at nadir, i.e. with very high confidence, once every 16 days. This makes it difficult to identify the precise dates of LMs in the annual timeseries of F_{SCA} and to determine F_{SCA} on those days. Spline interpolation soothes both interception and canopy

unloading, which often occur on the order of a single day or less. In a smoothed timeseries of F_{SCA}, these spikes and dips occur over several days, represented as more gradual processes than in reality. Nonetheless, it is the depth of the dips that impact VGF measurements, not their absolute timing. Annual estimates of VGF are often lower for raw rather than for interpolated timeseries, as shown in Figure 15 in raw F_{SCA} and $F_{SCA} + F_{Rock}$, shown in pink and purple. This is due to the smoothing spline muting the lowest extent of the lows. Thus, smoothing addresses the issue of variable sensor zenith angle and pixel size, but potentially elevates VGF estimates. Correlation coefficients are higher between smoothed timeseries VGF estimates and the MLMA, rather than raw MODSCAG returns for sensor zenith angles < 30°. This suggests that smoothing accounts for important effects of variable pixel size and footprint that using a raw timeseries of low-zenith angle returns does not. Smoothing does, however, elevate VGF measurements: this is true both before and after tree mortality, and so does not highly impact the correlation of VGF with mortality.

5.1.3 PIXEL ILLUMINATION

Shadows can cause MODSCAG to miss snow covered area, due to reduced illumination reflected from the shadowed surface. To account for this, spectral fraction of photometric shade is calculated in the spectral unmixing, and the initial estimate of FSCA is increased to a shade-normalized snow fraction, accounting for topographic effects on irradiance [*Painter et al.*, 2009]. Still, MODSCAG misses snow cover in areas with lower solar illumination [*Rittger et al.*, 2013]. MODSCAG error is not sensitive to the vegetation fraction, but finds little snow at high vegetation fractions as canopy gaps are small and shading of the snow surface interferes with the ability of the spectral-unmixing algorithm to identify the spectral signature of snow. The limit of detection is approximately 60% forest cover [*Rittger et al.*, 2013]. Our sites were selected for

high mortality levels: over 75 ha/km^2 of dead canopy, meaning 75% of the pixel is composed of dead tree canopy. This means that before mortality occurred, tree canopy covered at least 75% of the pixel: this is over the 60% forest cover limit of detection given by Rittger [2013]. This indicates that pre-mortality remote sensing likely underestimates F_{SCA}, which would reduce our pre-mortality assessment of VGF. This would artificially elevate our estimate of canopy change, the DC_{RS}.

MODSCAG has higher performance for larger grain size snow across all land cover types, meaning it performs very well during the initial melt season; at small grain sizes, earlier in the year, shrubs create a range of snow cover differences. Our methods select a time-period and location where shrubs and undergrowth are likely to be covered in snow, decreasing the importance of this limitation.

An illustration of the importance of illumination levels on the spectral unmixing estimates is shown in Figure 24. The three dates shown have ground completely covered by snow and a snow-free canopy, but variable illumination levels. Though this is not the only factor contributing to the date-specific estimate of $F_{SCA} + F_{Rock}$ – sensor zenith angle and the spline interpolation procedure undoubtedly have a large impact as well – we can see that the January date, where the illumination angle is lower, has more shadowing of the snow, and thus a lower estimated VGF. Conversely, the late-April date shown in the rightmost image is on a bright day, with a higher than expected VGF estimate, where without the image, we might have expected residual snow in the canopy. Both of these outliers are eliminated with the cutoff procedure from our VGF estimates, but show the importance of illumination conditions on optical remote sensing estimates of F_{SCA}. This casts doubt on the use of F_{SCA} estimates for a single date and

pixel, as opposed to a larger area or general trend (i.e. date of snowfall approximate to date timeseries begins increasing from a LM).

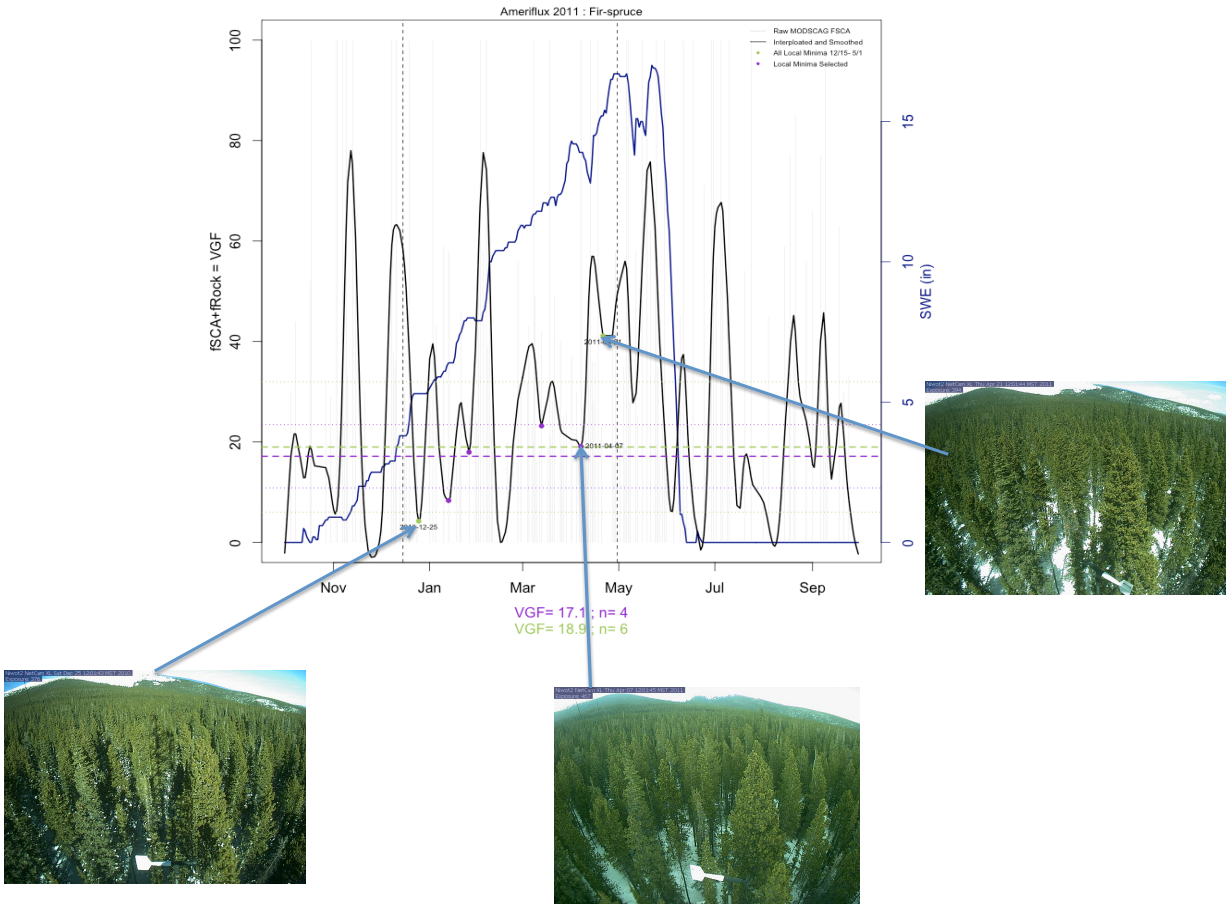

Figure 24: A timeseries of FSCA + FRock for Niwot Ridge, in the Colorado Front Range, showing midday photographs taken on indicated dates of local minima. Raw MODSCAG values are shown in light grey. A spline-interpolation is given as a solid black line Vertical dashed lines delineate winter season when undergrowth is assumed to be snow-covered. Points show local minima (LMs) in the timeseries, within the winter time window. Purple dashed horizontal line shows measurement of VGF for that year. Light green dashed horizontal lines delineate LMs used to calculate VGF from those deemed unrepresentative. Purple points are used to calculate the VGF. Green points are discarded as outliers not representative of target canopy conditions. Imagery is used to evaluate that assumption.

5.2 TIMING OF NEEDLEFALL

For the high-mortality sites selected in this research, needles most frequently fell 2-4 years after initial green-stage mortality. This is dependent on scale: at 500 m resolution, the most frequently occurring lag time was equally split between 2 and 4 years. At a 1.5 km resolution, the most frequent lag-time was 2 years, as shown in Figure 21. This difference in observed needlefall timing is likely a reflection of the slower and more variable spread of beetle-induced mortality across a larger area, giving a delayed increase in mortality, which in turn leads to a shorter lag time between beetle-induced mortality and VGF increase. Average needlefall lagged mortality at a 500 m scale by an average of 2.6 ± 1.2 years. Progression of beetle-induced mortality stages, from green to red to grey, has inherent variability in timing, as observed in many field studies [e.g. *Safranyik*, 2004; *Wulder et al.*, 2006]. This is likely based on factors including site microclimate, drought stress prior to beetle infestation, severity of beetle attack, and physiographic factors including elevation and precipitation regime.

In our analysis of needlefall timing, the progression of beetle attack occurred faster at higher elevations, where there was a shorter lag time between mortality and needlefall. This is shown in Figure 25, where an increase in elevation of 300 m corresponds to a 1-year decrease in lag timing (r^2=0.14, p=0.05). Lag timing is not equally distributed, as it is an ordinal value; a Spearman's ranked correlation confirms the negative relationship between the variables, though with a slight reduction in significance level (r=0.38, p=0.06).

Higher elevation trees are subject to higher winds and increased snowfall. After tree mortality, as needles begin to lose moisture and become brittle, it stands to reason that the higher stresses on high elevation trees from higher winds and increasing snowfall volumes will cause brittle needles and small twigs to fall from branches more quickly than at lower elevation locations.

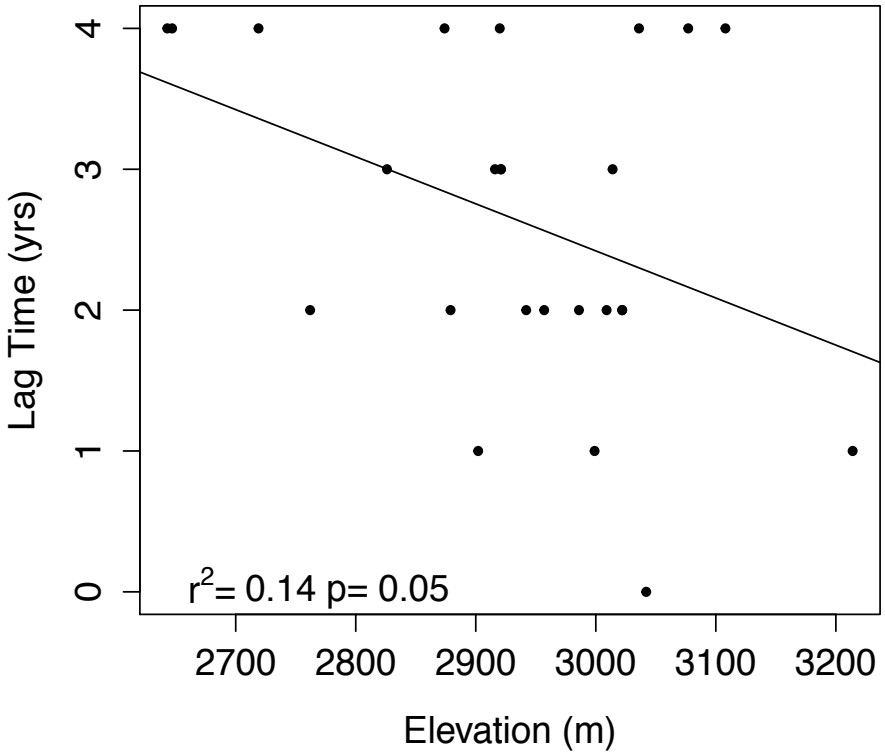

Figure 25: Relationship between needlefall lag timing and elevation. For every 300m increase in elevation, the lag-timing between mortality and needlefall is reduced by one year.

An alternate explanation for this relationship is simply that our VGF measurement method works differently in snowier regimes, represented here by higher elevation forests. With the long window for detecting LMs, from December 1st – May 15th, lower-elevation sites likely have a much longer timeframe during which our target conditions of snow-free canopy and snow-covered understory are not met. Thus, we would expect a better relationship between VGF and MLMA at high-elevation sites.

Confoundingly, we observe the opposite effect, as shown in Figure 26, which displays the relationship between VGF-MLMA r^2 and site elevation. The relationship is not highly significant (p=0.10), however. Thus, the correlation between VGF-MLMA model fit and elevation, though promising conceptually, is likely misleading, as the correlation is not significant, and is may rather be result of a small range in both r^2 and elevation in the current dataset.

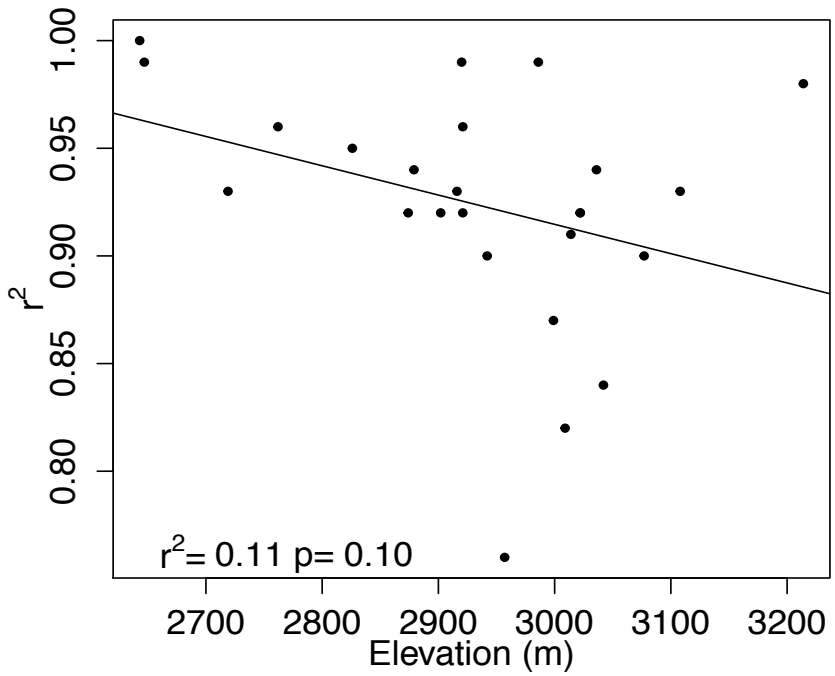

Figure 26: Relationship between model fit of VGF-MLMA (r^2) and site elevation, for all 25 high-mortality sites. An increase in elevation of 300 m corresponds to a decrease in r^2 of 0.4, signifying a decrease in model explanation of variance of 4%.

Additionally, we see no correlation between needlefall timing and a suite of other environmental site parameters: maximum mortality level measured by MLMA, year of maximum mortality, canopy cover as measured by NLCD datasets, the defoliation coefficient, aspect, northness as measured by cosine of aspect, or mean VGF before or after beetle kill ($p > 0.1$). We would expect to see a significant relationship with many of these variables.

We do observe a correlation between the latitude and lag timing ($r = 0.42$, $p < 0.05$), and elevation and latitude ($r = -0.77$, $p < 0.01$), however. These correlations within our sites in Northern Colorado are spurious: there is no reason that elevation and latitude, independent

physiographic parameters, would be related in our dataset, except by accident of random site selection. Additionally, the observed range of latitude in our dataset is only 1.4°, not a large enough spread for any realistic differences in illumination angle or reflected light to impact the spectral unmixing procedure. Indeed, the confounding negative relationship between r^2 and elevation at our sites could simply be the effect of collinearity between elevation and latitude.

The limiting factor in this analysis is likely the limited range of sites, in terms of both beetle-induced mortality and elevation range. Future work should include a larger number of sites, spanning a greater elevation range and wider degree of beetle-induced mortality. In Colorado, lodgepole pine grow from approximately 2500 to 3300 m in elevation [*CSFS*, 2007]. Our sites fall from 2643 m to 3241 meters, a substantial portion of that range. Using a non-lodgepole-specific mortality validation dataset would allow for expansion to higher and lower elevations. The spruce mortality dataset developed by Hart [2015] would allow expansion of upper elevation bound. Using ADS-based Meddens data (MADS-MA) would allow for expansion to all western forests, but would add additional uncertainty, due to known issues with ADS-derived data. A lowered threshold for mortality would allow selection of more sparsely forested pixels, potentially enhancing the ability of satellite remote sensing to detect snow cover, and improving measurements of VGF, especially pre-mortality with higher canopy closure. A larger elevation range would allow for more robust analysis of environmental and physiographic impacts on needlefall lag-timing.

5.3 THE DEFOLIATION COEFFICIENT (DC)

The DC relates observed changes in canopy area to the level of mortality causing the change. We argue that the DC is an inherent characteristic of a particular tree species, relating to the relatively consistent proportion of trunk and limb area per unit of canopy.

Using remote sensing to define a DC requires selection of pixels where there is little variability in sub-pixel tree species. In Colorado's lodgepole pine forests, this is easily satisfied. Lodgepole pine forests frequently grow uniformly, most following hot, stand-replacing fires [*CSFS*, 2007]. This results in an even-aged, very uniform forest. Prolific regeneration of small saplings following fire often results in extremely high-density forest stands with over 20,000 trees per acre. These are colloquially known as 'dog-hair' stands [*CSFS*, 2007]. The extreme uniformity of trees in these stands allows for the calculation of a species-specific DC quite well, as stand-complexity is very low. Sites selected in this study were required to have a minimum mortality of 75 ha/km^2. This means that 75% of pixel area is composed of dead canopy, indicating that the pixel was very densely forested initially – very likely a dog-hair lodgepole stand. The 2001 NLCD for all sites has a mean value of 72% forest cover across all sites, supporting this idea.

Calculating the DC would ideally define canopy cover in periods entirely before and entirely after beetle kill, pixels with either completely green or grey-stage trees. This is not a realistic goal, however; beetle-induced mortality spreads in non-uniform patterns from tree-to-tree, likely leaving a mosaic of morality stages within a single 500 m pixel for a given year. We are limited to defining the timing of stage progression by spectral characteristics – calculated by Meddens [2014] using spectral indices at a 30 m Landsat resolution – but aggregated to a 500 m resolution in order to match our MODIS-based measurements of VGF.

Additionally, this analysis uses VGF data from only 2001-2012. The average year of maximum single-year beetle-induced tree mortality was 2007. In order to divide the years of VGF measurements into two mortality stages, the year of peak beetle-induced mortality was identified, and a buffer of one year before and after was applied.

Giving a buffer of one year lessens any effect of poor identification of beetle-kill peak timing by the MLMA, and also allows one year for needlefall occurring in the peak year to occur before measuring resulting VGF. Ideally, a larger buffer could be applied to compare years completely before and after beetle-induced mortality; we know some of our sites require 4 years for most needlefall to occur. However, constrained to a twelve year MODIS-era dataset, we did not have the luxury of eliminating a larger number of years in intermediate, mixed stages, while retaining a dataset of any size suitable for statistical analysis. A single year is not suitable to define either pre- or post-beetle VGF, as there is substantial year-to-year noise in our method, shown in Figure 12. This variability is overwhelmed by changes due to tree mortality, but use of a single year in each mortality stage to calculate the DC would introduce increased uncertainty and unknown biases, depending on snowfall regime for year selected. The inclusion of some mixed-mortality years in the calculation of the DC likely decreases our estimate. If pre-mortality VGF includes some years where needles have begun to fall, our beginning VGF will be too high, and if our post-mortality VGF includes some years where some trees remain green or red, final VGF will be too low; VGF change will be underestimated, reducing the DC. A longer period of record could help with this problem, but might begin to measure regrowth where understory and saplings are above snow in winter months.

Additionally, changing snow surface illumination impacts VFG measurements. As needles fall, there will be less shadowing on the snowpack, improving the ability of the MODSCAG algorithm to detect $F_{SCA.}$ More shadowing before needlefall will artificially reduce VGF measurements, and increased surface illumination following needlefall will enhance the ability of MODSCAG to accurately retrieve $F_{SCA.}$ This will result in some overestimation of VGF change, increasing the DC.

Inclusion of mixed-stage mortality years in estimates of pre and post-mortality VGF are likely a dominant feature in the DC, affecting the calculation more than the influence of changing illumination conditions. These two effects have an opposing effect on estimated VGF change, likely offsetting each other to some degree. Still, if we consider the mixed-mortality stage factor dominant, this indicates that the DC is a conservative estimate of canopy change.

The DC is positively correlated with elevation, as shown in Figure 27. For each 100 m increase in elevation, the DC increases by 0.03. At higher elevations, the same change in mortality will give a larger change in VGF. There is no correlation between elevation and NLCD canopy cover, so the effect of shading on F_{SCA} retrievals should be the same at all elevations. Therefore, the relationship between the DC and elevation is most likely explained by the increased speed of needlefall at higher elevations. We know that the DC incorporates several years of potentially mixed mortality into assessment of post-mortality VGF, underestimating the DC. At higher elevations, needles fall more quickly, due to higher winds and snowfall volumes. Therefore, fewer years of mixed-

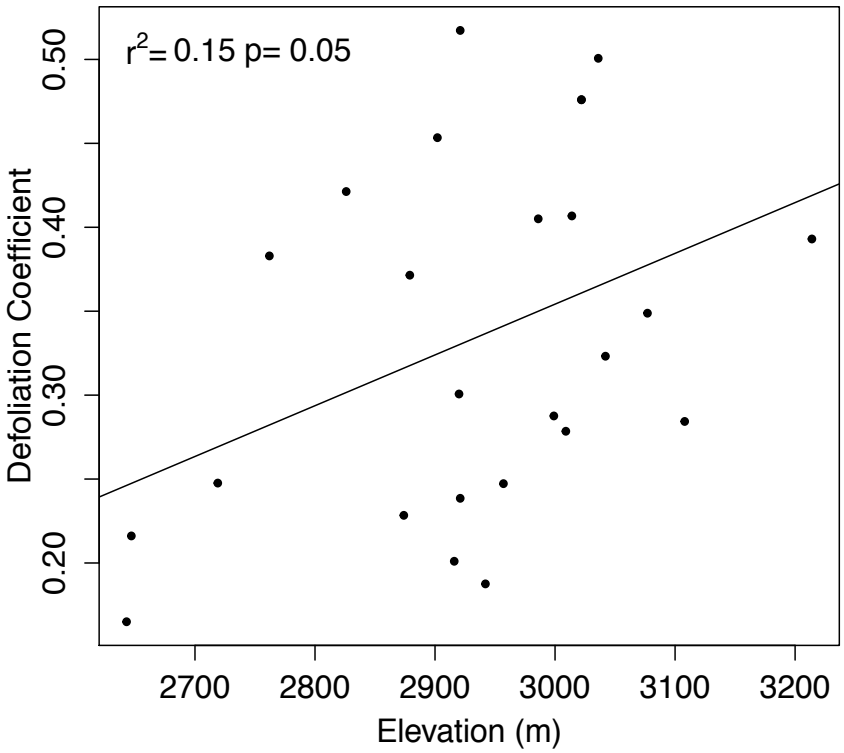

Figure 27: Relationship between the defoliation coefficient and elevation. A 100 m increase in elevation yields an increase in the defoliation coefficient of 0.03.

mortality stage are incorporated into post-beetle VGF estimates at high elevation. This reduces the underestimation bias of VGF change in the DC. Therefore, high-elevation DC is likely an improved estimate, with less underestimation error due to the effects of mixed-mortality stage in the post-mortality VGF estimate.

Beyond elevation, the DC is not correlated with any site-specific environmental, physiographic, or VGF-MLMA correlation parameter we tested. DC is not correlated with latitude, aspect, northness as measured by cosine of aspect, canopy cover as measured by NLCD datasets, year of maximum mortality, or goodness of fit of the MLMA-VGF relationship ($p > 0.1$). This reflects the status of the DC as an inherent characteristic of a particular tree species, relating to the consistent relationship of trunk and limb area to canopy, rather than any other site-specific environmental parameters.

The DC shown here is exclusively for lodgepole pine forests. A rapidly expanding spruce beetle epidemic has caused increased interest for spruce-specific mortality assessments. Detection of spruce mortality presents a special problem, as it is characterized by a short-lived yellow-green stage, followed by grey-stage, with no red-stage at all [Johnson et al., 1997]. This difference limits the applicability of lodgepole mortality detection methods to spruce-fir forests, but a newly available dataset on spruce beetle-induced mortality promises the ability to calculate a DC and lag-timing between mortality and needlefall for spruce trees [*Hart and Veblen*, 2015]. Spruce trees tend to retain more branches and twigs than lodgepole pine, which would give a substantially smaller DC, though this may be complicated by the tendency of spruce to grow in mixed spruce-fir stands. This is a promising avenue for future work.

5.4 Contribution of work and potential implications

The methodology we develop here adds a novel technique to common remote-sensing methods of detecting beetle-induced mortality. Current methods use the spectral signature of dying trees to identify timing and extent of red-stage forest; area of dead trees is distinct from canopy area lost, however. To quantify changes in canopy area, our method explicitly maps canopy extent at the sub-pixel fractional level, rather than relying on the spectral signature of dying trees, which can be muted by the presence of live trees or other sub-pixel landcover types (e.g. rock). Our method is designed to avoid convolving understory and canopy area, a recognized issue in other MODIS-based vegetation products [*Coops and Wulder*, 2010; *Bowler et al.*, 2012; *Heiskanen et al.*, 2012; *Bright et al.*, 2013; *Livneh et al.*, 2015]. Our technique has the potential to supplement existing canopy mapping methods, as these other products are not produced on annual timescales (e.g. the NLCD; University of Maryland Global Forest Change [*Homer et al.*, 2004; *Hansen et al.*, 2013]). Using MODIS-derived fractional snowcover products yields new insight into spatially-explicit, canopy-specific forest extents on a yearly timeframe, integrating all change, whether due to beetle-induced mortality, drought, fire, or expansion of forest canopy.

Our methodology can be applied anywhere in the seasonal snow zone, which is where currently expanding disturbances of great concern – fire and spruce beetle – are centered in western North America [*Westerling et al.*, 2006; *Williams et al.*, 2012; *Gleason et al.*, 2013; *USFS*, 2015]. Drought mortality rates are increasing broadly as well, including areas in the seasonal snow zone [*Allen et al.*, 2010; *Williams et al.*, 2012; *Smith et al.*, 2015]. The seasonal snow zone covers up to 30% of the global land surface seasonally, up to 50 million km^2 [*Vikhamar and Solberg*, 2003], and contains 40% of global forests [*Stueve et al.*, 2011]; forests cover 40% of the North American seasonal snow zone [*Klein et al.*, 1998]. Hence, the methods

presented here have wide potential application in quantifying regional forest die-offs occurring both now and in the coming decades. A warming climate is an important driver of forest disturbances, creating higher frequency of warm winters during which beetles thrive, as well as increasing fire area burned and rates of drought-related mortality, along with drought-related susceptibility to a suite of forests pests [*Westerling et al.*, 2006; *Raffa et al.*, 2008; *Allen et al.*, 2010].

There is broad public interest in the relationship of beetle-related mortality within forest ecosystems, owing to their visibly obvious impacts on a variety of sectors, from fire risk and timber production to hydrology and global climate. The research community has responded to this, with much recent work on beetle-associated fire risk, hydrologic impacts, carbon cycling, and global climate impacts. In order to determine the impact of beetle-induced mortality on these ecosystem services of interest, it is often necessary to quantify the mortality in a spatially-explicit manner. Thus, many of these studies use ADS-derived maps of beetle-induced mortality, introducing error in assessing impacts. Additionally, as ADS and spectrally-derived estimates of beetle-induced mortality give year of red-stage trees, additional assumptions must be made if the quantity in question is really the impact of changing canopy extent. Our methodology gives that directly.

Fire risk in western forests is of great public concern. Widespread forest mortality changes fuel conditions, moving potentially flammable needles and twigs to the ground, and removing them from the canopy. This may impact the behavior of future fires in an area, though it has been shown that dead forests do not impact either area burned or burn severity [*Simard et al.*, 2011; *Jenkins et al.*, 2012; *Hart et al.*, 2015]. Our VGF metric identifies the timing of

needlefall, which corresponds to the change in fuel location from canopy to surface, and can potentially inform research on this topic.

Watershed-scale impacts of changes to evapotranspiration, ground moisture, and snow interception and melt processes remain relatively unknown, beyond the plot scale. Changes to evapotranspiration (ET) likely occur when trees first die, during green-stage mortality. Other changes are related to reduced canopy, and are properly linked to the onset of grey-stage mortality. There are conflicting reports of streamflow impact in different regions of the western North America; some of this may be due to uncertainties inherent in ADS-derived beetle mortality information, obscuring timing and exact process-based knowledge of beetle impacts. Studies show that late-summer groundwater contributions to streamflow are increased in MPB killed forests, due to loss of forest ET; this work used ADS data to identify timing of beetle impacts [*Bearup et al.*, 2014]. Another modeling study using ADS data shows an increase in annual water yield of 8-13% [*Livneh et al.*, 2015]. This has not been observed in streamflow records, likely due to post-mortality increases in understory vegetation. One would predict major shifts in the hydrologic regime with the death of large swaths of forested areas within a watershed. This has not yet been shown with streamflow data; use of ADS-derived mortality may be one factor, if change in canopy area is in fact the driving process of interest.

Forest mortality has significant effects on global climate, through changes in the carbon cycle and land surface albedo. Death of trees reduces uptake of atmospheric carbon, turning forests from carbon sinks to carbon sources [*Hicke et al.*, 2012]. Decomposition of dead biomass returns previously stored carbon to the atmosphere, though forest regrowth is a significant carbon sink a few years after canopy removal. Timing of tree death and needlefall are critical to understanding whether a beetle-impacted forest will act as a carbon source or sink. Partially

offsetting the carbon released during needlefall decomposition, tree mortality significantly increases winter land surface albedo [*O'Halloran et al.*, 2012]. Change to land surface albedo is due to needlefall and reduced canopy extent, not explicitly to forest mortality explicitly. The DC can be used to estimate changes to albedo due to projected future mortality levels.

Additionally, VGF is a required input for a variety of landsurface and hydrologic models. Our approach for measuring VGF could create these inputs, or our measurements of DC could be used to adjust static canopy data, for pre- or post-mortality conditions.

Another potential use for our VGF metric is to fill gaps in existing ADS datasets. Our metric is well-correlated with the MLMA, which has a higher accuracy than ADS-derived measures of morality area. Thus, for areas or time-periods when ADS data is not available, it is possible to use our VGF methodology to calculate mortality area. This is especially useful in areas where ADS are not routinely flown, due to lack of funding, or to National Park and Wilderness area restrictions. If an area were not flown in a given year of interest, applying our VGF estimation methods would give a timeseries of VGF, which could be used to estimate ADS values in years with no flights, or could simply be used as a separate metric of canopy change.

6 CONCLUSIONS

New methods for quantifying integrated forest change – regardless of cause or direction – are needed, as drought, non-MPB insect mortality, and fire continue to expand in forests across western North America [*Westerling et al.*, 2006; *Allen et al.*, 2010; *Hart et al.*, 2014; *Smith et al.*, 2015]. This thesis proposes and tests one such method, using remotely-sensed estimates of snow-cover fraction. Once expanded from the current point-scale to landscape-scale analysis, this work holds promise for integration into varied land-surface and hydrologic models as a dynamic vegetation field, able to capture change quickly and more accurately represent the land surface than an unchanging single-date estimate of canopy cover, hopefully improve modeling results related to hydrology, biogeochemical and carbon cycling, and more. Empirically-based hydrologic models (e.g. SNOW-17) rely upon stationarity – the assumption that past behavior of hydrologic systems are representative of that of the future; with the impacts of anthropogenic climate change increasing, this assumption is no longer valid [*Bales et al.*, 2006; *Knowles et al.*, 2006; *Service et al., 2004]*. Thus, physically-based models are becoming ever more critical; incorporating knowledge of a dynamic forest cover fraction holds promise to add meaningfully to these modeling frameworks.

Additionally, our methodology can be used to model MPB mortality area – either Landsat-based or ADS-based – in areas where it is not currently available. ADS flights are costly and time-consuming, and are often not flown on an annual basis, for a given area of interest. The ability to hind-cast mortality in years of unknown value could be valuable for many research applications.

From a future-oriented perspective, our calculation of a defoliation coefficient can be applied predictively to assess potential VGF impacts of MPB infestation to an as-yet unimpacted

watershed of interest. It could be used to develop scenarios for different levels of beetle impact, and perhaps aid in planning for each case.

While MODSCAG- and fractional snow covered area estimates are currently only available operationally at a 500 m resolution, development of a joined MODIS-Landsat product at the 30 m resolution is currently under development [Rittger, in prep]. Once this becomes available, our methodology could provide annual VGF estimates at a 30 m resolution.

Forests hold vast global value, providing countless ecological, societal, and climate benefits to humanity, and indeed all living things on the planet. Our research provides a novel methodology for understanding this spatially and temporally variable, precious resource.

7 REFERENCES

Adams, H. D., A. K. Macalady, D. D. Breshears, and N. L. S. C. D. ALLEN (2010), Climate Induced Tree Mortality: Earth System Consequences, *Eos, Trans. …*, *91*(17), 2009–2010, doi:10.1111/j.1469-.

Allen, C. D. et al. (2010), A global overview of drought and heat-induced tree mortality reveals emerging climate change risks for forests, *For. Ecol. Manage.*, *259*(4), 660–684, doi:10.1016/j.foreco.2009.09.001.

Bales, R. C., N. P. Molotch, T. H. Painter, M. D. Dettinger, R. Rice, and J. Dozier (2006), Mountain hydrology of the western United States, *Water Resour. Res.*, *42*(8), n/a–n/a, doi:10.1029/2005WR004387.

Barnett, T., J. Adam, and D. Lettenmaier (2005), Potential impacts of a warming climate on water availability in snow-dominated regions., *Nature*, *438*(7066), 303–9, doi:10.1038/nature04141.

Bearup, L. A., R. M. Maxwell, D. W. Clow, and J. E. Mccray (2014), Hydrological e ects of forest transpiration loss in bark beetle-impacted watersheds, *Nat. Clim. Chang.*, *4*(6), 481–486, doi:10.1038/NCLIMATE2198.

Bentz, B., C. Allen, M. Ayres, A. Carroll, and M. Hansen (2009), *Bark beetle outbreaks in western North America: Causes and consequences.*, edited by B. Bentz, Univ. of Utah Press, Salt Lake City, UT.

Bewley, D., Y. Alila, and A. Varhola (2010), Variability of snow water equivalent and snow energetics across a large catchment subject to Mountain Pine Beetle infestation and rapid salvage logging, *J. Hydrol.*, *388*(3-4), 464–479, doi:10.1016/j.jhydrol.2010.05.031.

Biederman, J. a., P. D. Brooks, a. a. Harpold, D. J. Gochis, E. Gutmann, D. E. Reed, E. Pendall, and B. E. Ewers (2012), Multiscale observations of snow accumulation and peak snowpack following widespread, insect-induced lodgepole pine mortality, *Ecohydrology*, n/a–n/a, doi:10.1002/eco.1342.

Bonan, G. B. (2008), Forests and climate change: forcings, feedbacks, and the climate benefits of forests., *Science*, *320*(5882), 1444–1449, doi:10.1126/science.1155121.

Boon, S. (2007), Snow accumulation and ablation in a beetle-killed pine stand in Northern Interior British Columbia, *J. Ecosyst. Manag.*, *8*(3), 1–13.

Boon, S. (2009), Snow ablation energy balance in a dead forest stand, *Hydrol. Process.*, doi:10.1002/hyp.

Bowler, R., A. L. Fredeen, M. Brown, and T. Andrew Black (2012), Residual vegetation importance to net CO 2 uptake in pine-dominated stands following mountain pine beetle attack in British Columbia, Canada, *For. Ecol. Manage.*, *269*, 82–91, doi:10.1016/j.foreco.2011.12.011.

Bowman, W. (1992), Inputs and storage of nitrogen in winter snowpack in an alpine ecosystem, *Arct. Alp. Res.*, *24*(3), 211–215, doi:10.2307/1551659.

Bright, B. C., J. a. Hicke, and A. J. H. Meddens (2013), Effects of bark beetle-caused tree mortality on biogeochemical and biogeophysical MODIS products, *J. Geophys. Res. Biogeosciences*, *118*(February), n/a–n/a, doi:10.1002/jgrg.20078.

Brooks, P. D., P. Grogan, P. H. Templer, and P. Groffman (2011), Carbon and Nitrogen Cycling in Snow-Covered Environments, , *9*, 682–699.

Buma, B., E. T. Pugh, and C. a. Wessman (2013), Effect of the current major insect outbreaks on decadal phenological and LAI trends in southern Rocky Mountain forests, *Int. J. Remote Sens.*, *34*(20), 7249–7274, doi:10.1080/01431161.2013.817717.

Burles, K., and S. Boon (2011), Snowmelt energy balance in a burned forest plot, Crowsnest Pass, Alberta, Canada, *Hydrol. Process.*, *3029*(March), n/a–n/a, doi:10.1002/hyp.8067.

Cade, B. S. (1997), Comparison of tree basal area and canopy cover in habitat models: Subalpine forest, *J. Wildl. Manage.*, *61*, 326–335, doi:10.2307/3802588.

Chapman, T. B., T. T. Veblen, and T. Schoennagel (2012), Spatiotemporal patterns of mountain pine beetle activity in the southern Rocky Mountains., *Ecology*, *93*(10), 2175–85.

Coops, N. C., and M. a. Wulder (2010), Estimating the reduction in gross primary production due to mountain pine beetle infestation using satellite observations, *Int. J. Remote Sens.*, *31*(8), 2129–2138, doi:10.1080/01431160903474947.

Coops, N. C., M. Johnson, M. a. Wulder, and J. C. White (2006), Assessment of QuickBird high spatial resolution imagery to detect red attack damage due to mountain pine beetle infestation, *Remote Sens. Environ.*, *103*(1), 67–80, doi:10.1016/j.rse.2006.03.012.

Crane, R. G., and M. R. Anderson (1984), Satellite discrimination of snow/cloud surfaces, *Int. J. Remote Sens.*, *5*(1), 213–223, doi:10.1080/01431168408948799.

CSFS (2007), 2006 Report on the Health of Colorado's Forests. Special Issue: Lodgepole Pine Foresets, *Eff. Br. mindfulness Interv. acute pain Exp. An Exam. Individ. Differ.*, doi:10.1017/CBO9781107415324.004.

Dennison, P. E., S. C. Brewer, J. D. Arnold, and M. a. Moritz (2014), Large wildfire trends in the western United States, 1984-2011, *Geophys. Res. Lett.*, *41*(33), 2928–2933, doi:10.1002/2014GL059576.

Dietz, A. J., C. Kuenzer, U. Gessner, and S. Dech (2012), Remote sensing of snow – a review of available methods, *Int. J. Remote Sens.*, *33*(13), 4094–4134, doi:10.1080/01431161.2011.640964.

Dozier, J. (1989), Spectral Signature of Alpine Snow Cover from the Landsat Thematic Mapper, , *22*(August 1988), 9–22.

Dozier, J., T. H. Painter, K. Rittger, and J. E. Frew (2008), Time–space continuity of daily maps of fractional snow cover and albedo from MODIS, *Adv. Water Resour.*, *31*(11), 1515–1526, doi:10.1016/j.advwatres.2008.08.011.

Ellis, C. R., J. W. Pomeroy, R. L. H. Essery, and T. E. Link (2011), Effects of needleleaf forest cover on radiation and snowmelt dynamics in the Canadian Rocky Mountains, *Can. J. For. Res.*, *41*(3), 608–620, doi:10.1139/X10-227.

Erickson, T. a., M. W. Williams, and A. Winstral (2005), Persistence of topographic controls on the spatial distribution of snow in rugged mountain terrain, Colorado, United States, *Water Resour. Res.*, *41*(4), n/a–n/a, doi:10.1029/2003WR002973.

Essery, R., J. Pomeroy, C. Ellis, and T. Link (2008), Modelling longwave radiation to snow beneath forest canopies using hemispherical photography or linear regression, , *2800*(June), 2788–2800, doi:10.1002/hyp.

Fagre, D. B., D. L. Peterson, and A. E. Hessl (2003), Taking the pulse of mountains: Ecosystem responses to climatic variability, in *Climatic Change*, vol. 59, pp. 263–282.

Franco-Lopez, H., A. R. Ek, and M. E. Bauer (2001), Estimation and mapping of forest stand density, volume, and cover type using the k-nearest neighbors method, *Remote Sens. Environ.*, *77*(3), 251–274, doi:10.1016/S0034-4257(01)00209-7.

Frazer, G., C. Canham, and K. Lertzman (1999), *Gap Light Analyzer (GLA), Version 2.0: Imaging software to extract canopy structure and gap light transmission indices from true-colour fisheye photographs, users manual and program documentation*.

Gleason, K. E., A. W. Nolin, and T. R. Roth (2013), Charred forests increase snowmelt: Effects of burned woody debris and incoming solar radiation on snow ablation, *Geophys. Res. Lett.*, *40*(August), n/a–n/a, doi:10.1002/grl.50896.

Hall, D. K., and G. A. Riggs (2007), Accuracy assessment of the MODIS snow products, *1547*, 1534–1547, doi:10.1002/hyp.

Hall, D. K., G. a. Riggs, V. V. Salomonson, N. E. DiGirolamo, and K. J. Bayr (2002), MODIS snow-cover products, *Remote Sens. Environ.*, *83*(1-2), 181–194, doi:10.1016/S0034-4257(02)00095-0.

Hansen, M. C., P. V Potapov, R. Moore, M. Hancher, S. A. Turubanova, and A. Tyukavina (2013), High-resolution global maps of 21st- century forest cover change, *Science (80-.).*, *342*(November), 850–853.

Hardy, J. P., R. Melloh, G. Koenig, D. Marks, a. Winstral, J. W. Pomeroy, and T. Link (2004), Solar radiation transmission through conifer canopies, *Agric. For. Meteorol.*, *126*(3-4), 257–270, doi:10.1016/j.agrformet.2004.06.012.

Harpold, A., J. Biederman, K. Condon, M. Merino, Y. Korgaonkar, T. Nan, L. Sloat, M. Ross, and P. D. Brooks (2013), Changes in snow accumulation and ablation following the Las Conchas Forest Fire, New Mexico, USA, *Ecohydrology*, n/a–n/a, doi:10.1002/eco.1363.

Hart, S. J., and T. T. Veblen (2015), Detection of spruce beetle-induced tree mortality using high- and medium-resolution remotely sensed imagery, *Remote Sens. Environ.*, *168*, 134–145, doi:10.1016/j.rse.2015.06.015.

Hart, S. J., T. T. Veblen, K. S. Eisenhart, D. Jarvis, and D. Kulakowski (2014), Drought induces spruce beetle (Dendroctonus rufipennis) outbreaks across northwestern Colorado., *Ecology*, doi:10.1890/13-0230.1.

Hart, S. J., T. Schoennagel, T. T. Veblen, and T. B. Chapman (2015), Area burned in the western United States is unaffected by recent mountain pine beetle outbreaks, *Proc. Natl. Acad. Sci.*, (6), 201424037, doi:10.1073/pnas.1424037112.

Heiskanen, J., M. Rautiainen, P. Stenberg, M. Mõttus, V. H. Vesanto, L. Korhonen, and T. Majasalmi (2012), Seasonal variation in MODIS LAI for a boreal forest area in Finland, *Remote Sens. Environ.*, *126*, 104–115, doi:10.1016/j.rse.2012.08.001.

Hicke, J. a. et al. (2012), Effects of biotic disturbances on forest carbon cycling in the United States and Canada, *Glob. Chang. Biol.*, *18*(1), 7–34, doi:10.1111/j.1365-2486.2011.02543.x.

Hijmans, R. J. (2014), raster: Geographic data analysis and modeling. R package version 2.2-31. http://CRAN.R-project.org/package=raster,

Homer, C., C. Huang, L. Yang, B. Wylie, and M. Coan (2004), Development of a 2001 national land-cover database for the United States, *Photogramm. Eng. Remote Sens.*, *70*(7), 829–840, doi:10.14358/PERS.70.7.829.

Homer, C., J. Fry, and C. Barnes (2012), The National Land Cover Database, *US Geol. Surv. Fact Sheet*, (February), 1–4.

Jenkins, M. J., W. G. Page, E. G. Hebertson, and M. E. Alexander (2012), Fuels and fire behavior dynamics in bark beetle-attacked forests in Western North America and implications for fire management, *For. Ecol. Manage.*, *275*, 23–34, doi:10.1016/j.foreco.2012.02.036.

Johnson, E. W., and J. Ross (2008), Quantifying error in aerial survey data, *Aust. For.*, *71*(3), 216–222, doi:10.1080/00049158.2008.10675038.

Johnson, J., P. Greenfield, and A. S. Munson (1997), An evaluation of the utility of sub-pixel analysis of thematic mapper imagery for the spruce beetle outbreak on the Manti-LaSal National Forest, , 276–287.

Kelly, A. E., and M. L. Goulden (2008), Rapid shifts in plant distribution with recent climate change., *Proc. Natl. Acad. Sci. U. S. A.*, *105*(33), 11823–6, doi:10.1073/pnas.0802891105.

Klein, A. G., A. G. Klein, D. K. Hall, D. K. Hall, G. a Riggs, and G. a Riggs (1998), Improving snow cover mapping in forests through the use of a canopy re¯ectance model 2 1, *Hydrol. Process.*, *12*(December 1997), 1723–1744.

Klutsch, J. G., J. F. Negrón, S. L. Costello, C. C. Rhoades, D. R. West, J. Popp, and R. Caissie (2009), Stand characteristics and downed woody debris accumulations associated with a mountain pine beetle (Dendroctonus ponderosae Hopkins) outbreak in Colorado, *For. Ecol. Manage.*, *258*(5), 641–649, doi:10.1016/j.foreco.2009.04.034.

Knowles, N., M. D. Dettinger, and D. R. Cayan (2006), Trends in Snowfall versus Rainfall in the Western United States, *J. Clim.*, 4545–4559.

Kotchenova, S. Y., and E. F. Vermote (2007), Validation of a vector version of the 6S radiative transfer code for atmospheric correction of satellite data. Part II. Homogeneous Lambertian and anisotropic surfaces., *Appl. Opt.*, *46*(20), 4455–4464, doi:10.1364/AO.46.004455.

Kurz, W. a, C. C. Dymond, G. Stinson, G. J. Rampley, E. T. Neilson, a L. Carroll, T. Ebata, and L. Safranyik (2008), Mountain pine beetle and forest carbon feedback to climate change., *Nature*, *452*(7190), 987–990, doi:10.1038/nature06777.

Law, P. (2014), *Agricultural Act of 2014, Public Law 113-179*.

Lawler, R. R., and T. E. Link (2011), Quantification of incoming all-wave radiation in discontinuous forest canopies with application to snowmelt prediction, *Hydrol. Process.*, *25*(21), 3322–3331, doi:10.1002/hyp.8150.

Lewis, D., and D. Huggard (2010), A Model to Quantify Effects of Mountain Pine Beetle on Equivalent Clearcut Area, , *13*(2).

Liu, J., C. E. Woodcock, R. A. Melloh, R. E. Davis, C. McKenzie, and T. H. Painter (2008), Modeling the View Angle Dependence of Gap Fractions in Forest Canopies: Implications for Mapping Fractional Snow Cover Using Optical Remote Sensing, *J. Hydrometeorol.*, *9*(5), 1005–1019, doi:10.1175/2008JHM866.1.

Livneh, B., J. S. Deems, B. Buma, J. J. Barsugli, D. Schneider, N. P. Molotch, K. Wolter, and C. a. Wessman (2015), Catchment response to bark beetle outbreak and dust-on-snow in the Colorado Rocky Mountains, *J. Hydrol.*, *523*, 196–210, doi:10.1016/j.jhydrol.2015.01.039.

Lundquist, J. D., S. E. Dickerson-Lange, J. a. Lutz, and N. C. Cristea (2013), Lower forest density enhances snow retention in regions with warmer winters: A global framework developed from plot-scale observations and modeling, *Water Resour. Res.*, *49*(section 4), n/a–n/a, doi:10.1002/wrcr.20504.

Macomber, S. a., and C. E. Woodcock (1994), Mapping and Monitoring Conifer Mortality Using Remote Sensing in the Lake Tahoe Basin, *Remote Sens. Environ.*, *266*(October 1993), 255–266, doi:Doi 10.1016/0034-4257(94)90075-2.

Martinec, J. (1975), Snowmelt - runoff model for stream flow forecasts, *Nord. Hydrol.*, *6*(3), 145–154, doi:10.2166/nh.1975.010.

Meddens, A. J. H., and J. a. Hicke (2014), Spatial and temporal patterns of Landsat-based detection of tree mortality caused by a mountain pine beetle outbreak in Colorado, USA, *For. Ecol. Manage.*, *322*, 78–88, doi:10.1016/j.foreco.2014.02.037.

Meddens, A. J. H., J. a. Hicke, and L. a. Vierling (2011), Evaluating the potential of multispectral imagery to map multiple stages of tree mortality, *Remote Sens. Environ.*, *115*(7), 1632–1642, doi:10.1016/j.rse.2011.02.018.

Meddens, A. J. H., J. a Hicke, and C. a Ferguson (2012), Spatiotemporal patterns of observed bark beetle-caused tree mortality in British Columbia and the western United States., *Ecol. Appl.*, *22*(7), 1876–91.

Meddens, A. J. H., J. a. Hicke, L. a. Vierling, and A. T. Hudak (2013), Evaluating methods to detect bark beetle-caused tree mortality using single-date and multi-date Landsat imagery, *Remote Sens. Environ.*, *132*, 49–58, doi:10.1016/j.rse.2013.01.002.

Micheletty, P. D., a. M. Kinoshita, and T. S. Hogue (2014), Application of MODIS snow cover products: wildfire impacts on snow and melt in the Sierra Nevada, *Hydrol. Earth Syst. Sci. Discuss.*, *11*(7), 7513–7549, doi:10.5194/hessd-11-7513-2014.

Mikkelson, K. M., L. a. Bearup, R. M. Maxwell, J. D. Stednick, J. E. McCray, and J. O. Sharp (2013), Bark beetle infestation impacts on nutrient cycling, water quality and interdependent hydrological effects, *Biogeochemistry*, *115*(1-3), 1–21, doi:10.1007/s10533-013-9875-8.

Molotch, N. P., P. D. Blanken, M. W. Williams, A. A. Turnipseed, R. K. Monson, and S. A. Margulis (2007), Estimating sublimation of intercepted and sub-canopy snow using eddy covariance systems, , *1575*, 1567–1575, doi:10.1002/hyp.

Molotch, N. P., P. D. Brooks, S. P. Burns, M. Litvak, R. K. Monson, J. R. Mcconnell, and K. Musselman (2009), Ecohydrological controls on snowmelt partitioning in mixed-conifer sub-alpine forests, , *142*(May), 129–142, doi:10.1002/eco.

Molotch, N. P., P. D. Blanken, and T. E. Link (2011), *Forest Hydrology and Biogeochemistry*, Ecological Studies, edited by D. F. Levia, D. Carlyle-Moses, and T. Tanaka, Springer Netherlands, Dordrecht.

Musselman, K. N., N. P. Molotch, and P. D. Brooks (2008), Effects of vegetation on snow accumulation and ablation in a mid-latitude sub-alpine forest, , *2776*(April), 2767–2776, doi:10.1002/hyp.

Musselman, K. N., N. P. Molotch, S. a. Margulis, P. B. Kirchner, and R. C. Bales (2012), Influence of canopy structure and direct beam solar irradiance on snowmelt rates in a mixed conifer forest, *Agric. For. Meteorol.*, *161*, 46–56, doi:10.1016/j.agrformet.2012.03.011.

Nolin, A. W. (2010), Recent advances in remote sensing of seasonal snow, *J. Glaciol.*, *56*(200), 1141–1150, doi:10.3189/002214311796406077.

O'Halloran, T. L. et al. (2012), Radiative forcing of natural forest disturbances, *Glob. Chang. Biol.*, *18*(2), 555–565, doi:10.1111/j.1365-2486.2011.02577.x.

Painter, T. H., J. Dozier, D. a. Roberts, R. E. Davis, and R. O. Green (2003), Retrieval of subpixel snow-covered area and grain size from imaging spectrometer data, *Remote Sens. Environ.*, *85*(1), 64–77, doi:10.1016/S0034-4257(02)00187-6.

Painter, T. H., K. Rittger, C. McKenzie, P. Slaughter, R. E. Davis, and J. Dozier (2009), Retrieval of subpixel snow covered area, grain size, and albedo from MODIS, *Remote Sens. Environ.*, *113*(4), 868–879, doi:10.1016/j.rse.2009.01.001.

Painter, T. H., A. C. Bryant, and S. M. Skiles (2012), Radiative forcing by light absorbing impurities in snow from MODIS surface reflectance data, *Geophys. Res. Lett.*, *39*(17), n/a–n/a, doi:10.1029/2012GL052457.

Perrot, D., N. P. Molotch, K. N. Musselman, and E. T. Pugh (2012), Modelling the effects of the mountain pine beetle on snowmelt in a subalpine forest, *Ecohydrology*, n/a–n/a, doi:10.1002/eco.1329.

Pickett, S. T. a (1989), Space for time substitution as an alternative to long-term studies, *Long-term Stud. Ecol.*, 71–88.

Pugh, E., and E. Small (2012), The impact of pine beetle infestation on snow accumulation and melt in the headwaters of the Colorado River, *Ecohydrology*, *5*(4), 467–477, doi:10.1002/eco.239.

Pugh, E. T., and E. E. Small (2013), The impact of beetle-induced conifer death on stand-scale canopy snow interception, *Hydrol. Res.*, *44*(4), 644, doi:10.2166/nh.2013.097.

R Core Team (2014), R: A language and environment for statistical computing. R Foundation for Statistical Computing, Vienna, Austria. URL http://www.R-project.org/.,

Raffa, K. F., B. H. Aukema, B. J. Bentz, A. L. Carroll, J. a. Hicke, M. G. Turner, and W. H. Romme (2008), Cross-scale Drivers of Natural Disturbances Prone to Anthropogenic Amplification: The Dynamics of Bark Beetle Eruptions, *Bioscience*, *58*(6), 501, doi:10.1641/B580607.

Raleigh, M. S., K. Rittger, C. E. Moore, B. Henn, J. A. Lutz, and J. D. Lundquist (2013), Ground-based testing of MODIS fractional snow cover in subalpine meadows and forests of the Sierra Nevada, *Remote Sens. Environ.*, *128*, 44–57, doi:10.1016/j.rse.2012.09.016.

Rittger, K., T. H. Painter, and J. Dozier (2013), Assessment of methods for mapping snow cover from MODIS, *Adv. Water Resour.*, *51*, 367–380, doi:10.1016/j.advwatres.2012.03.002.

Rosenberger, R. S. ., L. A. . Bell, P. A. . Champ, and E. L. . Smith (2012), Nonmarket economic values of forest insect pests: An updated literature review, *USDA For. Serv. - Gen. Tech. Rep. RMRS-GTR*, (275), 1–46.

Saab, V. a., Q. S. Latif, M. M. Rowland, T. N. Johnson, A. D. Chalfoun, S. W. Buskirk, J. E. Heyward, and M. a. Dresser (2014), Ecological consequences of mountain pine beetle outbreaks for wildlife in Western North American forests, *For. Sci.*, *60*(3), 539–559, doi:10.5849/forsci.13-022.

Sacks, W. J., D. S. Schimel, and R. K. Monson (2007), Coupling between carbon cycling and climate in a high-elevation, subalpine forest: a model-data fusion analysis., *Oecologia*, *151*(1), 54–68, doi:10.1007/s00442-006-0565-2.

Safranyik, L. (2004), Mountain Pine Beetle Epidemiology in Lodgepole Pine, in *Taylor, S W & Carroll, a L, Mountain Pine Beetle Symposium: Challenges and Solutions*, pp. 41–51.

Safranyik, L., and B. Wilson (2006), *The mountain pine beetle: a synthesis of biology, management, and impacts on lodgepole pine*, Natural Resources Canada, Canadian Forest Service, Pacific Forestry Centre.

Safranyik, L., D. Shrimpton, and H. Whitney (1974), Management of Lodgepole Pine to Reduce Losses from the Mountain Pine Beetle, , (October 1974), 23.

Salomonson, V. ., and I. Appel (2004), Estimating fractional snow cover from MODIS using the normalized difference snow index, *Remote Sens. Environ.*, *89*(3), 351–360, doi:10.1016/j.rse.2003.10.016.

Sicart, J. E., R. L. H. Essery, J. W. Pomeroy, J. Hardy, T. Link, and D. Marks (2004), A Sensitivity Study of Daytime Net Radiation during Snowmelt to Forest Canopy and

Atmospheric Conditions, *J. Hydrometeorol.*, *5*, 774–784, doi:10.1175/1525-7541(2004)005<0774:ASSODN>2.0.CO;2.

Sicart, J. E., R. Hock, and D. Six (2008), Glacier melt, air temperature, and energy balance in different climates: The Bolivian Tropics, the French Alps, and northern Sweden, *J. Geophys. Res. Atmos.*, *113*(24), 1–11, doi:10.1029/2008JD010406.

Simard, M., W. H. Romme, J. M. Griffin, and M. G. Turner (2011), Do mountain pine beetle outbreaks change the probability of active crown fire in lodgepole pine forests?, *Ecol. Monogr.*, *81*(1), 3–24, doi:10.1890/10-1176.1.

Singer, F. S., and R. W. Popham (1963), Non-meteorological observations from satellites, *Astronaut. Aerosp. Eng.*, *1*(3), 89–92.

Smith, J. M., J. Paritsis, T. T. Veblen, and T. B. Chapman (2015), Permanent forest plots show accelerating tree mortality in subalpine forests of the Colorado Front Range from 1982 to 2013, *For. Ecol. Manage.*, *341*, 8–17, doi:10.1016/j.foreco.2014.12.031.

Spittlehouse, D. ., and R. D. Winkler (2005), Snowmelt in a Forest and Clearcut, *Hyrdological Process.*, *19*, 51–62.

Stueve, K. M. et al. (2011), Snow-covered Landsat time series stacks improve automated disturbance mapping accuracy in forested landscapes, *Remote Sens. Environ.*, *115*(12), 3203–3219, doi:10.1016/j.rse.2011.07.005.

Tan, B., C. E. Woodcock, J. Hu, P. Zhang, M. Ozdogan, D. Huang, W. Yang, Y. Knyazikhin, and R. B. Myneni (2006), The impact of gridding artifacts on the local spatial properties of MODIS data: Implications for validation, compositing, and band-to-band registration across resolutions, *Remote Sens. Environ.*, *105*(2), 98–114, doi:10.1016/j.rse.2006.06.008.

Teti, P. (2008), Effects of overstory mortality on snow accumulation and ablation, *Nat. Resour. Canada, Can. For. Serv.*

Troendle, A. (1983), The Potential for Water Yield Augmentation from Forest Management in the Rocky Mountain Region, *Water Resour. Bull.*, *19*(3), 359–373.

Trujillo, E., N. P. Molotch, M. L. Goulden, A. E. Kelly, and R. C. Bales (2012), Elevation-dependent influence of snow accumulation on forest greening, *Nat. Geosci.*, *5*(10), 705–709, doi:10.1038/ngeo1571.

USFS (2015), Aerial survey highlights for Colorado 2014, Available from: http://www.fs.usda.gov/Internet/FSE_DOCUMENTS/stelprd3828662.pdf (Accessed 1 January 2015)

Varhola, A., N. C. Coops, M. Weiler, and R. D. Moore (2010), Forest canopy effects on snow accumulation and ablation: An integrative review of empirical results, *J. Hydrol.*, *392*(3-4), 219–233, doi:10.1016/j.jhydrol.2010.08.009.

Veblen, T., K. Hadley, M. Reid, and A. Rebertus (1991), The Response of Subalpine Forests to Spruce Beetle Outbreak in Colorado, *Ecology*, *72*(1), 213–231.

Vikhamar, D., and R. Solberg (2003), Snow-cover mapping in forests by constrained linear spectral unmixing of MODIS data, *Remote Sens. Environ.*, *88*(3), 309–323, doi:10.1016/j.rse.2003.06.004.

Welch, C. M., P. C. Stoy, F. A. Rains, A. V. Johnson, and B. L. McGlynn (2015), The impacts of mountain pine beetle disturbance on the energy balance of snow during the melt period, *Hydrol. Process.*, n/a–n/a, doi:10.1002/hyp.10638.

Westerling, A., H. Hidalgo, D. Cayan, and T. Swetnam (2006), Warming and earlier spring increase western U.S. forest wildfire activity., *Science*, *313*(5789), 940–3, doi:10.1126/science.1128834.

Williams, A. et al. (2012), Temperature as a potent driver of regional forest drought stress and tree mortality, *Nat. Clim. Chang.*, *3*(3), 292–297, doi:10.1038/nclimate1693.

Williams, C. J., J. P. McNamara, and D. G. Chandler (2009), Controls on the temporal and spatial variability of soil moisture in a mountainous landscape: the signature of snow and complex terrain, *Hydrol. Earth Syst. Sci.*, *13*(7), 1325–1336, doi:10.5194/hess-13-1325-2009.

Winkler, R., S. Boon, B. Zimonick, and K. Baleshta (2010), Assessing the effects of post-pine beetle forest litter on snow albedo, *Hydrol. Process.*, *24*(6), 803–812, doi:10.1002/hyp.7648.

Winkler, R., S. Boon, B. Zimonick, and D. Spittlehouse (2014), Snow accumulation and ablation response to changes in forest structure and snow surface albedo after attack by mountain pine beetle, *Hydrol. Process.*, *28*(2), 197–209, doi:10.1002/hyp.9574.

Winkler, R. D., R. D. D. Moore, T. E. Redding, D. L. Spittlehouse, B. D. Smerdon, and D. E. Carlyle-moses (2006), *The Effects of Forest Disturbance on Hydrologic Processes and Watershed Response*.

Winstral, A., K. Elder, and R. Davis (2002), Spatial Snow Modeling of Wind-Redistributed Snow Using Terrain-Based Parameters, , (Berg 1977), 524–538.

Wolfe, R. E., M. Nishihama, A. J. Fleig, J. a. Kuyper, D. P. Roy, J. C. Storey, and F. S. Patt (2002), Achieving sub-pixel geolocation accuracy in support of MODIS land science, *Remote Sens. Environ.*, *83*(1-2), 31–49, doi:10.1016/S0034-4257(02)00085-8.

Wulder, M. a., C. C. Dymond, J. C. White, D. G. Leckie, and A. L. Carroll (2006), Surveying mountain pine beetle damage of forests: A review of remote sensing opportunities, *For. Ecol. Manage.*, *221*(1-3), 27–41, doi:10.1016/j.foreco.2005.09.021.

Xiao, X., C. Biradar, A. Wang, S. Sheldon, and Y. Chen (2011), Recovery of Vegetation Canopy after Severe Fire in 2000 at the Black Hills National Forest , South Dakota , USA, , *2*(2), 106–116, doi:10.3969/j.issn.1674-764x.2011.02.002.

Xin, Q., C. E. Woodcock, J. Liu, B. Tan, R. a. Melloh, and R. E. Davis (2012), View angle effects on MODIS snow mapping in forests, *Remote Sens. Environ.*, *118*, 50–59, doi:10.1016/j.rse.2011.10.029.

Zhu, Z., and D. L. Evans (1994), US forest types and predicted percent forest cover from AVHRR data, *Photogramm. Eng. Remote Sensing*, *60*(5), doi:10.1016/j.cosust.2013.08.001.